

**Study of the mechanisms of microbubble-facilitated sonoporation *in vitro* in
controlled environments**

by

Zhenzhen Fan

**A dissertation submitted in partial fulfillment
of the requirements for the degree of
Doctor of Philosophy
(Biomedical Engineering)
in The University of Michigan
2012**

Doctoral Committee:

**Associate Professor Cheri X. Deng, Chair
Professor J. Brian Fowlkes
Professor Shuichi Takayama
Associate Professor Joseph L. Bull**

**To my parents and my husband
for their love and support**

Acknowledgements

I would first like to thank my mom and dad for their love, encouragement and support, for their teaching me the value of good spirit and hard working. Without them, I would not be able to accomplish what I have achieved, or even one tenth of that.

I would like to express my deepest gratitude to Dr. Cheri Deng, my advisor, for her patience and kindness, for her understanding and confidence in me. The dissertation would not have seen the light of day without her constant inspiring mentoring. My enormous debt of gratitude can hardly be repaid to her for her guidance and support during every stage in my graduate study.

I would like to thank my dissertation committee for their inspiring guidance and support. Their invested time, support, and helpful suggestions in shaping my research and dissertation are greatly appreciated.

I would like to thank Dr. Ron Kumon, Dr. Juyoung Park and Dr. Yun Zhou for their countless efforts in helping me with my projects. I am extremely privileged to have you as mentors and friends.

Many thanks go to lab members in Dr. Deng's lab, Dr. Cain's lab and Dr. Xu' lab for their friendship and help, as well as my collaborators outside ultrasound group.

Finally, I would like to thank my husband, Xuan Wu, for his unwavering support and encouragement. Thanks for all your love.

Table of Contents

Dedication	ii
Acknowledgements	iii
List of Figures	vii
Abstract	xiv
Chapter 1 Introduction	1
1.1 Specific aims	2
1.2 Background	4
1.2.1 Current techniques for intracellular drug and gene delivery	4
1.2.2 Therapeutic application of ultrasound combined with microbubbles	7
1.2.3 Dynamic behaviors of microbubbles driven by ultrasound	8
1.2.4 Disruption of the cell membrane	10
1.2.5 Transmembrane transport by sonoporation and down-stream effects	11
1.3 Rationale and significance of this study	12
Chapter 2 Intracellular Delivery and Calcium Transients Generated in Sonoporation Facilitated by Microbubbles	14
2.1 Introduction	14
2.2 Materials and methods	16
2.2.1 Cell culture	16
2.2.2 Microbubbles	17
2.2.3 Measurement of intracellular calcium concentration	18
2.2.4 Determination of membrane permeabilization with propidium iodide	21
2.2.5 Optical imaging and data analysis	22
2.2.6 Ultrasound application and calibration	23
2.2.7 Experimental protocols	24
2.2.8 Curve fitting	25
2.3 Results	26
2.3.1 Ultrasound-driven microbubble activities, sonoporation, and calcium transients	26
2.3.2 Spatiotemporal evolution of intracellular marker and calcium	28
2.3.3 Delayed calcium transport in cells without pore formation	30

2.3.4 Concentration-gradient driven, bidirectional transport of markers and pore closure	32
2.3.5 Cell viability.....	36
2.4 Discussion.....	37
2.5 Conclusion	41
Chapter 3 Dynamic Activities of Microbubbles Driven by Ultrasound Exposures Correlated with Delivery Outcomes by Sonoporation.....	42
3.2 Materials and methods	43
3.2.1 Cell culture.....	43
3.2.2 Assessments of delivery outcomes	43
3.2.3 Ultrasound exposure and microbubbles.....	44
3.2.4 Optical imaging.....	44
3.2.5 Data analysis	45
3.3 Results.....	45
3.3.1 Characterization of the bubble dynamics correlated with sonoporation outcomes	45
3.3.2 Mapping sonoporation outcomes with bubble dynamics.....	55
3.3.3 Effects of ultrasound parameters on bubble dynamics	56
3.4 Discussion.....	59
3.4.1 Sonoporation correlated with bubble dynamics.....	59
3.4.2 High speed imaging and ultra-fast imaging	60
3.4.3 Biologic relevance besides intracellular delivery	61
3.4.4 Different experimental setting results in different bubble dynamics.....	61
3.5 Conclusion	62
Chapter 4 Controlled and Enhanced Delivery Facilitated by Targeted Microbubbles.....	63
4.1 Introduction.....	63
4.2 Materials and methods	63
4.2.1 Cell culture.....	63
4.2.2 Preparation of microbubbles	64
4.2.3 Plasmid labeling and transfection	65
4.2.4 Experimental setup and ultrasound application	66
4.2.5 Optical imaging.....	67
4.2.6 Data analysis	67
4.3 Results.....	69
4.3.1 Controlled delivery by targeted microbubbles.....	69

4.3.2 Comparison of bubble dynamics between targeted and non-targeted microbubbles.....	73
4.3.3 Delivery outcomes by sonoporation using targeted and non targeted microbubbles.....	76
4.3.4 Optimization of PI delivery	77
4.3.5 Enhanced gene transfection achieved by targeted microbubble and optimized ultrasound exposure condition	80
4.4 Discussion.....	84
4.4.1 Controlled ultrasound excitation of targeted microbubbles.....	84
4.4.2 Binding force between targeted microbubbles and cell membrane	85
4.4.3 Restoring and detachment mechanisms	86
4.4.4 Loading capability of antibody on microbubbles	87
4.4.5 The impact of primary radiation force and ratio of bubble/cell on delivery outcomes	87
4.5 Conclusion	92
Chapter 5 Future Work	94
5.1 Specific topics for future investigations	95
5.1.1 Manipulation of the contraction rhythm of cardiomyocyte via controlled Ca^{2+} influx by sonoporation	95
5.1.2 Study of gene internalization and expression pathways in sonoporation	96
5.1.3 Microbubbles patterning and spatially defined delivery by incorporating aqueous two phase system (ATPS) with sonoporation.....	98
References.....	100

List of Figures

Figure 2-1 (A) Schematic diagram of experimental apparatus for spatiotemporal measurements of intracellular delivery of fluorescent marker and calcium transients generated by ultrasound-driven microbubble activities (B) Picture of OptiCell™ cell culture chamber (C) Schematic diagram of OptiCell™, cells and Definity® microbubbles.	17
Figure 2-2 Experiment results using the fura2 calcium concentration calibration kit. A linear fitting was applied.....	20
Figure 2-3 (A) Spectra of fura2. Isosbestic point is the excitation wavelength, at which fura2 fluorescence intensity is independent from calcium concentration, cited from Invitrogen handbook. (B) Experimental detection of isosbestic point. A cell, which had no PI uptake, indicating no pore created, but $[Ca^{2+}]_i$ change, was excited at wavelength of 360 nm to 365 nm and 380 nm. 360 nm was found as isosbestic point, as no change was observed of emission when the cell was excited at 360 nm, while the cell experienced $[Ca^{2+}]_i$ change.....	21
Figure 2-4 Schematic diagram of experimental protocols for monitoring intracellular delivery and calcium transients generated by ultrasound-driven microbubbles.....	25
Figure 2-5 Propidium iodide (PI) delivery and intracellular $[Ca^{2+}]_i$ transients are temporally correlated with ultrasound-driven microbubbles. (A) Bright field image with superimposed PI fluorescence image before ultrasound application. No PI is observed in the cells. The solid lines show two regions of interest within cells (Cell 1 and Cell 2). The arrow points the microbubble next to Cell 2. (B) Bright field image with superimposed pseudocolor $[Ca^{2+}]_i$ image, indicating the initial $[Ca^{2+}]_i$ distribution before ultrasound application. (C) PI fluorescence intensity changes (from the baseline) as a function of time for Cells 1 and 2 induced by ultrasound simulation of the microbubbles. (D) $[Ca^{2+}]_i$ changes for Cells 1 and 2 as a function of time. In C and D, the break indicates the period when light was directed to the high speed camera. (E) High-speed camera recordings of the ultrasound-driven microbubble inside the dashed frames in (A) and (B) show bubble fragmentation.	28
Figure 2-6 Intracellular delivery of propidium iodide (PI) and intracellular $[Ca^{2+}]_i$ transients are spatially correlated with stimulation of microbubbles by ultrasound. (A)	

Time-lapse PI fluorescence images and (B) pseudocolor $[Ca^{2+}]_i$ images, corresponding to the traces shown in Fig.2-5C and D respectively. The solid lines show the two regions of interest (Cell 1 and Cell 2), while the circle outlines microbubble next to Cell 2 at the beginning of the experiment. The color bar indicates the $[Ca^{2+}]_i$ in μM . The first row shows the cells before ultrasound exposure while the subsequent rows show the cells at the indicated times after ultrasound application. 30

Figure 2-7 (A) Time-lapse sequence of PI fluorescence images and (B) time-lapse sequence of pseudocolor $[Ca^{2+}]_i$ images for five cells, where the color bar in row B indicates the $[Ca^{2+}]_i$ in μM . Only Cell 1 (arrow) shows immediate $[Ca^{2+}]_i$ change at the time of ultrasound and immediately PI uptake are seen in only cell 1 (arrow pointed). Cells 2 to 5 show delayed $[Ca^{2+}]_i$ transients without any PI uptake. (C) $[Ca^{2+}]_i$ as a function of time for Cells 1–5, showing the immediate change in calcium (cell 2) and delayed calcium change (cells 2–5). The $[Ca^{2+}]_i$ returned to a higher level than initial $[Ca^{2+}]_i$ for Cell 1, while all the delayed cells returned to approximately their initial level. (D) PI intensity change as a function of time for Cells 1–5. Only Cell 1 shows any PI uptake. 32

Figure 2-8 Scatter plot of $[Ca^{2+}]_i$ change and PI intensity change, both at 5 min since the start of fluorescence imaging for 36 cells, showing positive correlation ($R = +0.91$). 34

Figure 2-9 Pore generation is corroborated by simultaneous PI uptake, $[Ca^{2+}]_i$ increase, and fura-2 dye loss. (A) Changes in PI fluorescence intensity, $[Ca^{2+}]_i$, and fura-2 fluorescence intensity from excitation at 360 nm as a function of time, as induced by ultrasound-driven microbubbles for the cell shown in the inset (arrow pointing to microbubble), indicating increase in $[Ca^{2+}]_i$, PI uptake, and fura-2 dye loss generated by ultrasound application. Dashed lines show fitting of PI uptake and fura-2 loss to exponential recovery or decay models. (B) The change of fura-2 intensity from excitation at 360 nm and change of PI intensity change, both at 5 min since the start of fluorescence imaging for 36 cells are negatively correlated ($R = -0.78$), indicating loss of fura-2. 36

Figure 2-10 PI intensity difference in sonoporated but surviving cells (N=35), and dead cells (N=15), which were confirmed by Trypan blue staining. 37

Figure 3-1 A typical example of Definity® microbubbles behavior category 1: aggregation and microstreaming. In this example, Definity® microbubbles were suspended in OptiCell™, driven by 1M hz transducer, with 0.06 MPa, 20 hz PRF, 20% DC (10 ms in each pulse), 1s exposure totally. Panel (A) shows selective bright field images of a $216 \mu m \times 180 \mu m$ area before, during and immediately post ultrasound application, followed by fluorescence images excited at 538 nm before and post ultrasound for PI signals, and fluorescence images excited at 488 nm for calcein signal post ultrasound. Two sub-areas are selected in panel (A), labeled as (B) and (C), showing

microbubbles aggregation and microstreaming respectively. More temporal information was shown in panel (B) and (C) accordingly..... 47

Figure 3-2 Quantitative analysis of Definity microbubbles dynamics in the data shown in Fig.3-1. (A) Total bubble number change in the FOV as a function of time over 1s ultrasound exposure. (B) Histogram of cluster size before ultrasound and at 1s. 48

Figure 3-3 A typical example of Definity® microbubbles behavior category 2: coalescence and translation. In this example, Definity® microbubbles were suspended in OptiCell™, driven by 1Mhz transducer, with 0.43 MPa, 20 hz PRF, 20% DC (10 ms in each pulse), 1s exposure totally. (All bubble disappeared immediately after 1st ultrasound.) Panel (A) shows selective bright field images of a 216 μm×180 μm area before, during and immediately post ultrasound application, followed by fluorescence images excited at 538 nm before and post ultrasound for PI signals, and fluorescence images excited at 488 nm for calcein signal post ultrasound. Panel (B) and (C) are sub-areas shown in the image of Panel (A), with more temporal information, illustrating coalescence in (B) and newly fused big bubble fast translating while violently oscillating in (C). 49

Figure 3-4 Quantitative analysis of Definity microbubbles dynamics in the data shown in Fig.3-2. (A) Total bubble number change in FOV as a function of time over 10ms. (B) Percentage of moving bubble change as a function of time over 10ms..... 50

Figure 3-5 A typical example of Definity® microbubbles behavior category 3: collapse. In this example, Definity® microbubbles were suspended in OptiCell™, driven by 1Mhz transducer, with 0.43MPa, 10 hz PRF, 10 μs (10 cycles) in each pulse, 1 s exposure totally. (All bubble disappeared after 4th ultrasound pulse.) Panel (A) shows selective bright field images of a 257 μm×184 μm area before, post 1st ultrasound pulse, followed by fluorescence images excited at 538 nm before and post ultrasound for PI signals, and fluorescence images excited at 488 nm for calcein signal post ultrasound. Panel (B-D) are ultrasound excited Definity® microbubbles images captured by ultra-fast camera with frame rate 2M fps, showing three different bubble activities during ultrasound exposure, oscillation (B), forming microjet (C) and fragment (D). The direct observation of panel (C) is vortex ring formation, which indicating a flow is penetrating the center of the ring, which is microjet. The time label and scale bar in (B) apply for (C) and (D). 52

Figure 3-6 Quantitative analysis of Definity microbubbles dynamics according to the example shown in Fig.3-5. (A) Total bubble number change as a function of time. (B) Percentage of moving bubbles changes as a function of time. (C) Radius change as a function of time of a bubble in this data. 53

Figure 3-7 Bubble dynamics characterization (A) and the corresponding PI delivery outcomes (B) under the ultrasound conditions creating the basic three categories: Cat.1

Aggregation and microstreaming (US: 0.06MPa, 20hz PRF, 20% duty cycle, 1s); Cat.2. Coalescence and translation (US: 0.43MPa, 20hz PRF, 20% duty cycle, 1s); and Cat.3. Collapse (US: 0.43MPa, 10hz PRF, 0.008% duty cycle, 1s). Viability is defined as the number of surviving cells divided by the total number of cells in the FOV. Delivery efficiency is defined as the number of surviving and PI uptake cells divided by the total number of cells in the FOV. “N” is the number of experiments conducted. 55

Figure 3-8 Mapping bubble dynamics (A) and sonoporation outcomes (B) of 4 data sets using the typical three categories as landmarks. The ultrasound condition for the 4 data sets are: Data set1: 0.10 MPa, 20 hz PRF, 20% DC, 1 s (N=4); Data set 2: 0.12 MPa, 20 hz PRF, 10% DC, 1s (N=8); Data set 3: 0.23 MPa, 20 hz, 0.4% DC (200 μ s in each pulse), 1 s (N=4); and Data set 4: 0.23 MPa, 20 hz PRF, 20% DC, 1 s (N=4). 56

Figure 3-9 Impact of ultrasound parameters, including acoustic pressure (A and B) and PRF (C and D) to bubble dynamics 58

Figure 3-10 Impact of ultrasound parameter (acoustic pressure and duty cycle) to bubble dynamics. Bubble dynamics were characterized by % of remaining bubble at 1s (A) and % of moving bubbles (B).0.008% duty cycle data were with 10hz PRF. All other data were with 20hz PRF..... 58

Figure 4-1 Multiple targeted microbubbles attached on cell membrane (A) resulted multiple entry area of PI (B) and Ca^{2+} (C). Ultrasound applied was of 0.17 MPa and 2.4 μ s duration. 70

Figure 4-2 Multiple excitations of ultrasound pulses induced multiple entry of PI and Ca^{2+} at different time. (A) $[Ca^{2+}]_i$ change, indicated by ratio of 340 nm excitation and 380 nm excitation, and PI intensity change as a function of time. Insert is a bright field image before ultrasound superimposed with PI fluorescent image at time 11s. Scale bar is 10 μ m. (B) Selective fluorescent images of PI (first row) and pseudocolor $[Ca^{2+}]_i$ images. The first ultrasound pulse was of 0.17 MPa and 2.4 μ s duration, and second pulse was of 0.23 MPa and 2.4 μ s duration. 70

Figure 4-3 Maximum bubble radius during expansion is correlated with bubble initial size, under a certain ultrasound condition. (A-C) Ultra-fast images of Definity® microbubbles with different initial radius (1.9 μ m, 3.1 μ m and 5.3 μ m) were excited by 0.29 MPa and 5 μ s ultrasound. (D) Scatter plot of maximum bubble radius during expansion as a function of initial radius (n=24) excited by 0.29 MPa and 5 μ s ultrasound. A linear fitting was applied, with the goodness of fitting $R^2=0.87$ 72

Figure 4-4 Excitation of microbubbles with different radius by different ultrasound pressure to achieve staged delivery. Before ultrasound, bubble 1 was of 2 μ m radius and

bubble 2 was of 1.5 μm radius. The first ultrasound (0.26 MPa and 8 μs) was applied at time 0 s, another ultrasound pulse (0.6 MPa and 8 μs) was applied at time 250 s. 72

Figure 4-5 A typical example of Targestar™-SA microbubbles behavior category 1: aggregation and microstreaming. In this example, Targestar™-SA microbubbles were conjugated with anti-human CD31 antibody bound on HUVEC cells, excited by a 1.25 Mhz transducer, with 0.06 MPa, 20 hz PRF, 20% DC (10ms in each pulse), 1 s exposure totally. Panel (A) shows selective bright field images of a 216 μm ×180 μm area before, during and immediately post ultrasound application, followed by fluorescence images excited at 538 nm before and post ultrasound for PI signals, and fluorescence images excited at 488 nm for calcein signal post ultrasound. Four sub-areas are selected in Panel (A), labeled as (B-D). (B) and (C) are microbubbles, which were bound the cell surface though entire ultrasound exposure; while (D) and (E) are microbubbles, whose link to cell surface were broken during ultrasound exposure. More temporal information was shown in panel (B-D) accordingly. 74

Figure 4-6 A typical example of Targestar™-SA microbubbles behavior category 2: coalescence and translation. In this example, Targestar™-SA microbubbles were conjugated with anti-human CD31 antibody bound on HUVEC cells, excited by a 1.25 Mhz transducer, with 0.43 MPa, 10 ms. (All bubble disappeared immediately after ultrasound.) Panel (A) shows selective bright field images of a 216 μm ×180 μm area before, during and immediately post ultrasound application, followed by fluorescence images excited at 538 nm before and post ultrasound for PI signals, and fluorescence images excited at 488 nm for calcein signal post ultrasound. Panel (B) and (C) are sub-areas shown in the image of panel (A), with more temporal information, illustrating coalescence in (B) and newly fused big bubble fast translating while violently oscillating in (C). 75

Figure 4-7 A typical example of Targestar™-SA microbubbles behavior category 3: collapse. In this example, Targestar™-SA microbubbles were conjugated with anti-human CD31 antibody bound on HUVEC cells, excited by a 1.25 Mhz transducer, with 0.43 MPa PNP, 10hz PRF, 0.008% duty cycle, 1s. Selective bright field images of a 293 μm ×233 μm areas before, during and post 1s ultrasound are shown followed by fluorescence images excited at 538 nm before and post ultrasound for PI signals, and fluorescence images excited at 488 nm for calcein signal post ultrasound. 76

Figure 4-8 PI delivery outcomes of Definity® microbubbles (non-targeted microbubbles) in Opticell setting and Targestar™-SA microbubbles (targeted microbubbles) in petri dish setting in three typical categories: Cat.1: aggregation and microstreaming; Cat.2: coalescence and translation; and Cat.3: collapse. Ultrasound conditions used for data shown here for Definity® microbubbles are: Cat.1: 0.06 MPa, 20 hz PRF, 20% DC

(10ms in each pulse), 1 s (N=9); Cat.2: 0.43 MPa, 20 hz PRF, 20% DC, 1 s (N=10); and Cat.3: 0.43 MPa, 10 hz PRF, 0.008% duty cycle, 1 s (N=13). Ultrasound conditions used for data shown here for Targestar™-SA microbubbles were the same as Definity® microbubbles: Cat 1 (N=6); Cat 2 (N=6); and Cat 3 (N=4)..... 77

Figure 4-9 Viability (A) and delivery efficiency (B) using PI as the delivery indicator with different ultrasound pulses. For all data, the acoustic pressure was 0.43MPa, 10hz PRF (for multiple pulses) and 8µs for each pulse. N ≥ 5 for each condition. 78

Figure 4-10 Viability (A), delivery efficiency (B) and PI intensity (C) with different acoustic pressure. For all data, single ultrasound pulse with 8µs duration was applied. N ≥ 5 for each condition. 79

Figure 4-11 Impact of the number of bubbles attached per cells (# bubble/cell) on delivery outcomes. (A-C) are typical example of # bubble/cell distribution 1 and (D-E) are typical example of distribution 2. (A) and (D) are calcein image superimposed bright field image before ultrasound. (B) and (E) are cell number grouped by # bubble/cell corresponding to the example shown in (A) and (D) in the entire FOV. Green, yellow and red represent surviving and no PI uptake cells, surviving and PI delivered cells and killed cells respectively. (C) and (F) convert the information shown in (B) and (E) into percentage within three groups (1bubble/cell, 2bubble/cell and 3bubble/cell). 80

Figure 4-12 BOBO™-iodide labeled plasmid delivery was spatially correlated with bubble attached cells. (A) Fluorescent image excited at 570 nm post ultrasound. (B) Phase contrast bright field image post ultrasound. (C-D) are (A) superimposed with bright field image before and post ultrasound. Arrows point the bubbles, which resulted plasmid uptake. 81

Figure 4-13 Characterization of bubble number and bubble size change in three ultrasound conditions: 1.6 MPa, 8 µs (A and B); 1.6 MPa, 8 µs followed by 1.8 MPa, 8 µs with 50 ms time interval (C and D); and 1.6 MPa, 8 µs, followed by 1.8 MPa, 8 µs, and 2.0 MPa, 8 µs with 50 ms time interval (E and F). (G) Gene transfection efficiency corresponding to the three conditions, and from lipofection (purple filled bar)..... 83

Figure 4-14 Example images show GFP expressed cells (A) and superimposed with bright field phase contrast image (B) using ultrasound condition: 1.6 MPa, 8 µs followed by 1.8 MPa, 8 µs with 50 ms time interval. 84

Figure 4-15 Schematic illustration of the direction of primary radiation force in Opticell setting with Definity® microbubbl (A) and in petri dish setting with Targestar™-SA targeted microbubble (B). 88

Figure 4-16 Force diagram of Definity® microbubble once it was pushed away from cell monolayer. 88

Figure 4-17 Simulation of resonance frequency of Definity® microbubbles (A), time-averaged primary radiation force on a Definity® microbubble with 0.06MPa peak negative pressure and 20% DC (B) and buoyancy of Definity® microbubbles in water. 91

Figure 5-1 A example demonstrates that contraction rhythm of cardiomyocyte was changed by ultrasound application in the presence of microbubbles. (A) Bright field image before ultrasound of a group of cardiomyocytes clustered together attached on the upper inner membrane of Opticell. Some of the black circles were Definity® microbubbles, such as the ones pointed by arrows. The area within the frame was selected to monitor the contraction. The zoomed area is shown on the right side of the image. The black small area in the center of this frame was traced and analyzed using Matlab. Its displacement relative to its original position at time 0 as a function of time was plotted in (B). A single ultrasound pulse with 0.43MPa peak negative pressure and 8 μ s duration was applied at time 10s. 96

Figure 5-2 BOBO-labeled plasmid distribution 30minutes after sonoporation (A), and 24 hours after sonoporation (B) of the same area; and 24 hours after lipofection (C). 98

Figure 5-3 Illustration of picoliter microbubble patterning and spatially defined delivery 99

Abstract

Successful delivery of drug molecules and therapeutic genetic materials across the plasma membrane into the target cells in sufficient dosage is important for satisfactory treatment effects. Ultrasound excitation of microbubbles generates disruption of the cell membrane (sonoporation) and opens new opportunities for non-viral intracellular drug and gene delivery. When excited by ultrasound, microbubbles undergo rapid volume expansion and contraction as well as collapse (cavitation) and can temporally disrupt the cell membrane, creating a direct physical route for the transport of extracellular agents into viable cells. However, despite increasing interest and recent progresses, challenges and difficulties remain to be overcome, including relatively low delivery efficiency and large variation in delivery outcomes. These difficulties are mainly due to the insufficient understanding of the underlying mechanisms and process of sonoporation. This study aims to obtain a comprehensive understanding of sonoporation mechanisms and process under well controlled environments. We employed various strategies to precisely control microbubbles location and cavitation, using fast-frame bright field video-microscopy combined with real-time fluorescence microscopy to reveal ultrasound excited microbubble dynamics and subsequent cellular responses, such as membrane rupture, calcium transient and waves, and gene transfection. The specific aims of this study are: 1) to investigate the intracellular transport and calcium transient generated by sonoporation; 2) to exploit dynamics activities of microbubbles driven by ultrasound and correlate with

delivery outcomes; 3) to achieve controlled and enhanced delivery outcomes facilitated by targeted microbubbles.

Chapter 1

Introduction

Successful delivery of drug molecules and therapeutic genetic materials across the plasma membrane into the target cells in sufficient dosage is important for satisfactory treatment effects [1, 2]. Sonoporation, or ultrasound generated disruption of the cell membrane, has been exploited as a new strategy for non-viral intracellular drug and gene delivery [3-10]. However, despite increasing interest and progresses made recently, challenges and difficulties remain to be overcome, including relatively low delivery efficiency and large variation in delivery outcomes [11].

The objective of this study is to develop sonoporation as a controlled and highly efficient intracellular delivery technique based on a comprehensive understanding of sonoporation process and mechanisms under controlled environments. The mechanic impact of ultrasound excited microbubble exerted on the nearby cells has been recognized to be the cause for the reversible increase of the cell membrane permeability (sonoporation) [12-14], allowing entry of extracellular therapeutic agents into the cells through temporally disrupted regions on the membrane [15-17]. Microbubble-facilitated sonoporation has demonstrated great potential as an efficient, non-invasive and targeted delivery method for many *in vitro* and *in vivo* applications [3-7], although difficulties and challenges remain to be overcome.

1.1 Specific aims

Transportation of drug molecule and therapeutic genetic materials across the plasma cell membrane is highly significant and an important area of pursuit in basic biological and medical research. Various approaches have been exploited [12, 18-21]; yet robust intracellular delivery of these bio-molecules still remains a major challenge. Sonoporation is the ultrasound generated poration of cell membrane [15, 22, 23]. The physical disruption of cell membrane by ultrasound, often facilitated by microbubbles, creates a direct physical route for the transport of extracellular membrane impermeable compounds into the cytoplasm of viable cells, thereby making microbubble-facilitated sonoporation a promising technique for intracellular delivery of therapeutic agents.

Even with recent progress in the field, however, many difficulties still remain that hinder the practical translation of sonoporation technology into a viable and robust strategy. Sonoporation currently has relatively low delivery efficiency compared with other techniques such as viral vector transfection, and large variation exists in the delivery outcomes [11]. These difficulties are largely due to the lack of knowledge about sonoporation occurrence and its subsequent bioeffects. Therefore, it is of great importance to elucidate microbubble activities on the cell membrane and cellular responses to reveal the underlying mechanisms. Static post-ultrasound assessment methods that many conventional sonoporation studies employed, may not be suitable for investigating the inherently dynamic and transient process of sonoporation, because no detailed information is available to directly relate the microbubble-cell interaction with sonoporation outcomes.

In this study, we aim to investigate the underlying mechanisms and processes of sonoporation and the relevant consequences at cellular level in order to achieve controlled and improved drug and gene delivery outcomes. Designed to address the key questions in order to obtain improved understanding of the mechanisms of sonoporation, the specific aims of this research are:

Aim 1: To investigate intracellular transport and calcium transients generated by sonoporation facilitated by non-targeted microbubble;

Aim 2: To study the dynamic activities of non-targeted microbubbles driven by ultrasound and correlate with delivery outcomes;

Aim 3: To achieve controlled and improved delivery outcomes facilitated by targeted microbubbles.

These three aims will be described and discussed in details in chapters 2 – 4. To address the specific aims, we developed a research design that employs various strategies to control microbubbles location and activities to establish controlled experimental environments. Fast-frame bright field video-microscopy synchronized with ultrasound application was employed to monitor the microbubble activities upon ultrasound stimulation; while real-time fluorescence microscopy was applied to assess membrane rupture, intracellular calcium transient and waves, and gene transfection. By spatiotemporally correlating the bubble dynamics with these biological consequences, we characterized the transient processes of pore formation, studied microbubble dynamics under various ultrasound conditions, and finally utilized this knowledge to achieve controlled and improved delivery outcomes.

1.2 Background

1.2.1 Current techniques for intracellular drug and gene delivery

Identification of molecular mechanisms responsible for diseases and the synthesis of new drug or genetic strategies alone cannot guarantee efficient therapy. Successful delivery of therapeutic agents to the designated target cells and even sub-cellular sites of action with sufficient dosage is essential to achieve satisfactory treatment effects [1, 2]. Conventional drug delivery methods, such as intravenous injection and oral administration, are not suitable for highly toxic anticancer drugs or recombinant DNAs for gene therapy, as all healthy tissues and organs are undesirably exposed to the drugs and genes. There has been an upsurge of global interests in developing targeted delivery techniques, in order to increase drug and gene delivery efficacy as well as to minimize any side effects [7, 12, 20, 24]. Although targeted delivery shows great potential, it faces serious technical challenges due to many diffusional and metabolic fences on the delivery pathway [25]. One major difficulty is to facilitate therapeutic agents transport across plasma cell membrane. Another barrier is the nuclear membrane, in the case of gene delivery, as well as antibody and drugs whose targeted action sites are located in cell nuclei [25-27].

As a special case of drug delivery, gene delivery is an emerging therapeutic strategy that offers the promise of treating a wide variety of inherited and acquired diseases by genetic modification of cells or production of therapeutic proteins within cells [18, 27, 28]. Most genetic molecules are both large and negatively charged, making it difficult for them to spontaneously transpass the negatively charged and relatively lipophilic plasma membrane [27]. Therefore, assisting delivery reagents or external

energy deposit has been exploited to facilitate gene transportation across the cell membrane. Gene transfection techniques may be divided into two categories: viral and non-viral. Viral vectors take use of the millions-of-years naturally evolved ability of virus to efficiently transfer genetic material of their own into host cells. The viral vectors, in general, are superior to their non-viral counterparts [21, 29]. Viral vectors derived from retroviruses, adenovirus, adeno-associated virus, herpesvirus and poxvirus are actively employed both at the level of laboratory developments and of clinical applications [21, 29]. Despite the remarkable efficacy in gene transfection, the possibility of viral vector to evoke inflammatory and adverse immunogenic responses and to produce insertional mutagenesis limits its translation from preclinical studies to human treatment [30, 31].

In contrast, non-viral gene delivery methods possess many important safety advantages, therefore attracting increasing attention, although transfection efficiency is still far from being ideal [18, 32]. In non-viral gene transfection, genetic materials exist in the format of plasmid vectors, which are composed entirely of covalently closed circles of double-stranded DNA [33]. To aid entry of plasmids into cells, transfection reagent molecules and/or physical energy is often required. The materials currently used as non-viral gene transfection reagents include cationic and neutral lipids, cationic polymers, peptides or combination thereof [28, 34]. The most commonly used is cationic liposome (microscopic vesicles of amphiphilic molecules surrounding a watery interior) mediated gene transfer, often termed as lipofection [35-37]. Due to the similarity to plasma cell membrane, liposome exhibits high biocompatibility. Cationic liposomes form a complex with negatively charged DNA molecules (known as “lipoplex”) with a small net positive charge, which can be electrostatic attracted by the negatively charged cell membrane.

While the process of DNA attachment onto the cell membrane is rapid, the trafficking of plasmid DNA inside the cell toward nucleus is generally slow (hours), as plasmid DNA has to escape from endosome after endocytosis, migrate toward nucleus, and traverse nuclear envelop [38-40]. Along the way, the foreign DNA could be partially degraded by cytoplasmic DNases or by the acidic environment in late endosome or lysosome [34, 38, 40, 41]. The nuclear membrane barriers, DNases metabolism and endosome environment, etc. vary dramatically among different cell types, which may explain the large variation of transfection efficiency by lipofection in different cell types.

A number of physical approaches, as an alternative to viruses or transfection reagents, have been demonstrated to enhance plasmid delivery by temporarily increasing the permeability of cell membrane. Physical methods include microinjection, magnetofection, laser poration, ballistic delivery, hydrodynamic delivery, electroporation and ultrasound mediated delivery (sonoporation) [42-44]. Electroporation and microbubble-mediated ultrasound are two of the most effective physical methods that can be applied both *in vitro* and *in vivo*. Electroporation is an established technique to introduce DNA or other molecules into cells by transiently increasing cell membrane permeability using a high electric field [45-48]. The creation of aqueous pores is believed to be the cause of increased permeability in electroporation [45-48]. The size of these membrane openings in red blood was reported to be between 20 nm-120 nm [49]. The precise dynamic details of cell membrane change during electroporation are still elusive. It has been suggested that small molecules, such as anticancer drugs, can enter cells *via* simple diffusion through pores induced by strong electrical fields; while macromolecules, such as DNA, enter cells through a more complex interaction with cell membrane,

involving the electrophoretically driven interaction of the DNA molecules with the destabilized membrane during the electric pulses and then their passage across the membrane [19]. Many factors have effects on transport efficiency in electroporation, including electrodes configurations, pulse patterns, pulse magnitude, and duration etc. It's reported that short pulses (100 μ s) of high electric field strength (>700 V/cm) is optimal for small anti-cancer drug delivery, whereas longer pulses (20-60 ms) with lower field strength (100-200 V/cm) were preferred for gene transfer [50, 51].

1.2.2 Therapeutic application of ultrasound combined with microbubbles

Ultrasound technology is spreading its medical application from diagnostic imaging to medical therapy. This change is coupled with the advent and development of engineered gas bubbles. First introduced as an ultrasound imaging contrast enhancement agents, microbubbles have shown great potential for their therapeutic application recently [12, 52, 53]. Although the mechanisms of ultrasound microbubble mediated delivery is not yet fully understood, cavitation of microbubbles by ultrasound excitation is most likely to be the cause for reversibly increase of the cell membrane permeability, often termed as sonoporation [54-56]. Many studies have examined the improved effect of ultrasound microbubble mediated delivery, including delivery of drugs [57-60], antibody [61] peptide [62, 63], siRNA [8-10], and DNA plasmid [64-68] both *in vitro* and *in vivo*. However, currently sonoporation has, in general, low delivery efficiency compared with viral techniques as well as other non-viral techniques such as lipofection and electroporation [11, 40]. Understanding the fundamental mechanisms involved in sonoporation, and making use of this knowledge to improve the technique, provides a rational approach to successfully develop sonoporation technique.

1.2.3 Dynamic behaviors of microbubbles driven by ultrasound

Microbubbles play a key role in sonoporation. To enhance microbubbles stability, prolong their life-time, and potentially loading drugs and assisting targeted adhesion, microbubbles are formulated as lipid or polymer encapsulating microspheres with a water-insoluble gas core such as perfluorocarbon, with a radius of 1- 4 μm typically [26, 69-72]. The shell of ultrasound contrast agents typical has a thickness of 10 to 100 nm [73]. When microbubbles oscillate driven by ultrasound field, lipid shell buckles into a bilayer during compression and shed during expansion [74-76]; while polymer and albumin shells usually rupture with discrete defects [77, 78]. The lipid shell, which is used on many shelled microbubbles, such as Definity® (Lantheus Medical Imaging, Billerica, MA) and Targestar™-SA (Targeson, La Jolla, CA), readily expands, ruptures, reseals, compresses and buckles under ultrasound field, which has been explicitly investigated theoretically and validated experimentally [79-86].

Accumulation of microbubbles on the specific molecular sites on the cell surface is a strategy used to increase site specificity and delivery efficacy. The ligand-receptor interactions exist extensively in biological media and exhibit high selectivity. Therefore, ligands have been applied to decorate the surface of microbubbles via biotin-avidin linkage. Consequently these ligands can guide microbubbles adhere on the cell surface, where the corresponding receptors are expressed. These modified microbubbles, capable of binding to a receptor, are called targeted microbubbles [72, 87-89]. In addition to surface decoration for targeted attachment, microbubbles can be manufactured to have more complicated structure to serve as drugs and genes carrier vehicles. Different strategies have been exploited, such as electrostatically coupled charged compound, DNA

or RNA, onto the cationic shell [90]; dissolving hydrophilic or lipophobic drugs in the oil, which incorporated into the lipid shell [91]; or attaching nanoparticles through biotin-avidin bridging system [92].

No matter whether the drug molecules are co-administrated with microbubbles or loaded within the microbubbles, ultrasound pulses are applied to stimulate the microbubbles to facilitate sonoporation and the intracellular uptake of drug and genes. The outcome depends on the dynamic behaviors of microbubbles driven by ultrasound exposures. Based on direct optical observation, individual microbubble behaviors have been observed to exhibit phenomena including oscillation, fragmentation, micro fluidic jetting, translation, and coalescence [13, 84, 93-98]. Inertial cavitation is the expansion and contraction as well as collapse of bubbles driven by the inertia of the surrounding fluid and occurs when the acoustic pressure amplitude is above a threshold level [99]. In inertial cavitation, microbubbles first grow in volume, and then implode violently, resulting in fragmentation, microjetting, generation of highly reactive free radicals and even emitting photons (sonoluminescence) [94, 100-103]. In non-inertial cavitation or stable cavitation, microbubbles oscillate with relatively small amplitude at the frequency of incoming ultrasound. Microstreaming also occur as a result of cavitation [104-106]. In addition, microbubbles are subjected to a net force, the (primary) acoustic radiation force, which is associated with the applied ultrasound field [107-109]. If multiple microbubbles are present proximately, microbubbles are also subjected to the secondary acoustic radiation force, resulting from the scattered acoustic field generated by the other pulsating microbubbles [109-112]. The secondary radiation force can cause attraction or repulsion of microbubbles. Aggregation and coalescence (fuse into one big bubble)

among multiple microbubbles are mostly driven by secondary radiation force [83, 111-113].

1.2.4 Disruption of the cell membrane

Ultrasound induced microbubble dynamic activities have been reported to be able to disrupt cell membrane. Prentice et al have demonstrated that fluid microjet was produced when encapsulated microbubbles excited by ultrasound in proximity to cell monolayer attached on a rigid substrate [13]. And the compression of cells due to the expansion of microbubbles was also suggested to be a possible way leading to membrane permeability change [97]. Evidence has been shown that shear stress built up with microstreaming generated by gentle/linear bubble oscillations is sufficient to rupture lipid membranes [114].

It is indicated that nano- to micro scale pores generated on the cell membrane is the cause for increased membrane permeability and transporting of drug and gene is mainly via these pores. Great efforts have been made to visualize and characterize the pores. Scanning electron microscopy (SEM) revealed the presence of pores with the diameter from 100 nm to 1 μ m [14, 17, 56, 115-118]. Atomic force microscopy (AFM) images [13, 119], transmission electron microscopy (TEM) images [15] and confocal fluorescence microscopy image [15] confirmed the plasma membrane discontinuity in sonicated cell surface; although the dimension of the break varies greatly, from 1 nm to 1 μ m diameter. Due to rapid resealing of the pores, however, these post ultrasound assays may not accurately obtain the pore information. Previous study in our lab employed voltage clamp technique using a *Xenopus laevis* oocyte model and estimated the pore size to be in the order of 100 nm [120].

1.2.5 Transmembrane transport by sonoporation and down-stream effects

Despite many investigations, the detailed processes and mechanisms of drug and gene uptake and intracellular trafficking pathway via sonoporation is still under debate. The transmembrane transport appears to be dependent on the size of the agents to be delivered [15, 121, 122]. Small molecule, such as calcein, was homogeneously distributed throughout cytosol as well as in nuclei. Fewer uptakes were observed for larger molecules along with less homogeneous distribution and limited access to nuclei [15, 121]. The co-localization of macromolecules and endocytosis markers implied that endocytosis was also involved in transporting macromolecule such as plasmid by sonoporation [121, 123], although contradictory evidences were published as well [40].

In addition to pore formation or triggering endocytosis, other bioeffects have also been reported to be associated with sonoporation. Ca^{2+} influx was reported by several research groups [14, 16, 124-129], including the early studies in our lab that demonstrated Ca^{2+} influx and oscillation in Chinese hamster ovary (CHO) cells [128, 129]. Juffermans et al suggested that the formation of hydrogen peroxide (H_2O_2) provokes Ca^{2+} influx [124]. Apoptosis has been reported in cells exposed to ultrasound application [130-134]. It was suggested that the reactive oxygen species (ROS) generated from mitochondria, rather than ROS directly produced by inertial cavitation of microbubbles in medium, combined with Ca^{2+} influx play a critical role in ultrasound induced apoptosis [133]. The results from both fluorescent imaging of voltage sensitive dye (di-4-ANEPPs) stained cell membrane [135], and whole-cell current clamp technique [136-138] illustrated that hyperpolarization occurred during ultrasound exposure in the presence of microbubbles; and activation of BKca channels were proposed to be the

cause for hyperpolarization. The reversible cytoskeletal F-actin fiber arraignment and number change were reported to be resulted from ultrasound exposure alone and more pronounced with the present of microbubble [126].

1.3 Rationale and significance of this study

Sonoporation, as mentioned above, provides an advantageous opportunity to facilitate targeted intracellular uptake of drugs and genes. At present, the understanding of sonoporation mechanisms is insufficient. The difficulties in sonoporation mechanisms studies arise from the inherently transient, dynamic, microscopic, complicated biochemical-physical nature involved in the interaction of ultrasound excited microbubbles with cells. In many sonoporation studies, freely floating microbubbles were employed [8, 139-141]. This adds extra factor to the complexity and the uncertainty of the dynamic process. Therefore, creating a controlled environment of microbubble and cell interaction is important for investigation of sonoporation mechanisms.

Many studies have been reported to optimize sonoporation delivery outcomes by manipulating ultrasound parameters as well parameters such as bubble concentration, concentration of agents to be delivered [142-145]. In the absence of mechanistic understanding, however, these studies are limited by their specific experimental configuration and condition.

To explore the cellular/molecular biological consequences followed by cell membrane rupture in sonoporation, techniques, such AFM, SEM, TEM, and confocal fluorescent microscopy were used [13, 15, 115, 119, 121]. The superior spatial resolution of these imaging techniques provides spatial details of a fixed cell after ultrasound treatment. However, since there is relatively huge time span between plasma membrane

poration in live cells and examination of fixed cell sample, these findings may not be directly correlated with the actual sonoporation process.

In this study, we created well-controlled *in vitro* experimental environments by physical restriction of microbubbles and attaching microbubbles onto cell surface via ligand-receptor reaction to study the transient process of sonoporation at cellular level. We explicitly elucidate the relationship between membrane rupture and $[Ca^{2+}]_i$ transient and intracellular Ca^{2+} wave; extensively explored the dynamic microbubble activities in a population under various ultrasound exposures and spatial-temporally correlated with delivery outcomes; and achieved enhanced gene transfection efficiency by optimizing microbubble dynamics instead of blind adjustment of ultrasound parameters.

Chapter 2

Intracellular Delivery and Calcium Transients Generated in Sonoporation Facilitated by Microbubbles

In this chapter, we described in detail our study to investigate the change of cell membrane permeability and changes of intracellular calcium concentration ($[Ca^{2+}]_i$) generated by ultrasound-driven microbubbles. Using a combination of imaging techniques, real-time fluorescent microscopy, we obtained results of intracellular uptake and calcium transients that were spatiotemporally correlated with high-speed bright field images of ultrasound-driven microbubbles activities.

2.1 Introduction

Ultrasound application with microbubbles have demonstrated the promise to facilitate intracellular transport of different kinds of therapeutic agents, such as drug molecule, genetic materials, that are otherwise impermeable to the cell [11, 146-152]. One major route for intracellular uptake is suggested to be through transient and reversible pores created on the cell membrane [12-14]. However, a detailed mechanistic description of sonoporation and its full range of bioeffects remain to be elucidated [153].

Calcium ion as is a ubiquitous intracellular signal responsible for regulating numerous cellular activities, such as control of muscle contraction, neurotransmitter releases, synaptic plasticity, cell proliferation and apoptosis. Because of the importance of calcium as a second messenger, the impact of sonoporation on intracellular and intercellular calcium signaling becomes one of the most important bioeffects aspects that

researchers in therapeutic ultrasound area investigated. Recent studies have demonstrated that cells treated with ultrasound and microbubbles can exhibit temporal calcium transients [124, 154, 155]. In particular, we have shown temporal calcium oscillations and spatial waves can be generated, resulting in calcium changes in cells away from the cells that directly interact with microbubbles over distances of hundreds of microns and tens of seconds after ultrasound application [156]. Due to the central role that calcium ions play in cellular functions regulation and intercellular communication, changes in the intracellular calcium ion concentration $[Ca^{2+}]_i$ resulting from ultrasound exposure may have unintended consequences in ultrasound-mediated delivery applications such as cardiac gene transfection and targeted cancer drug delivery. However, while these studies suggested that calcium response occurs as a result of ultrasound application in the presence of microbubbles, it is not explicitly clear whether sonoporation of the cell membrane with intracellular delivery directly causes $[Ca^{2+}]_i$ activities.

In this study, we employ a combination of imaging techniques to determine whether sonoporation of cardiomyoblast cells and $[Ca^{2+}]_i$ changes are generated by the interaction between individual microbubbles and cells via pore formation. Ultrasound-driven microbubble activity was imaged using high-speed bright-field imaging, which was synchronized and spatially correlated with a real-time fluorescence imaging system specially designed to simultaneously measure changes in $[Ca^{2+}]_i$ and membrane permeabilization using multiple fluorescent dyes.

2.2 Materials and methods

2.2.1 Cell culture

H9c2 rat cardiomyoblast cells (ATCC, Manassas, VA) were grown in a humidified incubator at 37°C and 5% CO₂ in cell culture flasks containing the complete cell culture medium consisting of Dulbecco's modified Eagle's medium (Gibco Invitrogen, Carlsbad, CA) supplemented with 10% fetal bovine serum (HyClone, Logan, UT) and 1% penicillin-streptomycin (HyClone, Logan, UT). Two days before the sonoporation experiment, the cells were harvested from the flasks and seeded into an OptiCell™ chamber (Nunc, Rochester, NY) filled with the same cell culture medium. OptiCell™ chambers consist of two parallel, gas-permeable, cell-culture-treated, polystyrene membranes (50 cm², 75 μm thick, 2 mm apart) attached to a standard microtiter plate-sized frame, shown in Fig.2-1B. At the time of experiment, the cells had reached approximately 90% confluency.

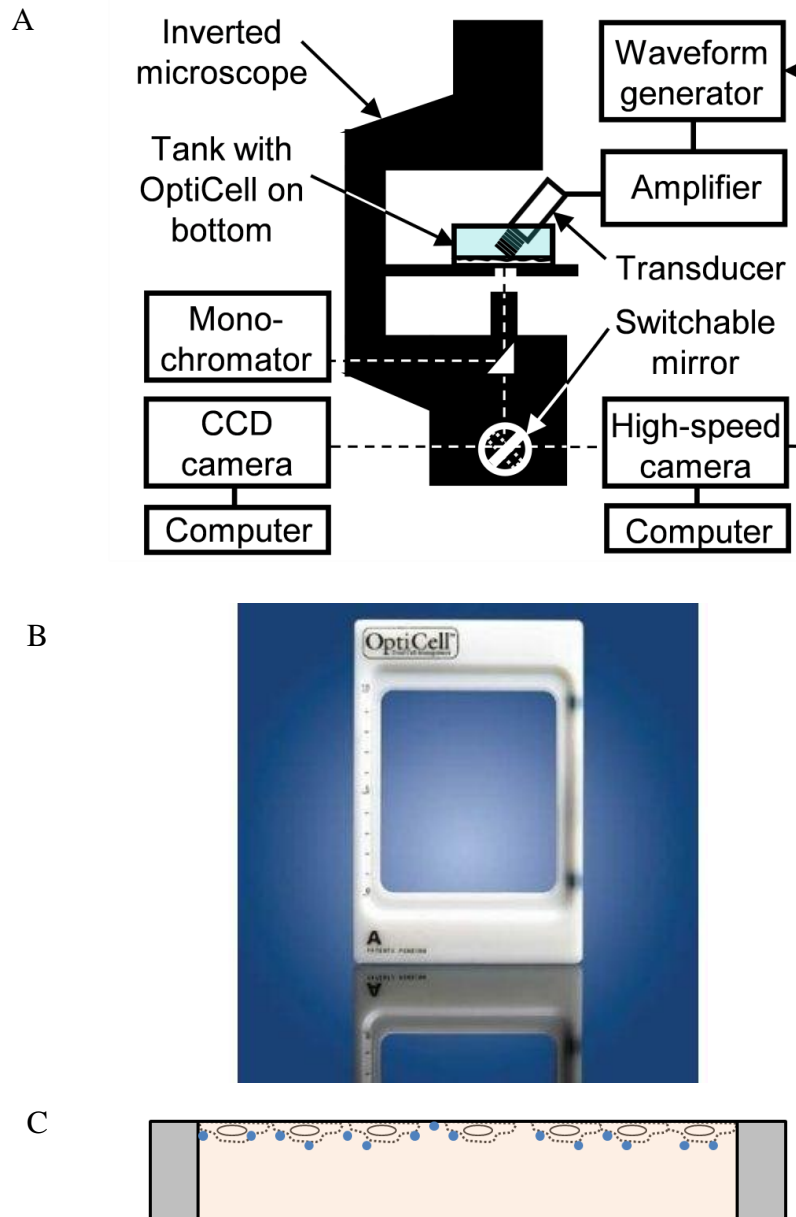


Figure 2-1 (A) Schematic diagram of experimental apparatus for spatiotemporal measurements of intracellular delivery of fluorescent marker and calcium transients generated by ultrasound-driven microbubble activities (B) Picture of OptiCell™ cell culture chamber (C) Schematic diagram of OptiCell™, cells and Definity® microbubbles.

2.2.2 Microbubbles

Definity® (Lantheus Medical Imaging, Billerica, MA) consists of distributed encapsulated microbubbles, each with a C_3F_8 gas core encapsulated by an outer phospholipid shell. Immediately after activation following the manufacturer's protocol,

the suspension contains approximately 1.2×10^{10} microbubbles/mL with mean diameter range of 1.1 μm –3.3 μm . However, for the current experiments, the solution was diluted with PBS to have a final concentration of 10^6 microbubbles/mL such that most cells had only 1 or 2 bubbles in their immediate vicinity. During the experiment, OptiCell™ was facing down, so that microbubbles can be in close contact with cells, as illustrated in Fig.2-1C.

2.2.3 Measurement of intracellular calcium concentration

Fluorescence imaging of intracellular calcium concentration, $[\text{Ca}^{2+}]_i$, was performed using the indicator dye fura-2 [157]. To load the dye into the cells, the cells were incubated for 60 minutes at 37°C and 5% CO_2 in complete cell culture medium containing 7.8 μM fura-2AM (Invitrogen, Carlsbad, CA) dissolved in DMSO and 0.05% v/v of 10% w/v Pluronic F-127 (Invitrogen, Carlsbad, CA) in water. After incubation, excess dye was removed by washing the cells three times with complete culture medium before ultrasound exposure. The OptiCell™ chamber was then filled with Dulbecco's Phosphate-Buffered Saline solution (DPBS, Gibco Invitrogen 14040, Carlsbad, CA), which has $[\text{Ca}^{2+}]_o = 0.9$ mM. Quantitative measurement of $[\text{Ca}^{2+}]_i$ was achieved via calibrated ratiometric imaging. The “raw” emitted fluorescence intensities (at 510 nm) for both excitation wavelengths 340 nm and 380 nm in each cell was determined from manually segmented regions of the cell in the images. The background-corrected fluorescence intensities (F_{340} , F_{380}) were obtained by subtracting the fluorescence intensity from an area free of cells from the raw intensities. The ratio $R = F_{340}/F_{380}$ was related to the change in the intracellular calcium concentration according to

$$[Ca^{2+}]_{free} = K_d \times \left[\frac{R - R_{min}}{R_{max} - R} \right] \times \frac{F_{max}^{380}}{F_{min}^{380}} \quad \text{Equ. 2-1}$$

where the parameters $R_{min} = 0.0226$, $R_{max} = 0.749$, $F_{min}^{380} = 232.9$ and $F_{max}^{380} = 1949.3$ were obtained by using a fura-2 calibration kit (Invitrogen F6774, Carlsbad, CA). The calibration kit contains samples of 0 μM , 0.017 μM , 0.038 μM , 0.065 μM , 0.100 μM , 0.150 μM , 0.225 μM , 0.351 μM , 0.602 μM , 1.35 μM and 39 μM free calcium standard solution with 50 μM fura-2 in each sample. It provided another sample without fura2, which was used as the background measure. The measurements at different calcium concentration were all corrected by the background intensity. The results for R_{min} and F_{min}^{380} were obtained using 0 μM calcium sample, while the results for R_{max} and F_{max}^{380} were obtained using 39 μM calcium sample. All the calibration measurement were carried out using 40x extra long working distance objective, at the same setting as in experiments, with exposure time 656 ms, and 100% electron multiplication gain in Easy Ratio Pro software (PTI, Birmingham, NJ). A set of fluorescent curves of 340 nm and 380 nm excitation were generated using the 11 different calcium concentration solution samples, a figure with $\log \left\{ \frac{R - R_{min}}{R - R_{max}} \times (F_{max}^{380} / F_{min}^{380}) \right\}$ as y-axis and $\log[Ca^{2+}]$ (M) as x-axis was plotted. A linear fitting was employed, the x-intercept should be equal to the log of the apparent K_d , as shown in Fig.2-2. The measurement was without cells and used glass cover slides, which was different from the intracellular environment and OptiCell™ configuration in real experiment, so to convert the ratio of 340 nm and 380 nm into $[Ca^{2+}]_i$, dissociation coefficient $K_d = 155$ nM was taken from the literature [158].

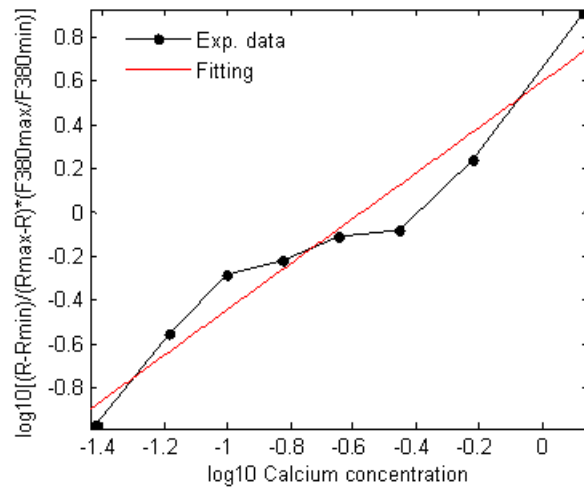


Figure 2-2 Experiment results using the fura2 calcium concentration calibration kit. A linear fitting was applied.

Fura-2 is a ratiometric fluorescent dye which binds to free intracellular calcium and the spectrum varies with different calcium concentration. However, there is one excitation wavelength, at which the emission of fura-2 is independent from calcium concentration but fura-2 dye concentration, which is named as isosbestic point (Fig.2-3A) The isosbestic point is reported around 360 nm. We conducted experiments to confirm that the isosbestic point of fura-2 in our experiments to be 360 nm by examining the emission intensities as a function of time in cells sequentially excited at 340 nm, 360 nm, 361 nm to 365 nm, 380 nm, and 539 nm (for PI excitation) while ultrasound application initiated change (increase) in $[Ca^{2+}]_i$. In the cells that did not exhibit PI uptake but with (delayed) change in $[Ca^{2+}]_i$ (e.g., as a result of a calcium wave but not pores on the membrane), the emission intensity from 360 nm excitation stayed unchanged, while the emission intensities from excitation at longer wavelengths increasingly resembled the response from excitation at 380 nm (which decreases in amplitude when $[Ca^{2+}]_i$ increases), as shown in Fig.2-3B.

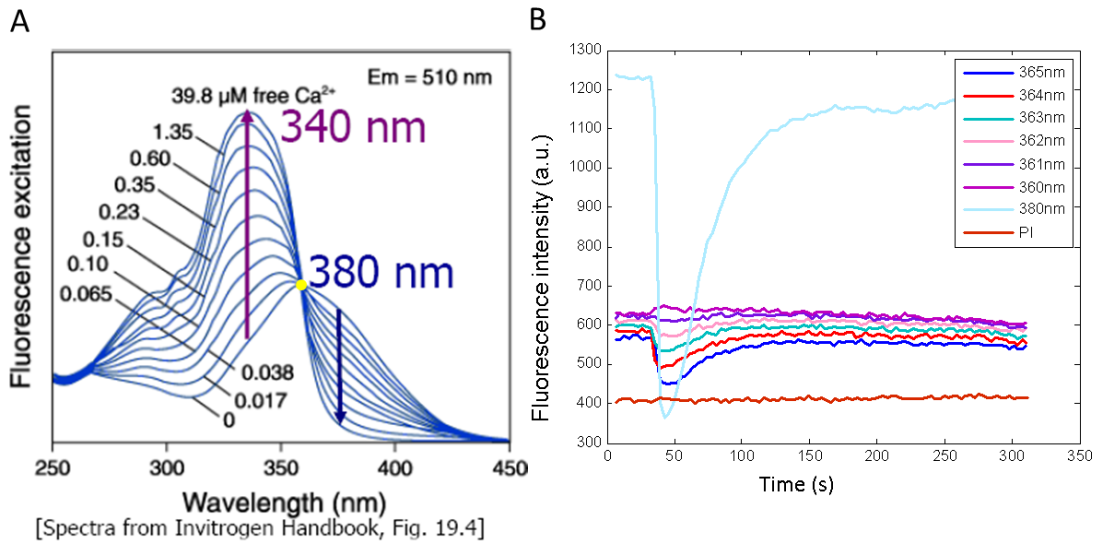


Figure 2-3 (A) Spectra of fura2. Isosbestic point is the excitation wavelength, at which fura2 fluorescence intensity is independent from calcium concentration, cited from Invitrogen handbook. (B) Experimental detection of isosbestic point. A cell, which had no PI uptake, indicating no pore created, but $[Ca^{2+}]_i$ change, was excited at wavelength of 360 nm to 365 nm and 380 nm. 360 nm was found as isosbestic point, as no change was observed of emission when the cell was excited at 360 nm, while the cell experienced $[Ca^{2+}]_i$ change.

2.2.4 Determination of membrane permeabilization with propidium iodide

Change in cell membrane permeabilization by ultrasound was assessed by detecting the intracellular fluorescence intensity of the intercalating agent propidium iodide (PI; 668 Da) (Sigma Aldrich, St. Louis, MO). After loading with fura-2, PI was added to the extracellular solution to achieve a final concentration of 120 μ M. To detect PI, the specimen was excited at 539 nm, and emission was detected at 610 nm. (Excitation at the ultraviolet wavelengths caused a very low-intensity emission from PI that cannot be fully distinguished from the emission from the fura-2; however, this effect is estimated to cause an error of less than 5%.) As PI only fluoresces at these wavelengths when inside the cell, it provides a good real-time marker for delivery via membrane disruption from the extracellular solution with real-time fluorescence imaging. While irreversible changes in PI fluorescence are often used as a marker for cell death, here

transient changes in PI fluorescence were also used as a marker for permeation of the cell membrane.

2.2.5 Optical imaging and data analysis

A schematic diagram of the experimental apparatus is shown in Fig.2-1A. The fura-2-loaded cells in the OptiCell™ chamber filled with the solution of PI and microbubbles were placed on a 37°C heating stage of an inverted microscope (Nikon Eclipse Ti-U, Melville, NY). The real-time fluorescence imaging employed a monochromator (DeltaRAM X™, PTI, Birmingham, NJ) with 5 nm bandpass to repeatedly filter light from a 75 W xenon lamp at the various excitation wavelengths previously described, with an exposure time of 656 ms during fura-2 imaging and 400 ms during PI imaging. The excitation light was directed through either a 20× Super Fluor (Nikon MRF00200, Melville, NY; NA 0.75) or a 40× Plan Fluor objective (Nikon MRH08420, Melville, NY; NA 0.60) and the light subsequently emitted from the cells was passed through a polychroic filter (Chroma 73000v2, Rockingham, VT) with passbands in the green and red. The resulting series of 16 bit grayscale photomicrographs were acquired with a cooled CCD camera (Photometrics QuantEM, Tucson, AZ) at a 512 × 512 resolution. Electron multiplication gain in the camera was set to 100% during fura-2 imaging and 80% during PI imaging. The image acquisition and analysis from this camera were performed using the software package Easy Ratio Pro (PTI, Birmingham, NJ). To create the calibrated calcium images, image post-processing was performed using MATLAB (Mathworks, Natick, MA) and MetaFluor Analyst (Molecular Devices, Downingtown, PA). Noise in the regions outside the cells was suppressed by using intensity-modulated display approach [159] using the 340 nm images for modulation, as

described previously [154]. The grayscale PI images were artificially-colored red for display purposes by zeroing the green and blue components of each pixel.

Microbubble activity was captured using a high-speed, bright field camera (Photron FASTCAM SA1, San Diego, CA) at a resolution of 1024×1024 , rate of 5400 frames/s, and total exposure time of ~ 2 s. The specimen was illuminated with metal-halide light source (Dolan-Jenner MH-100, Boxborough, MA) only during the high-speed imaging.

2.2.6 Ultrasound application and calibration

The ultrasound system used for the experiment consisted of a non-focused circular transducer specially-designed and constructed for our study (1 MHz center frequency, 0.635 cm diameter, Advanced Devices, Wakefield, MA). The transducer was driven by a function/waveform generator (Agilent Technologies 33250A, Palo Alto, CA) and a 75 W power amplifier (Amplifier Research 75A250, Souderton, PA). The transducer was characterized in free field using computer-controlled system with a 40 μm calibrated needle hydrophone (Precision Acoustics HPM04/1, UK). Prior to the experiment, the transducer was aligned with the field of view (FOV) of the microscope objective using a thin wire attached on the top surface of a water-filled OptiCell™ with a plastic wall attached around its entire edge to create a small tank, which was subsequently filled with deionized water for acoustic energy coupling.

This alignment apparatus was then removed and replaced by the OptiCell™ containing the cells loaded with fura-2 and with PI in the extracellular medium, also with a coupling tank on top filled with deionized water. The water in the tank is physically isolated from the cells by the upper membrane of the OptiCell™ chamber. The transducer

was positioned such that the active surface of the ultrasound transducer submerged in solution was ~7 mm from the cells at the bottom of the dish at an angle of approximately 45 degrees (Fig.2-1). The transducer had a near field distance of ~6.4 mm and spatial width (half-max) at 7.5 mm, which is the approximate distance between the transducer and OptiCell™ chamber during the experiments. As such, the entire FOV of the microscope (200 × 200 μm at 40× objective, 400 × 400 μm at 20× objective) was insonified. The cells are attached to the top polystyrene membrane of the OptiCell™ chamber. Standing wave effects [140] due to the bottom membrane of the OptiCell™ were minimized by angling the ultrasound beam and using short pulses. The generated ultrasound waveforms at the region of interest had peak negative pressure of 0.27 MPa as determined from the calibration above. A single ultrasound tone burst of 10 or 15 cycles was applied during each experiment.

2.2.7 Experimental protocols

Two protocols were used in our experiments, schematically illustrated in Fig.2-4. In the first protocol, the microbubbles were imaged during ultrasound application and included the following steps (1) baseline fluorescence imaging performed with sequential excitation at 340 nm, 380 nm and 539 nm for 20 s; (2) baseline bright field high-speed imaging performed for 10 ms; (3) ultrasound application during the high-speed imaging; (4) fluorescence imaging continued with the same excitation sequence for up to 5 min. Synchronization of ultrasound pulse and bright field imaging ensured that bright field images would be acquired before, during, and after the ultrasound pulse. Immediately after the bright field imaging was completed, the microscope was manually switched back to the fluorescence camera, which continued to run throughout the bright field

imaging to maintain a continuous time base during the entire duration of the experiment. Since light could only be directed to one camera at a time, the information from the fluorescent dyes is not captured during the time when the ultrasound pulse is applied and the bright field imaging is performed.

The second protocol involved only fluorescence imaging without the bright field imaging. In addition to excitations at 340 nm, 380 nm and 539 nm, fluorescence imaging in the second protocol also included excitation at 360 nm, the isosbestic wavelength of fura-2, to investigate the leakage of the pre-loaded fura-2 out of the cell due to sonoporation of the cell membrane. At the isosbestic point of the dye, the fluorescent emission is independent of the $[Ca^{2+}]_i$. As such, this wavelength was used as a measure of fura-2 dye concentration [160-162].

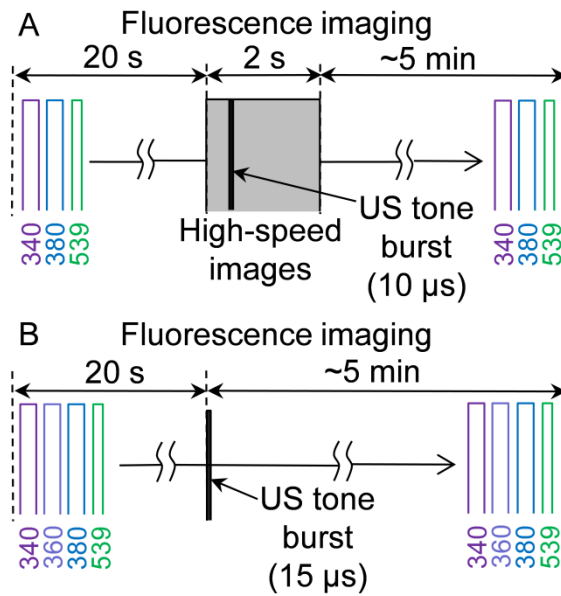


Figure 2-4 Schematic diagram of experimental protocols for monitoring intracellular delivery and calcium transients generated by ultrasound-driven microbubbles.

2.2.8 Curve fitting

Following a previous proposed model [163, 164], the change in PI intensity due to PI uptake was fitted to a two-parameter exponential recovery function

$$PI(t) = PI_{\infty}[1 - \exp(-t/\tau_{PI})] \quad \text{Equ. 2-2}$$

where $t = 0$ is the time of the ultrasound application, τ_{PI} is the characteristic PI recovery time and PI_{∞} is the asymptotic PI intensity at long times. Analogously, intensity changes due to fura-2 dye loss measured with the 360 nm excitation were fitted to a two-parameter exponential decay function

$$F_{360}(t) = F_{360}^{\infty} + (F_{360}^0 - F_{360}^{\infty})\exp(-t/\tau_{F360}) \quad \text{Equ. 2-3}$$

where τ_{F360} is the characteristic decay time for fura-2 dye leakage and F_{360}^0 and F_{360}^{∞} are the initial fura-2 intensity from 360 nm excitation before ultrasound exposure (known) and the asymptotic fura-2 intensity at long times. Fitting was performed using the routines of the MATLAB Curve Fitting Tool using the default parameter on all data except those with signal-to-noise ratios so low that meaningful fitting was not possible. Goodness-of-fit was assessed using the R^2 parameter (ratio of the sum of squares of the regression and the total sum of squares).

At each experimental condition, multiple experiments were conducted. The number of experiments are indicated where the results are reported.

2.3 Results

2.3.1 Ultrasound-driven microbubble activities, sonoporation, and calcium transients

In the set of experiments using the first protocol, microbubble dynamics were observed using the high-speed camera during the application of ultrasound while the intracellular delivery of the marker PI from the extracellular solution and the $[Ca^{2+}]_i$

response were measured using real-time fluorescence imaging. Control experiments with no microbubbles or no ultrasound yielded no PI uptake. Only those microbubbles that were immediately adjacent to the cell resulted in any observable changes in the cells. Figure 2-5 shows the results of a typical experiment. Figures 2-5A and 2-5B show pre-ultrasound PI and $[Ca^{2+}]_i$ (pseudocolor) images superimposed on the bright field image of the same FOV taken prior to the start of the fluorescence imaging and ultrasound application with the region of interest indicated by the solid white lines on the main body of two cells. Cell 2 is adjacent to a microbubble (indicated by the arrow) while Cell 1 is not. The absence of PI in cells (no red in Fig.2-5A) indicates their viability with intact membrane (the extracellular solution contains PI). After initial baseline fluorescence imaging, the microscope is switched to the high-speed brightfield imaging followed by ultrasound application. Figures 2-5C and 2-5D show the mean PI fluorescence intensity and $[Ca^{2+}]_i$, respectively, as a function of time for the regions of interest corresponding to Cells 1 and 2 in Fig.2-5A and 2-5B. The significant increase of PI intensity in Cell 2 is clearly shown in Fig.2-5C, indicating intracellular PI delivery via sonoporation. Figure 2-5D shows that the average $[Ca^{2+}]_i$ also increases significantly in Cell 2 before eventually returning to an equilibrium value. The return of the $[Ca^{2+}]_i$ of Cell 2 to an equilibrium value suggests that the cell is still alive even though delivery has occurred. Figure 2-5E shows the ultrasound-induced stimulation of the microbubble adjacent to Cell 2. The bubble is seen to fragment into three smaller bubbles resulting from the ultrasound pulse. In contrast, both PI fluorescence intensity and the $[Ca^{2+}]_i$ are essentially unaffected for the nearby Cell 1 in the absence of bubble activities in close proximity.

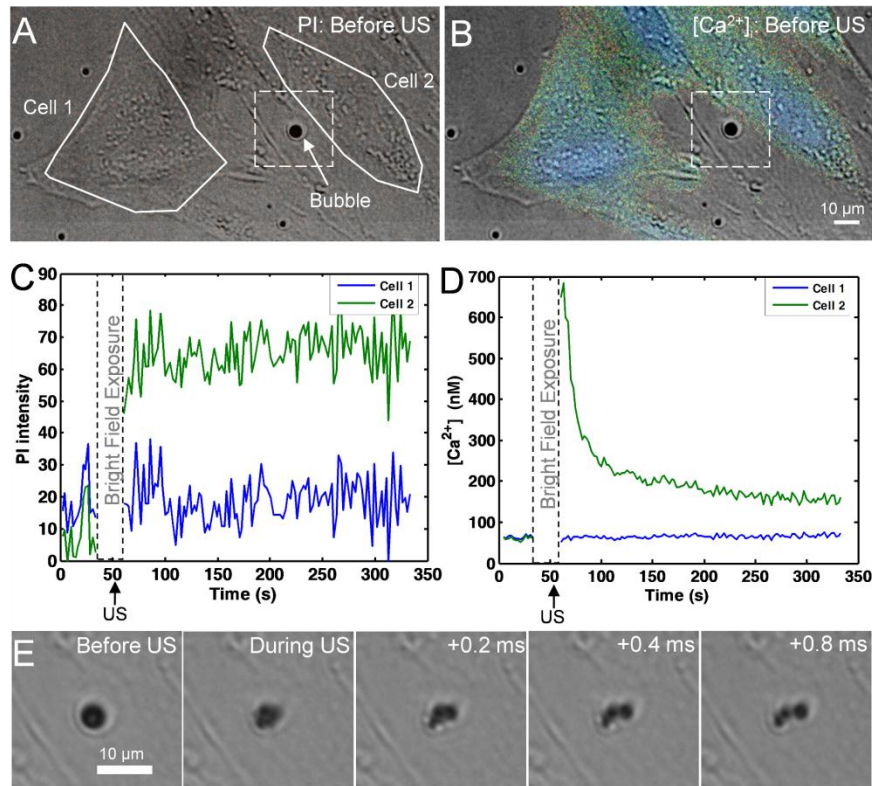


Figure 2-5 Propidium iodide (PI) delivery and intracellular $[Ca^{2+}]_i$ transients are temporally correlated with ultrasound-driven microbubbles. (A) Bright field image with superimposed PI fluorescence image before ultrasound application. No PI is observed in the cells. The solid lines show two regions of interest within cells (Cell 1 and Cell 2). The arrow points the microbubble next to Cell 2. (B) Bright field image with superimposed pseudocolor $[Ca^{2+}]_i$ image, indicating the initial $[Ca^{2+}]_i$ distribution before ultrasound application. (C) PI fluorescence intensity changes (from the baseline) as a function of time for Cells 1 and 2 induced by ultrasound simulation of the microbubbles. (D) $[Ca^{2+}]_i$ changes for Cells 1 and 2 as a function of time. In C and D, the break indicates the period when light was directed to the high speed camera. (E) High-speed camera recordings of the ultrasound-driven microbubble inside the dashed frames in (A) and (B) show bubble fragmentation.

2.3.2 Spatiotemporal evolution of intracellular marker and calcium

Figure 2-6 shows spatiotemporal evolution of the intracellular PI (Fig.2-6A) and $[Ca^{2+}]_i$ changes (Fig.2-6B), corresponding to the traces of Figs.2-5C and 2-5D. The white lines show the of the regions of interest corresponding to Cell 1 and Cell 2 while the location of the microbubble before ultrasound is indicated by the small circle. Figure 2-

6A shows that the PI delivery originates in the immediate vicinity of the microbubble at the time of the ultrasound application and then diffuses to the other areas of Cell 2 over the next 4 minutes, while Cell 1 is entirely unaffected. Figure 2-6B shows that the $[Ca^{2+}]_i$ increases from less than 100 nM to more than 500 nM and then recovers. Again, the $[Ca^{2+}]_i$ of Cell 1 is unaffected. Taken together, Figure 2-5 and 2-6 illustrate that PI delivery and change in $[Ca^{2+}]_i$ are spatially and temporally correlated in cell sonoporation due to an ultrasound-stimulated microbubble.

$[Ca^{2+}]_i$ transients and PI fluorescence changes induced by ultrasound-stimulated microbubbles like those seen in Figs.2-5 and 2-6 were observed in 18 independent ultrasound experiments (exposures) with 28 different cells each with one adjacent microbubble. In every case of PI delivery, $[Ca^{2+}]_i$ changes also occurred simultaneously. While the individual bubble oscillations were not resolved, the high-speed bright field imaging clearly showed a change in the bubble after each ultrasound pulse.

This simultaneous occurrence of microbubble changes, PI uptake, and $[Ca^{2+}]_i$ transients indicates transient pore formation induced by the microbubble stimulation is likely the cause for the observed $[Ca^{2+}]_i$ transients.

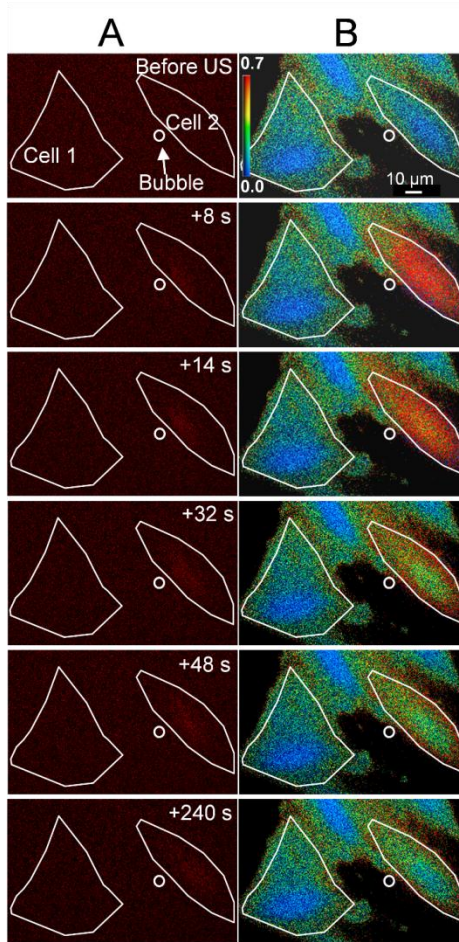


Figure 2-6 Intracellular delivery of propidium iodide (PI) and intracellular $[Ca^{2+}]_i$ transients are spatially correlated with stimulation of microbubbles by ultrasound. (A) Time-lapse PI fluorescence images and (B) pseudocolor $[Ca^{2+}]_i$ images, corresponding to the traces shown in Fig.2-5C and D respectively. The solid lines show the two regions of interest (Cell 1 and Cell 2), while the circle outlines microbubble next to Cell 2 at the beginning of the experiment. The color bar indicates the $[Ca^{2+}]_i$ in μM . The first row shows the cells before ultrasound exposure while the subsequent rows show the cells at the indicated times after ultrasound application.

2.3.3 Delayed calcium transport in cells without pore formation

While the results described above demonstrated that immediate $[Ca^{2+}]_i$ transients are correlated with PI delivery in cells affected by ultrasound-driven microbubble activities, cells with delayed $[Ca^{2+}]_i$ transients showed no PI uptake. Figure 2-7 shows the spatiotemporal evolution of the PI delivery (Fig.2-7A) and the changes in $[Ca^{2+}]_i$ (Fig.2-7B) for five cells and corresponding time traces (Fig.2-7C and D). Prior to the application

of ultrasound, no cells exhibited PI fluorescence and all the cells showed normal levels $[Ca^{2+}]_i$. However, immediately after the ultrasound is applied, only Cell 1 exhibited a calcium transient with PI delivery (in red) indicating sonoporation on the right side of the cell. Subsequently, the nearby Cells 2–5 showed an increase in $[Ca^{2+}]_i$ with delays of 6 s, 6 s, 12 s, and 42 s, respectively, but exhibited no sign of PI delivery. After 140 s, all cells had returned to their equilibrium $[Ca^{2+}]_i$ except Cell 1. It is noted that the amplitude of the increase in $[Ca^{2+}]_i$ in sonoporated cells is much higher than those in cells with delayed change in $[Ca^{2+}]_i$ due to calcium waves.

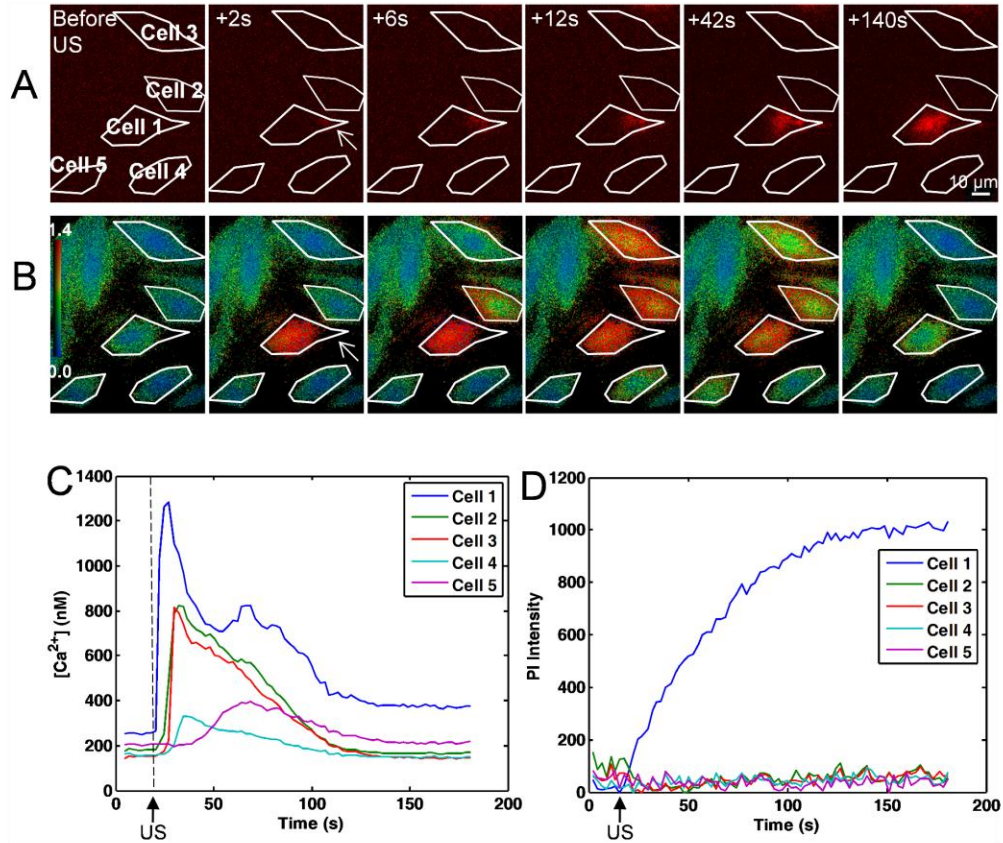


Figure 2-7 (A) Time-lapse sequence of PI fluorescence images and (B) time-lapse sequence of pseudocolor $[Ca^{2+}]_i$ images for five cells, where the color bar in row B indicates the $[Ca^{2+}]_i$ in μM . Only Cell 1 (arrow) shows immediate $[Ca^{2+}]_i$ change at the time of ultrasound and immediately PI uptake are seen in only cell 1 (arrow pointed). Cells 2 to 5 show delayed $[Ca^{2+}]_i$ transients without any PI uptake. (C) $[Ca^{2+}]_i$ as a function of time for Cells 1–5, showing the immediate change in calcium (cell 2) and delayed calcium change (cells 2–5). The $[Ca^{2+}]_i$ returned to a higher level than initial $[Ca^{2+}]_i$ for Cell 1, while all the delayed cells returned to approximately their initial level. (D) PI intensity change as a function of time for Cells 1–5. Only Cell 1 shows any PI uptake.

2.3.4 Concentration-gradient driven, bidirectional transport of markers and pore closure

With clear evidence for the correlation between marker delivery, calcium changes, and microbubble activity, a second set of experiments was performed to focus on sonoporation quantification. A series of 15 independent experiments were performed using the same approach as in the previous section using the second protocol with the

additional excitation at the 360 nm as an independent measure of the fura-2 dye concentration. For a total of 36 different cells, in all but one of the cells, simultaneous PI uptake and $[Ca^{2+}]_i$ transients were observed immediately after ultrasound exposure. In one case, no PI uptake was detected but a small immediate $[Ca^{2+}]_i$ transient still occurred. It is possible that PI uptake may have still occurred but may have been below the detection threshold of our system ($[Ca^{2+}]_i > 20.4$ nM and under PI intensities > 20.4 units).

First, the effect of sonoporation on the post-ultrasound equilibrium values of the delivery marker and $[Ca^{2+}]_i$ was considered, where five minutes was empirically determined to be a sufficient time period for most cells to reach equilibrium or near-equilibrium conditions. Figure 2-8 shows scatter plots of $[Ca^{2+}]_i$ change (max $[Ca^{2+}]_i$ increase or $[Ca^{2+}]_i$ increase at 5min = $[Ca^{2+}]_i(t = 5 \text{ min}) - [Ca^{2+}]_i(t = 0 \text{ min})$) and PI intensity changes = $PI(t = 5 \text{ min}) - PI(t = 0 \text{ min})$. Only $[Ca^{2+}]_i$ increase at 5min and PI intensity increase at 5 mins are positively correlated (linear correlation coefficient $R = +0.91$), showing both that sonoporation caused marker delivery and that increased delivery resulted in increased level of $[Ca^{2+}]_i$ long (5min) after the ultrasound exposure had ended.

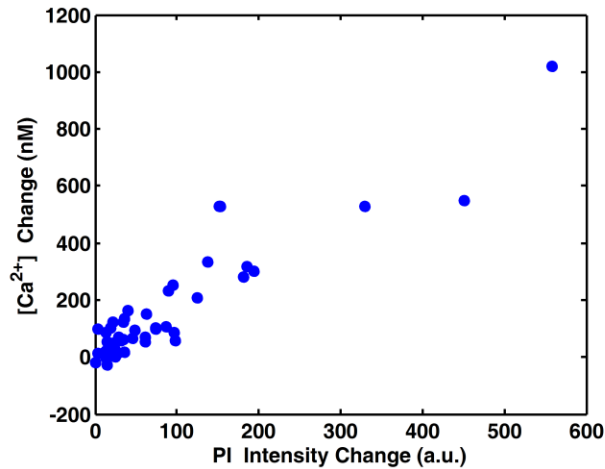


Figure 2-8 Scatter plot of $[Ca^{2+}]_i$ change and PI intensity change, both at 5 min since the start of fluorescence imaging for 36 cells, showing positive correlation ($R = +0.91$).

Next, the effect of sonoporation on the pre-loaded dye fura-2 was investigated. If sonoporation creates non-specific pores, then the preloaded dye might leak out of the cell as the delivery marker PI is transported into the cell.

Figure 2-9A shows the typical result from sonoporated cells with the isosbestic point excitation included. The PI intensity increases in the cell after ultrasound application, indicating marker delivery due to pore formation. At the same time, the $[Ca^{2+}]_i$ transiently increases and then decreases to an equilibrium level. Finally, the emission from 360 nm excitation decreased, implying a loss of fura-2 dye from the cell and thereby also indicating the existence of pore on the cell membrane. (Recall that the ratio of the emission intensities due to excitations at 340 nm and 380 nm is used to derive $[Ca^{2+}]_i$ and is thus essentially independent of dye concentration.)

The dashed lines on the figure (Fig.2-10A) show the fit of the PI uptake to Eq.2.2 ($\tau_{PI} = 34.2$ s, $PI_{\infty} = 58.4$) and fura-2 dye loss to Eq.2.3 ($\tau_{F360} = 13.8$ s, $F_{360}^{\infty} = 166$). Figure 2-9B shows that the change in the emission intensity from the 360 nm excitation F_{360} change = $F_{360}(t = 5 \text{ min}) - F_{360}(t = 0 \text{ min})$ is negatively correlated with the PI

intensity change = PI ($t = 5$ min) – PI ($t = 0$ min) in these experiments ($R = -0.78$), indicating that amount of marker delivery is related to the amount of dye loss. Using the fitting Eq.2.2 and Eq.2.3, the mean and standard deviation of the exponential recovery time constant τ_{PI} for PI was found to be 50 ± 32 s, while the mean and standard deviation of the exponential decay time constant τ_{F360} for the fura-2 dye loss was 25 ± 15 s. Although the exponential time constants depend on a combination of factors, the asymptotic behavior of fluorescence intensities of PI and fura-2 (excited at 360 nm) suggests that the time constants reflect the resealing rate of the pores on the cell membrane.

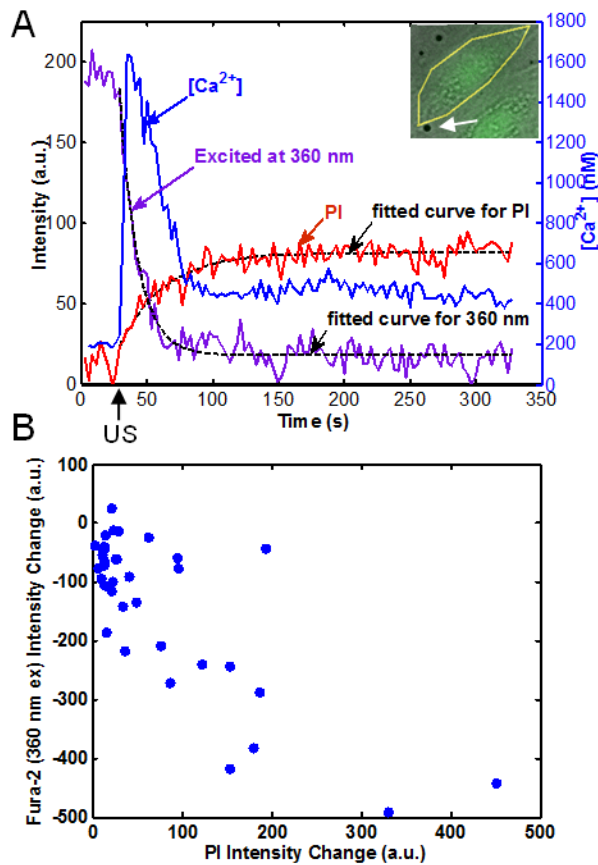


Figure 2-9 Pore generation is corroborated by simultaneous PI uptake, $[Ca^{2+}]_i$ increase, and fura-2 dye loss. (A) Changes in PI fluorescence intensity, $[Ca^{2+}]_i$, and fura-2 fluorescence intensity from excitation at 360 nm as a function of time, as induced by ultrasound-driven microbubbles for the cell shown in the inset (arrow pointing to microbubble), indicating increase in $[Ca^{2+}]_i$, PI uptake, and fura-2 dye loss generated by ultrasound application. Dashed lines show fitting of PI uptake and fura-2 loss to exponential recovery or decay models. (B) The change of fura-2 intensity from excitation at 360 nm and change of PI intensity change, both at 5 min since the start of fluorescence imaging for 36 cells are negatively correlated ($R = -0.78$), indicating loss of fura-2.

2.3.5 Cell viability

All of the cells affected by ultrasound-bubble included in this study (no data were excluded) and presented above were viable at the end of the 5 minute observation period after ultrasound application because they met the following conditions: (1) its ultrasound-induced $[Ca^{2+}]_i$ rises and then returns to an equilibrium value (although it may not necessarily be its initial value), (2) the PI intensity reaches a stable plateau which is much

lower than the PI intensity exhibited by the cells that were dead (verified by Trypan blue assay) before ultrasound application, shown in Fig.2-10, and (3) the fura-2 emission intensity due to 360 nm excitation (when bright-field imaging was not performed) drops but reaches a non-zero equilibrium value that is higher than the final equilibrium fluorescence intensity exhibited by the cells that were dead before ultrasound application (confirmed by Trypan blue assay).

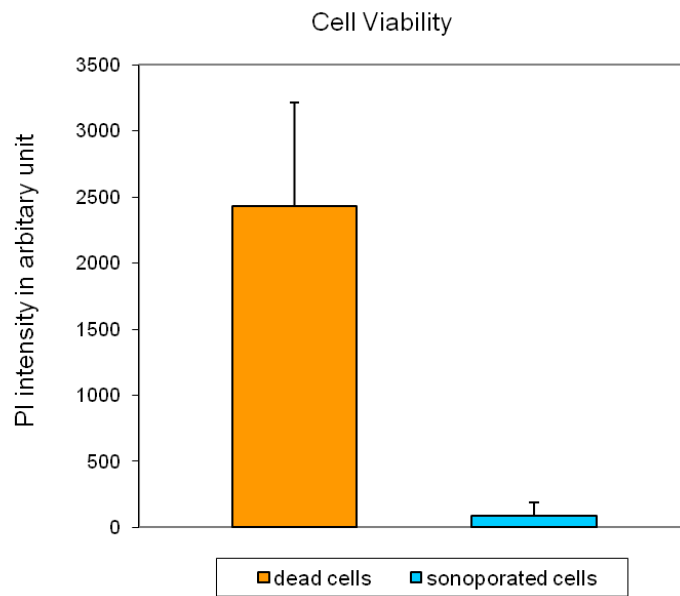


Figure 2-10 PI intensity difference in sonoporated but surviving cells (N=35), and dead cells (N=15), which were confirmed by Trypan blue staining.

2.4 Discussion

Previous studies without microbubbles [133] and with microbubbles [124, 156] have shown that cells increase $[Ca^{2+}]_i$ when $[Ca^{2+}]_{out} > [Ca^{2+}]_i$ but show no change or decrease in $[Ca^{2+}]_i$ when $[Ca^{2+}]_i > [Ca^{2+}]_{out} = 0$. Both of these responses are consistent with Ca^{2+} transport into the cell through nonspecific pores, but existence of physical pores of membrane disruption, e.g., indicated by concomitant delivery of a membrane-impermeable marker from the extracellular solution, was not explicitly demonstrated. In

the current study, the spatiotemporal correlation between the microbubble and change in PI fluorescence and $[Ca^{2+}]_i$ (Fig.2-5 and Fig.2-6) in sonoporated cells indicate that the ultrasound-driven microbubble is the cause for the $[Ca^{2+}]_i$ transients in these cells. However, it is possible that other intracellular mechanisms can also be triggered subsequently by the pore formation (e.g., calcium-induced calcium release controlled by the $InsP_3R$ and RYR families), as has also been suggested by others [135]. In general, the recovery of $[Ca^{2+}]_i$ is mostly likely the result of several complex processes. The Ca^{2+} -ATPase pumps and Na^+/Ca^{2+} exchangers on cell membranes extrudes Ca^{2+} to the outside whereas the sarco-endoplasmic reticulum ATPase pumps and mitochondria accumulate Ca^{2+} into the internal stores [165, 166].

No distinguishable difference of $[Ca^{2+}]_i$ transients and PI intensity change exhibited between two bubble reaction groups: shrink and fragment, nor clear trend were shown $[Ca^{2+}]_i$ transients and PI intensity change as a function of bubble diameter reduction in the case of shrink. This may be explained as sonoporation is complicated system, although ultrasound excited bubble reaction plays the key role in the whole process, it's the only determining factor for the outcomes. The natural variations of endoplasmic reticulum, sarcoplasmic reticulum and mitochondria quantity and distribution in individual cells may lead to various $[Ca^{2+}]_i$ transients responses, while the variations of intracellular RNA or DNA may result into different PI intensity changes. In addition to the aspect of variation in cells, the bubble location on cell membrane, and the distance of bubbles to cell surface was not under precious control in current setting, where the contact of microbubble and cell surface was generated by buoyancy of microbubbles and confinement of the OptiCell™ upper membrane. If more sophisticated

strategy can be used better control the relative position of microbubbles and cell membrane, we could improve the controllability of sonoporation outcomes.

Cells with delayed $[Ca^{2+}]_i$ transients with respect to the cells with immediate $[Ca^{2+}]_i$ transients generated by ultrasound-driven microbubble as well as PI uptake showed no PI delivery (Fig.2-7), indicating that the delayed transients are not directly due to pores on the membrane, but result from “calcium waves”, as observed previously in a different cell type [154, 156]. Hence $[Ca^{2+}]_i$ transients alone are not a good indicator for permeabilization in sonoporation for intracellular macromolecule delivery. Tsukamoto et al. [155] similarly have observed the existence of calcium transients delayed with the respect to the time of ultrasound application, particularly in cells adjacent to cells that exhibited membrane rupture (as determined by an irreversible decrease in the 380 nm excitation signal of fura-2). In studies on a variety of cells, $[Ca^{2+}]_i$ transients have been shown to result from both intracellular [167] and extracellular transport of messengers [168].

A recent study showed that delivery by endocytosis can also occur as a result of ultrasound exposure, particularly for larger weight molecules ($> 150k$ Da) [121]. Imaging from the current study showed that the intracellular PI delivery was only seen initially at the area adjacent to the ultrasound-driven microbubble, despite the fact that the entire FOV is exposed to ultrasound. The PI fluorescence gradually became increasingly distributed inside the cell, and calcium changes also rapidly occur throughout the cell. These observations are inconsistent with the localization within vesicles that is observed in endocytotic delivery. Instead, it is more likely that ultrasound mediated intracellular delivery of PI observed in our experiments results from the passive transport of

macromolecules into the cytosol through non-specific pores and/or physical disruption of the membrane [13, 15, 97, 115, 169-172].

The mean 99% recovery times observed in our study from time-dependent measurements of marker intensities ($5 \tau_{PI} \approx 250$ s or $5 \tau_{F360} \approx 125$ s) are somewhat slower than those observed previously in mechanical wounding of 10 to 30 s [160-162] of murine fibroblasts, but faster than the recovery times of 600 s in some electroporation experiments based on averaging over many murine myeloma cells [163, 164]. These differences can come from a number of factors, including difference cell types, methods of membrane wounding, as well as fluorescent dye kinetics. In addition, the scatter plots of Fig.2-8 and Fig.2-9 suggest that there is a significant amount of variability in the sonoporation process in terms of the amount of marker delivery or loss. It is possible that inherent differences in nucleic acid distribution or concentration within the cell, intercellular variations in fura-2 dye loading, and differences in the size and distance of the microbubbles could contribute this variability, but effects from these individual factors were not determined.

Sonoporation has the ability to enhance the delivery of large-molecular weight drugs, genes, and proteins to cells, but pore formation in the cell membrane may also result in other cellular events such as calcium transients or waves as well as hyperpolarization induced by calcium or stretch activation of ion channels [135, 136, 138, 173]. It has been suggested that arrhythmogenic changes that have been clinically observed during echocardiography [174, 175] may result from calcium transients [124, 135]. Cardiac contractions can follow calcium-induced calcium release [176-178], and calcium transients and waves can be involved in arrhythmias [179-181]. Calcium waves

have been found in migrating tumor cells, and an anti metastatic drug has been shown to affect the calcium-wave properties of an invasive cancer cell line [68]. Another recent study has shown that even low-intensity ultrasound can induce excitation in neurons via activation of sodium-gated and calcium-gated ion channels [69], which may then also have implications for efforts to use ultrasound as a means to transiently permeate the blood-brain barrier. Although the exact consequences require further investigation, these cellular events could have important implications in many applications such as ultrasound mediated cardiac gene delivery and targeted cancer drug delivery and are thus worthy of further careful studies in order to develop sonoporation as a safe and robust strategy for drug and gene delivery.

2.5 Conclusion

Results from this study demonstrate that ultrasound-driven bubble activities generated pores on the cell membrane that resulted in the intracellular delivery of PI and changes in $[Ca^{2+}]_i$. The correlated PI gain and fura-2 loss observed in cells due to ultrasound application indicated concentration-gradient driven, bidirectional transport characteristic of non-specific pores created by the sonoporation. Cells with delayed $[Ca^{2+}]_i$ transients showed no PI uptake in cells, indicating calcium waves that originated from nearby sonoporated cells.

Chapter 3

Dynamic Activities of Microbubbles Driven by Ultrasound Exposures Correlated with Delivery Outcomes by Sonoporation

In this chapter, we describe the studies of correlating the microbubble activities driven by ultrasound exposures with sonoporation outcomes. We implemented high speed video microscopy to investigate the dynamic activities of the Definity® microbubbles (Lantheus Medical Imaging, Billerica, MA) activities driven by various ultrasound exposures. OptiCell™ (Nunc, Rochester, NY) was used to house the cells and microbubbles. We analyzed quantitatively the microbubble behaviors and established correlation of the bubble activities with the intracellular uptake using a model molecule propidium iodide (PI) and cell viability. These results provide a knowledge base to optimize sonoporation outcome.

3.1 Introduction

Ultra-fast photographs have provided insights to understand isolated single bubble behaviors near cells exposed to ultrasound pulses lasting a few microseconds [13, 14, 93, 182, 183]. However, multiple bubbles subjected to longer ultrasound exposure (seconds), which are often used in studies employing sonoporation mediated intracellular delivery [3-7, 15-17], have not been investigated in detail. These investigations require controlled experimental environment for investigating microbubble dynamics and the resulting effects. Our approach to achieve enhanced intracellular delivery is by optimizing

ultrasound-driven microbubble interaction with cells, as it is the direct cause for any delivery outcomes, rather than ultrasound parameters.

3.2 Materials and methods

3.2.1 Cell culture

Human umbilical vein endothelial cells (HUVEC) were cultured in flasks in complete human endothelial growth medium (Lonza CC-3124, Walkersville, MD) in a humidified incubator at 37°C and 5% CO₂. Before experiment, HUVEC cells were plated into OptiCell™ chamber (Nunc, Rochester, NY). HUVEC cells were cultured in the same medium in OptiCell™ for one more day. At the time of experiment, cells had reached approximately 90%-100% confluency.

3.2.2 Assessments of delivery outcomes

Intracellular uptake of propidium iodide (PI) (Sigma Aldrich, St. Louis, MO), which is cell membrane impermeable nucleic acid intercalating agent, was used to assess sonoporation. PI was dissolved in extracellular medium at the final concentration of 100 μM. To detect PI, the specimen was excited at 539 nm, and emission was detected at 610 nm. PI serves as a real-time cell membrane integrity indicator, as it only fluoresces after excitation when inside the cells.

Cell viability was assessed by calcein AM assay. Calcein AM is a cell-permeable, non-fluorescent compound. In live cell, the non-fluorescent calcein AM is converted to green-fluorescent calcein, after acetoxymethyl ester hydrolysis by intracellular esterases. Calcein AM was dissolved in extracellular medium before ultrasound at the final concentration 1 μM. To detect calcein signal, the specimen was excited at 488nm, and emission was detected at 520 nm.

3.2.3 Ultrasound exposure and microbubbles

Ultrasound setup and microbubbles were the same as described in Chapter 2, shown in Fig.2-1. A range of ultrasound conditions was employed, with peak negative pressure from 0.06 MPa to 0.8 MPa, pulse repetition frequency (PRF) -from 10 hz to 1k hz-, duty cycles (DC) -from 0.008% to 20% - and a fixed total exposure time of 1 s. During each experiment, Definity® solution was diluted in complete culture medium for HUVEC with a final concentration $\sim 10^7$ bubbles/ml. We used OptiCell™ cell culture chamber as physical confinement for Definity® microbubbles, so that microbubbles were in close contact with cells, which were attached on the inner upper membrane of OptiCell™, as illustrated in Fig.2-1C

3.2.4 Optical imaging

Bright-field imaging was performed to capture the microbubble activities driven by ultrasound using a high-speed camera (Photron FASTCAM SA1, San Diego, CA) with a frame rate 20,000 frames per second. To resolve the microbubble dynamics in microsecond scale, an ultra-fast camera (Specialised Imaging Multi-Channel Framing Camera SIM02, Herfordshire, UK) was employed with frame rate of 2,000,000 frame per second and exposure time of 100 ns.

For fluorescence imaging, a monochromator (DeltaRAMX™ PTI, Birmingham, NJ) was employed to excite the samples at 539 nm for PI and 488 nm for Calcein. The emission of specimen was filtered by a dichroic light filter (Chroma 52002, Rockingham, VT) with passbands of green and red. The fluorescent images were acquired with a cooled CCD camera (Photometrics QuantEM, Tuscon, AZ) and then artificially-colored using Matlab.

3.2.5 Data analysis

The number of bubbles present in each frame was counted manually. For aggregates of bubbles, the bubble number in each cluster was estimated by dividing the projection area of the cluster by the averaged area of a single bubble cross-section. The percentage of bubbles number change in FOV was normalized by the number of bubbles prior to ultrasound application.

To quantify the behavior of translation, a velocity threshold, $0.06 \mu\text{m}/\mu\text{s}$, was empirically set to differentiate moving and non-moving bubbles. A bubble was considered as a moving bubble if at any time point during the entire 1s ultrasound exposure, its velocity was above this threshold.

Delivery outcomes were assessed using two parameters: viability and delivery efficiency. For each ultrasound exposure, the fluorescent images of PI were acquired before and after ultrasound exposure, and calcein image was acquired post ultrasound for viability assessment. The total number of cells in the field of view (FOV) was considered as total number of cells. The percentage of calcein positive cell in the total cell number was defined as viability. The percentage of both PI and calcein positive cells (PI uptake and surviving cells) post ultrasound relative to all calcein positive cells (surviving cells) was defined as delivery efficiency.

At each experimental condition, multiple experiments were conducted. The number of experiments are indicated where the results are reported.

3.3 Results

3.3.1 Characterization of the bubble dynamics correlated with sonoporation outcomes

In our experiments, we have observed that different ultrasound parameters lead to different complex bubble dynamics and usually a mixture of bubble behaviors. To elucidate the correlation between bubble dynamics and sonoporation outcomes, bubble dynamics driven by a wide range of ultrasound conditions in entire FOV were quantitatively analyzed and categorized.

Three basic categories of bubble behaviors were identified from detailed examination of the bubble behaviors in this study: category 1, aggregation and microstreaming; category 2, violent translation; category 3, rapid collapse. Typical examples for each category are shown in Fig.3-1, Fig.3-3, and Fig.3-5. In each figure, part A provides an overview of the bubble activities before, during and post ultrasound exposure, followed by PI images before and post ultrasound and calcein image post ultrasound as the assessments of small molecule delivery outcome and cell viability. Part B and C provide details of a particular kind of bubble behavior. Ultrasound was switched on at time 0.

Driven by low acoustic pressure and relative long DC (0.06 MPa, 20 hz PRF, 20% DC, 1 s ultrasound applied for data shown in Fig.3-1), aggregation of bubbles (Fig.3-1A and B) and microstreaming built up by relatively big bubbles (Fig.3-1C) were often observed. Attracted by nearby bubbles, small bubbles gradually moved to get together to form small bubble clusters. As long as ultrasound was on, small bubble clusters can further attracted by nearby cluster to aggregate into bigger cluster (Fig.3-1B). Originating from the oscillation of a relatively big bubble, microstreaming was built up in the fluid around it, which was illustrated by the trajectories of its surrounding small bubbles carried by the microstreaming flow (Fig.3-1C). Figure 3-1C also shows that this

oscillating big bubble was poking the membrane of the adjacent cell. However, this aggregation and microstreaming bubble activities did not have any impact on PI uptake or cell viability as shown in Fig.3-1A.

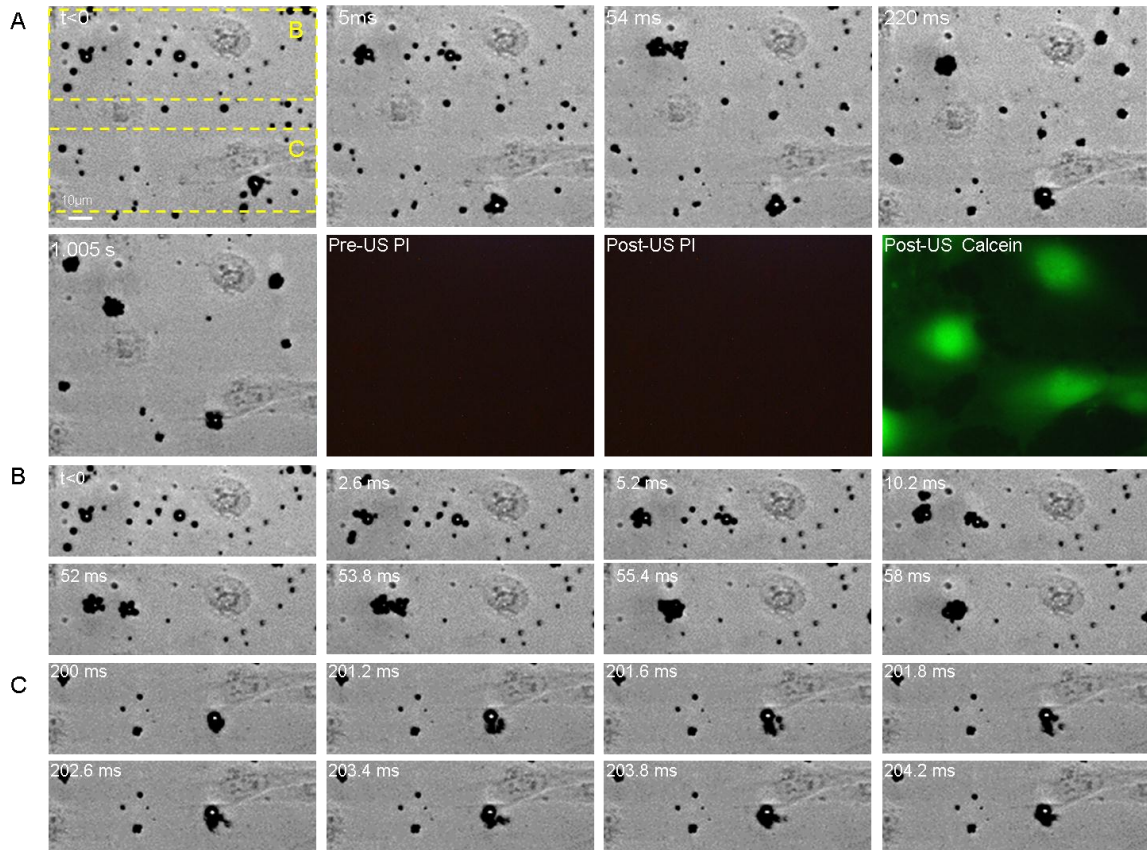


Figure 3-1 A typical example of Definity® microbubbles behavior category 1: aggregation and microstreaming. In this example, Definity® microbubbles were suspended in OptiCell™, driven by 1M hz transducer, with 0.06 MPa, 20 hz PRF, 20% DC (10 ms in each pulse), 1s exposure totally. Panel (A) shows selective bright field images of a 216 µm×180 µm area before, during and immediately post ultrasound application, followed by fluorescence images excited at 538 nm before and post ultrasound for PI signals, and fluorescence images excited at 488 nm for calcein signal post ultrasound. Two sub-areas are selected in panel (A), labeled as (B) and (C), showing microbubbles aggregation and microstreaming respectively. More temporal information was shown in panel (B) and (C) accordingly.

In order to quantitatively describe the bubble dynamics in the data shown in Fig.3-1, we measured two parameters: the total bubble number change in FOV as a function of time and cluster size before ultrasound and at 1s (Fig.3-2). As shown in

Fig.3-2A, there was no significant bubble number change over 1s ultrasound exposure. While aggregation was demonstrated by the growth of cluster size shown in Fig.3-2 B. Before ultrasound, microbubbles were evenly distributed in the FOV, as 160 bubbles out of 175 bubbles were individual bubbles without touching with any other bubbles. By comparison, after 1s ultrasound exposure, many bubble clusters formed, with bubbles number per cluster varying from 2-37(Fig.3-2 B).

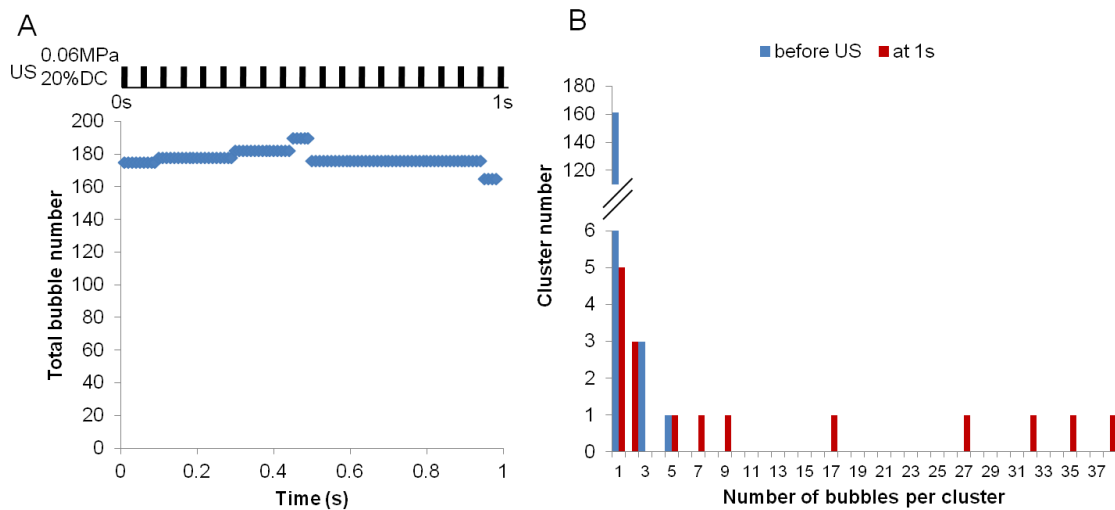


Figure 3-2 Quantitative analysis of Definity microbubbles dynamics in the data shown in Fig.3-1. (A) Total bubble number change in the FOV as a function of time over 1s ultrasound exposure. (B) Histogram of cluster size before ultrasound and at 1s.

With much higher acoustic pressure and long DC, the second category of bubble dynamics: coalescence and translational movements were results, as shown in Fig.3-3 (0.43 MPa, 20 hz PRF, 20% DC (10ms in each pulse), 1 s ultrasound was applied to the data shown in Fig.3-3). Once ultrasound was on, bubble coalesced right the way. Small bubbles coalesced into big bubbles; big bubbles further coalesced into even bigger bubbles (Fig.3-3B). Due to this strong attraction between bubbles, coalescence was accompanied with violent translation. The coalesced big bubbles crazily moved around

while wildly oscillating, intruding into cells on its pathway, tearing apart cell membranes, and forcing cells detach from the bottom immediately (Fig.3-3A and C). This violent translation movement was devastating to the cells on their pathway, resulting in massive cell death immediately after ultrasound exposure (Fig.3-3A). Although the total ultrasound duration applied for data shown in Fig.3-3 was 1 second, all microbubbles disappeared once the 1st ultrasound pulse was off, making all the following ultrasound pulses useless in terms of delivery outcomes.

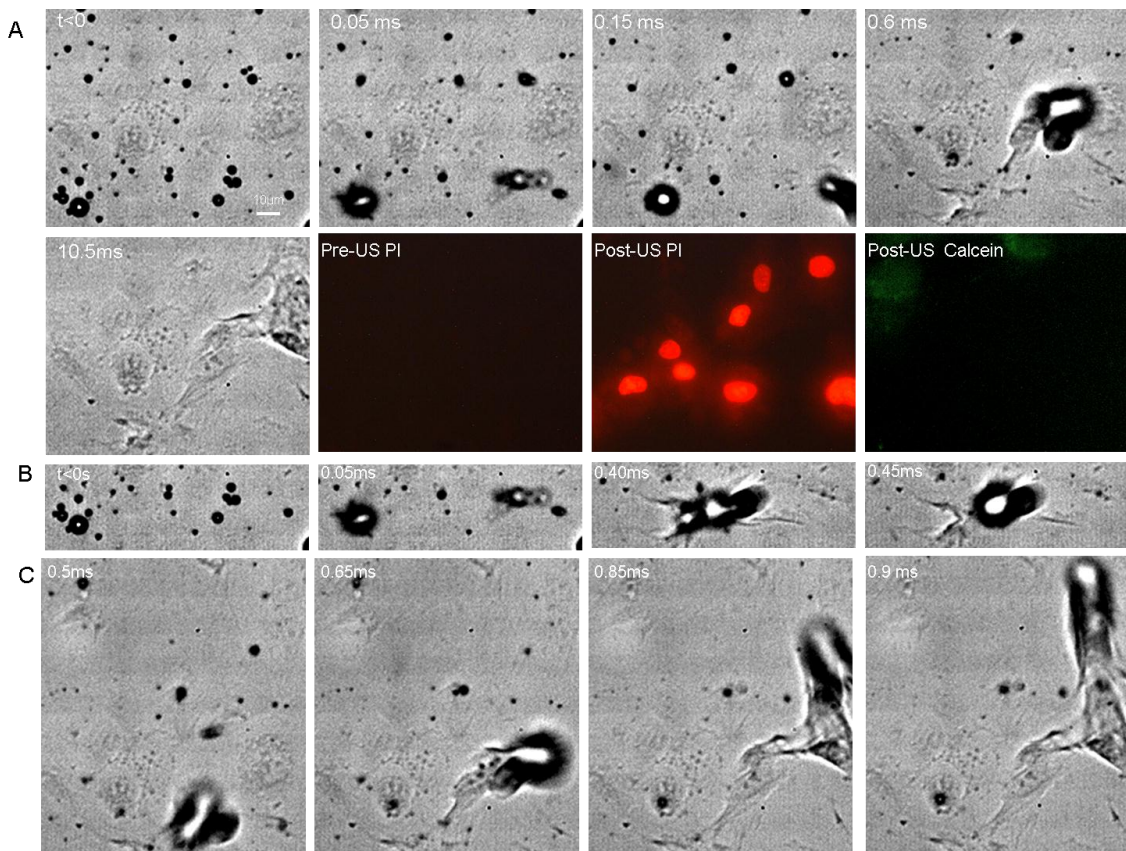


Figure 3-3 A typical example of Definity® microbubbles behavior category 2: coalescence and translation. In this example, Definity® microbubbles were suspended in OptiCell™, driven by 1Mhz transducer, with 0.43 MPa, 20 hz PRF, 20% DC (10 ms in each pulse), 1s exposure totally. (All bubble disappeared immediately after 1st ultrasound.) Panel (A) shows selective bright field images of a 216 μm×180 μm area before, during and immediately post ultrasound application, followed by fluorescence images excited at 538 nm before and post ultrasound for PI signals, and fluorescence images excited at 488 nm for calcein signal post ultrasound. Panel (B) and (C) are sub-areas shown in the image of Panel (A), with more temporal information, illustrating coalescence in (B) and newly fused big bubble fast translating while violently oscillating in (C).

In order to quantitatively describe the bubble dynamics in the data shown in Fig.3-3, we measured two parameters: the total bubble number in FOV as a function of time and the percentage of moving bubbles in FOV as a function of time, shown in Fig.3-4. The time periods shown in Fig.3-4 were from -0.5ms up to 10ms, as after 1 ultrasound pulse (10ms) no bubble existed any more. There was a sudden drop of bubble number within the first 0.05ms (from 250 to 170), which may be due to collapse and coalescence happened once ultrasound was on. After that, the residual bubbles were oscillating driven by on-going ultrasound and gradually shrinking, which may be due to passive diffusion; while the coalesced big bubbles were moving around fast and absorbed/fused with small bubbles along their moving paths. These may explain the gradual decreasing of bubble number between 0.5ms to 10ms, shown in Fig.3-4A. Once ultrasound was turned off at 10ms, all bubbles immediately disappeared.

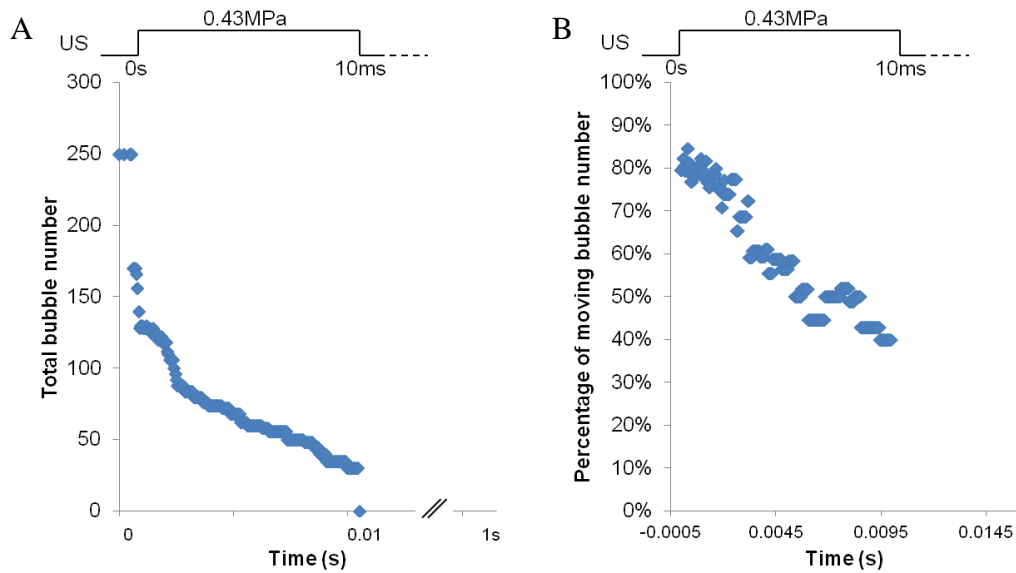


Figure 3-4 Quantitative analysis of Definity microbubbles dynamics in the data shown in Fig.3-2. (A) Total bubble number change in FOV as a function of time over 10ms. (B) Percentage of moving bubble change as a function of time over 10ms.

High pressure with very short pulse duration created the third bubble dynamics case, rapid collapse. As typical example shown in Fig.3-5A (0.43 MPa, 10 hz PRF, 0.008% DC (8 μ s in each pulse), 1 s ultrasound was applied to data shown in Fig.3-5A), with minimal translational movement, bubble size gradually decreased during ultrasound exposure. The sonoporation outcomes show that there were some cells exhibiting PI uptake and surviving. As the ultrasound only lasted 8 μ s, 20,000 fps frame rate is not sufficient to resolve the details during ultrasound-on time; therefore ultra-fast camera was applied to supplement the details information. Figure 3-5 (B-D) are ultra-fast images of Definity® microbubbles in Opticell without cell attached, driven by 0.43MPa, 8 μ s ultrasound. The images were captured at 2M frames per second, 100 ns exposure time. Figure 3-5 B-D illustrates three different bubble behaviors: oscillation (Fig.3-5B), microjet formation (Fig.3-5C) and fragmentation (Fig.3-5D). The direct observation of Fig.3-5C is vortex ring formation, which indicating a flow is penetrating the center of the ring, which is microjet.

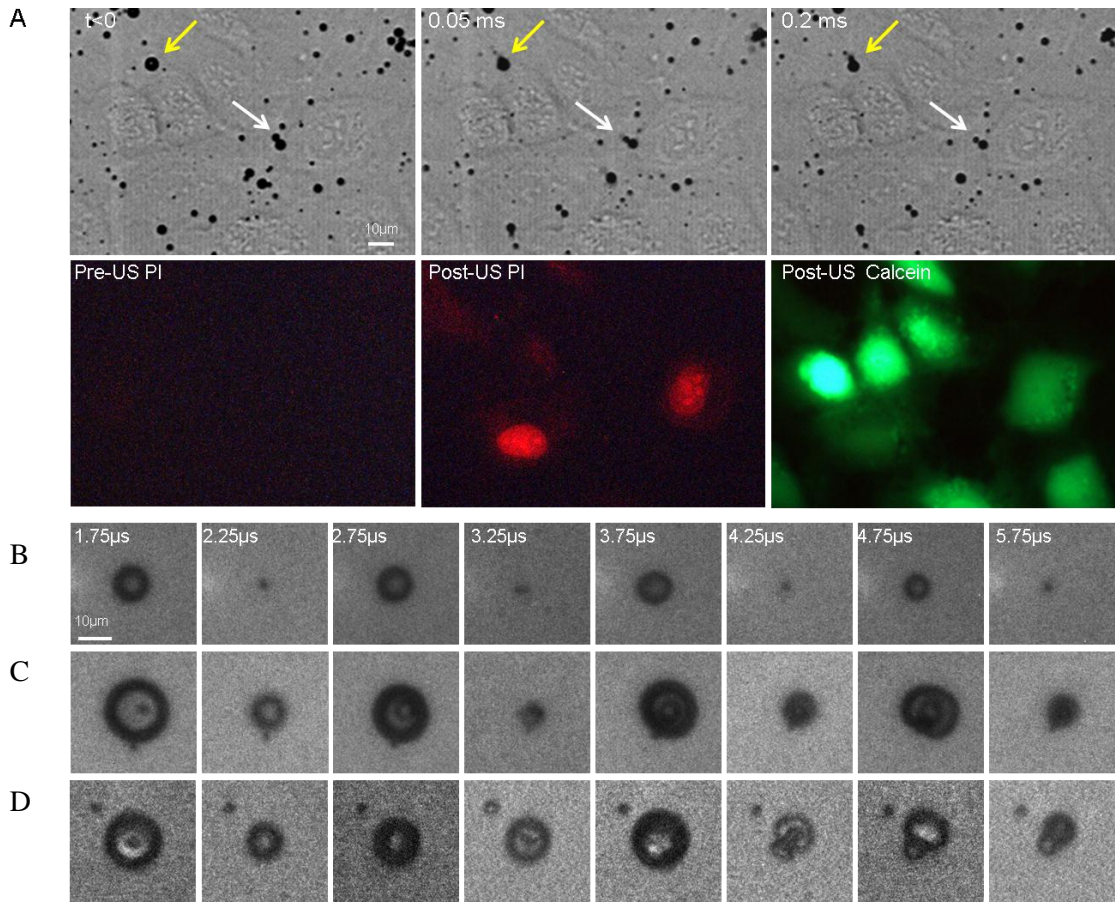


Figure 3-5 A typical example of Definity® microbubbles behavior category 3: collapse. In this example, Definity® microbubbles were suspended in OptiCell™, driven by 1Mhz transducer, with 0.43MPa, 10 hz PRF, 10 μ s (10 cycles) in each pulse, 1 s exposure totally. (All bubble disappeared after 4th ultrasound pulse.) Panel (A) shows selective bright field images of a 257 μ m \times 184 μ m area before, post 1st ultrasound pulse, followed by fluorescence images excited at 538 nm before and post ultrasound for PI signals, and fluorescence images excited at 488 nm for calcein signal post ultrasound. Panel (B-D) are ultrasound excited Definity® microbubbles images captured by ultra-fast camera with frame rate 2M fps, showing three different bubble activities during ultrasound exposure, oscillation (B), forming microjet (C) and fragment (D). The direct observation of panel (C) is vortex ring formation, which indicating a flow is penetrating the center of the ring, which is microjet. The time label and scale bar in (B) apply for (C) and (D).

In order to quantitatively describe the bubble dynamics in the data shown in Fig.3-5, we measured two parameters: the total bubble number change in FOV as a function of time and the percentage of moving bubbles change in FOV as a function of time, shown in Fig.3-6A-B. In addition, the radius change of a typical bubble in FOV was shown in Fig.3-6 C. It is shown in Fig.3-6 A that ultrasound pulse immediately destroyed

some bubbles, resulting into the sudden drop right after each ultrasound pulse. Meanwhile, some bubbles gradually disappeared during the ultrasound-off interval, which may be owing to diffusion, especially in the case when lipid shell of microbubbles was broken by ultrasound. Only when ultrasound was on, bubbles moved, but the percentage of moving bubbles (Fig.3-6B) was significantly lower than in category 2 (Fig.3-4B), as each ultrasound pulse only lasted $8\mu\text{s}$. Before a bubble completely disappeared, usually it experienced shrinking during ultrasound on and off period. A typical example of a bubble size evolution was shown in Fig.3-4C.

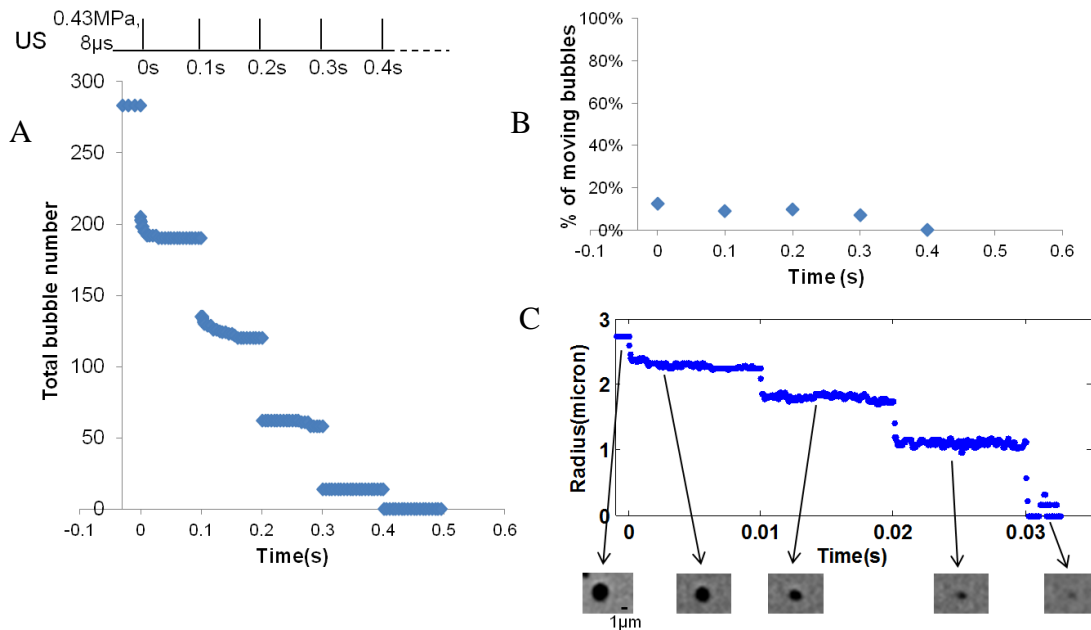


Figure 3-6 Quantitative analysis of Definity microbubbles dynamics according to the example shown in Fig.3-5. (A) Total bubble number change as a function of time. (B) Percentage of moving bubbles changes as a function of time. (C) Radius change as a function of time of a bubble in this data.

Detailed descriptions of typical examples in each category were presented above, systematic analysis and correlation with bubble dynamics and sonoporation outcome with statistic power was conducted as followed. As shown in the quantitative bubble dynamic

analysis that immediately after 1s ultrasound exposure, 96% bubbles still exist in the example for category 1 (Fig.3-2B, the data with 20 hz PRF); while 0% and 0% bubble exist in the examples of category 2 (Fig.3-4B, the data with 20 hz PRF) and 3 (Fig.3-6, the data with 10 hz PRF). Collapsing is a main reason decreasing bubble number. Therefore, the percentage of bubbles remaining in the FOV immediately after 1 s ultrasound exposure can serve as a good indicator to distinguish category 1 from category 2 and 3. Another indicator to differentiate category 2 and 3 is the number of moving bubbles during ultrasound-on time. Moving is defined as the displacement between 2 consecutive frames is larger than 6 pixels. Driven by much longer pulse in category 2 compared with category 3, the percentage of moving bubbles in category 2 was significantly larger than category 3.

Under the ultrasound conditions which created the three basic bubble dynamics categories, more data were collected and presented in Fig.3-7. For category 1, ultrasound applied was 0.06MPa, 20hz PRF, 20% duty cycle, 1s; for category 2, ultrasound applied was 0.43MPa, 20hz PRF, 20% duty cycle, 1s; and for category 3, ultrasound applied was 0.43MPa, 10hz PRF, 0.008% duty cycle, 1s (Fig.3-7). Bubble dynamics was indicated by “% of bubble remaining at 1s” and “% of moving bubbles” (Fig.3-7A). The corresponding sonoporation outcomes, including viability and delivery efficiency are shown in Fig.3-7B. Clearly shown in Fig.3-7B, these three categories have distinctive characteristic sonoporation outcomes, while category 3 has the most desirable outcomes, viability $88\pm 6\%$ (N=9) and delivery efficiency $37\pm 6\%$. By comparison, category 1 has zero delivery efficiency, and the viability for category 2 is poor ($24.1\pm 8.6\%$, N=10).

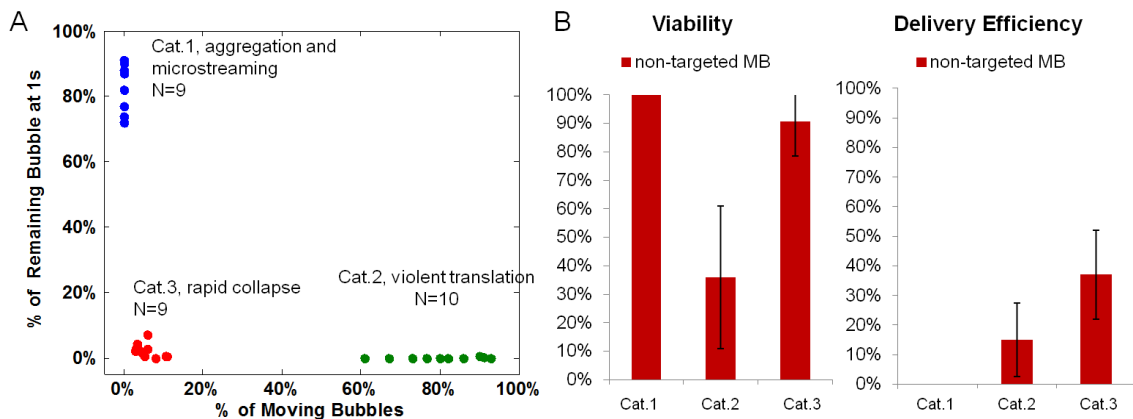


Figure 3-7 Bubble dynamics characterization (A) and the corresponding PI delivery outcomes (B) under the ultrasound conditions creating the basic three categories: Cat.1 Aggregation and microstreaming (US: 0.06MPa, 20hz PRF, 20% duty cycle, 1s); Cat.2. Coalescence and translation (US: 0.43MPa, 20hz PRF, 20% duty cycle, 1s); and Cat.3. Collapse (US: 0.43MPa, 10hz PRF, 0.008% duty cycle, 1s). Viability is defined as the number of surviving cells divided by the total number of cells in the FOV. Delivery efficiency is defined as the number of surviving and PI uptake cells divided by the total number of cells in the FOV. “N” is the number of experiments conducted.

3.3.2 Mapping sonoporation outcomes with bubble dynamics

Since sonoporation outcomes is directly determined by the bubble dynamics, and three typical bubble dynamics categories and their sonoporation outcomes have been characterized; Figure 3-8 shows that bubble dynamics and sonoporation outcomes of four data sets were mapped in the coordinate established by the three typical categories. Starting from data set 1 (0.1 MPa, 20 hz PRF, 20% DC, 1s ultrasound applied), whose bubble dynamics and sonoporation outcomes are very similar to category1, as the bubble dynamic of data set 2, 3 and 4 are approaching category 2 and category 3, their delivery efficiency increases while viability decrease. Compared with data set 2 (0.12 MPa, 20 hz PRF, 10% DC, 1s ultrasound applied), data set 3 (0.23 MPa, 20 hz, 0.4% DC (200 μ s in each pulse), 1 s ultrasound applied) is closer to category 3 in the bubble dynamics coordinate, as a result, shown in sonoporation outcome coordinate, data set 3

exhibits higher delivery efficiency than data set 2. Compared with data set 3, the bubble dynamic of data set 4 (0.23 MPa, 20 hz PRF, 20% DC, 1s ultrasound applied) is located nearer to category 2, which features low viability, therefore data set 4 displays lower viability than data set 3. These four data sets can be seen as a mixture of the typical categories. Among all the bubble dynamic groups, three typical ones, and four mixtures, category 3 “rapid collapse” shows its superior delivery efficiency, confirming that it is the preferable scenario for intracellular delivery.

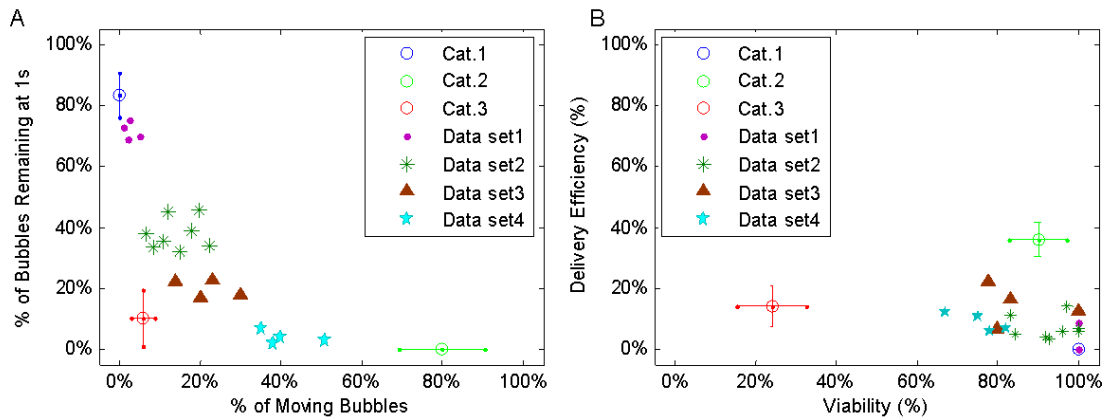


Figure 3-8 Mapping bubble dynamics (A) and sonoporation outcomes (B) of 4 data sets using the typical three categories as landmarks. The ultrasound condition for the 4 data sets are: Data set1: 0.10 MPa, 20 hz PRF, 20% DC, 1 s (N=4); Data set 2: 0.12 MPa, 20 hz PRF, 10% DC, 1s (N=8); Data set 3: 0.23 MPa, 20 hz, 0.4% DC (200 μ s in each pulse), 1 s (N=4); and Data set 4: 0.23 MPa, 20 hz PRF, 20% DC, 1 s (N=4).

3.3.3 Effects of ultrasound parameters on bubble dynamics

Bubble dynamics is resulted from all ultrasound parameters, including transducer center frequency, acoustic pressure, PRF, DC, total duration, in addition to the specific chemical and physical condition in a certain experimental setup. Figure 3-9 provides a hint about how ultrasound parameters impact the microbubble dynamics. With very short pulse duration 10 μ s, increasing acoustic pressure, bubble dynamics gradually transited from category 1 to category 3, while the moving bubble slightly increased as well (Fig.3-

9A). And with relative long pulse duration (10ms), increasing acoustic pressure, bubble dynamics gradually transited from category 1 to category 2 (Fig.3-9B). The percentage of both the destroyed bubble and moving bubbles increase with increased acoustic pressure (Fig.3-9B). Other ultrasound parameters, such as PRF, also take effects, as shown in Fig.3-9C and D. With fixed DC, lower PRF lead to more moving bubbles (Fig.3-9C) and with fixed pulse duration, higher PRF lead to more moving and destroyed bubbles (Fig.3-9D).

In a certain experiment configuration, ultrasound conditions determine bubble dynamics, and bubble dynamics determine delivery outcomes. Therefore we intended to build the connection between ultrasound conditions, bubbles dynamics and delivery outcomes. Figure 3-10 shows how acoustic pressures and duty cycles affect bubble dynamics with 20hz PRF. The three basic categories of bubble dynamics were indicated on the plot. The delivery outcomes responding to the three basic categories have been characterized (Fig.3-7). The bubble dynamics generated by different ultrasound parameter combinations can be seen as the mixture of the three basic categories. Therefore, by comparing the bubble dynamics with the basic categories, its delivery outcomes can be estimated qualitatively.

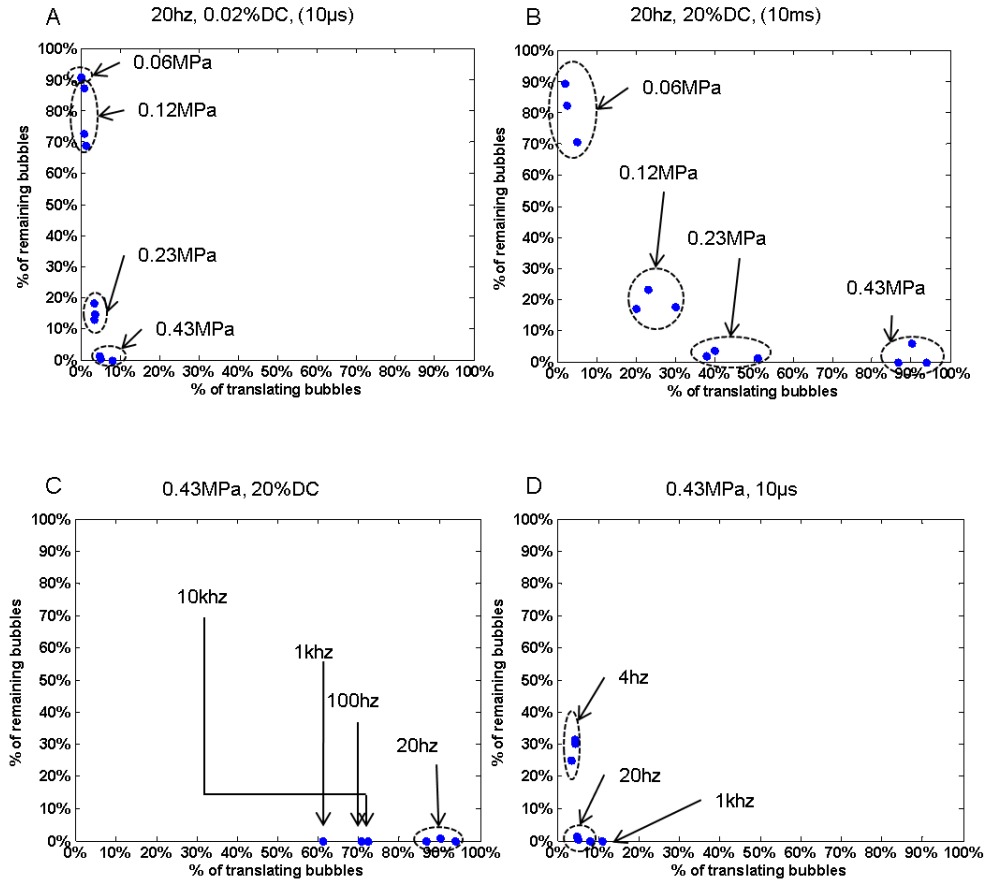


Figure 3-9 Impact of ultrasound parameters, including acoustic pressure (A and B) and PRF (C and D) to bubble dynamics

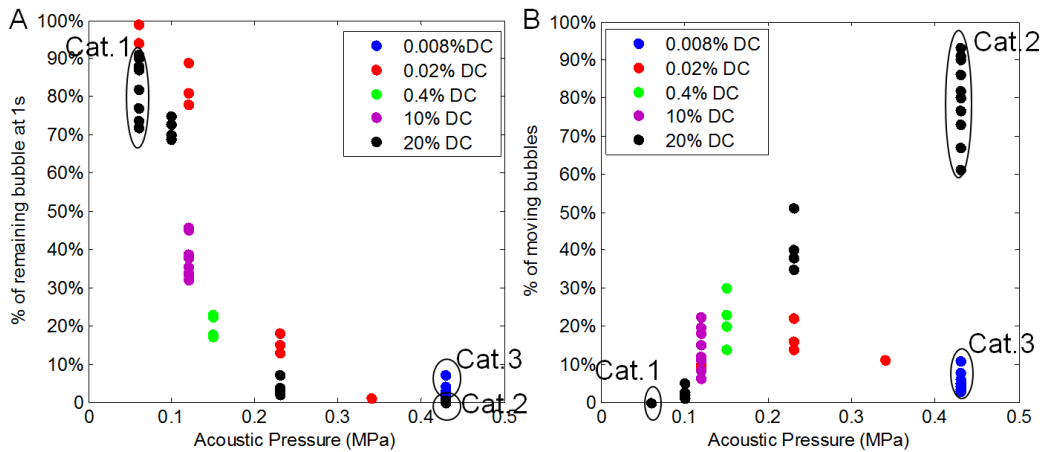


Figure 3-10 Impact of ultrasound parameter (acoustic pressure and duty cycle) to bubble dynamics. Bubble dynamics were characterized by % of remaining bubble at 1s (A) and % of moving bubbles (B). 0.008% duty cycle data were with 10hz PRF. All other data were with 20hz PRF.

In short, bubble dynamics is determined by all ultrasound parameters along with all other experimental factors. This knowledge inspires us in two perspectives. One is that the phenomenal association built up between certain ultrasound parameters and delivery outcomes without knowing bubble dynamics is isolated information and may not apply in a different experimental setting. Another is that the rational approach to promote the sonoporation delivery results is to optimize microbubble activities relative to cells.

3.4 Discussion

3.4.1 Sonoporation correlated with bubble dynamics

In this study, we conducted experiments using Definity® microbubbles in OptiCell™ configuration. The critical role of ultrasound-driven microbubbles in this setting was explicitly demonstrated by quantitative analysis of the dynamics process and precise spatiotemporal correlation with outcomes assessments. Three basic bubble dynamics categories have been identified: aggregation and microstreaming (category 1), coalescence and translation (category 2) and rapid collapse (category 3); while category 3 shows the most favorable delivery outcomes. The broad relevance of bubble dynamics permits mapping others' studies performed in a similar experimental setup using the bubble dynamics coordinate built up in this study. For example, van Wamel et al [97] provided bright field images. The bubble dynamics in their experiment can be classified into category 3. And their results confirmed that category 3 has the high delivery efficiency while good viability.

We built up a whole perspective of microbubble mediated sonoporation: bubble dynamics in the key position determining sonoporation outcomes and determined by ultrasound parameters. The ultrasound parameter studies, highly depending on the initial

protocol to start with, they are easily restricted themselves in a narrow bubble dynamics region, losing the whole picture of bubble dynamics, and therefore finding a local optimal condition. Rahim et al. [144] found that the optimal ultrasound condition is 0.25 MPa peak negative pressure with 40 cycles/pulse, with delivery efficiency 4%. However, the bubble dynamics they explored is most likely close to category 1. They did not explore the category 3, which might give them dramatically higher delivery efficiency. Moreover, it's not surprising that contradictory results can arise with the respect of ultrasound parameter on sonoporation outcomes. For example, the impact of duty cycles were reported making no difference [144] or being critical [184] on delivery efficiency. This inconsistency can be easily explained as the bubble dynamics of these two studies were in different categories. The bubble dynamics in Rahim's study [144] and Merjering's study [184] most likely close to category 1, and category 2 respectively.

3.4.2 High speed imaging and ultra-fast imaging

While ultra-fast speed photographs can capture expansion and contraction of an oscillating bubble or the evolution of a collapsing bubble with frame rate from 0.5M fps to 10M fps [13, 56, 93, 95-97, 185], our high speed camera are able to continuously record the dynamic process of bubble-cell interaction during entire 1s pulsed ultrasound exposure and reveal some relatively slow process, such as microstreaming and violent translation. Because of the continuity of ultrasound-driven bubble activities, the observation at the shutter duration on the order of nanoseconds ([13, 56, 93, 95-97, 185]) and the observation at the shutter duration at 50 microseconds (this study) are mutually complementary, as shown in Fig.3-1, Fig.3-3, and Fig.3-5. All these direct optical observation shows many different kinds of bubble behaviors. The driven force for these

behaviors may be different. The movement in the direction of ultrasound propagation is due to the primary radiation force, while the attraction or repulsion between bubbles is due to the secondary radiation force [93, 100, 108, 186].

3.4.3 Biologic relevance besides intracellular delivery

Though some bubble behaviors, such as aggregation and mild oscillation, are not inducing intracellular delivery, they may have other therapeutic applications. Microfoam formation in capillary due to aggregation has been studied and suggested to be used to block the entire vessels on purpose [187]. At very low intensity of ultrasound exposure, mild oscillation was demonstrated to increase calcium ion permeability, intracellular H₂O₂ level, protein nitrosylation, rearrangement of F-actin cytoskeleton, as well as reversible change of monolayer integrity, which was suggested to have potential application in control gene expression and trigger vascular angiogenesis [126]. Mild translation can be used to displace targeted contrast agents to a vessel wall, increasing binding efficiency between targeted contrast agents and available surface receptors for ultrasonic molecular imaging [188].

3.4.4 Different experimental setting results in different bubble dynamics

In this study, experiments were performed in an OptiCell™ cell chamber, where bubbles are in close proximity of cells before ultrasound. Therefore, the specific knowledge about bubble dynamics categorization is limited in a similar setup. A lot of *in vitro* sonoporation studies were conducted in dishes or tubes with cell suspension [15, 115, 189]. In this case, long-time translational movement of bubbles may be desirable, as it can create streaming flow, carrying bubbles to the close vicinity of cells. In addition, in the case, where delivery efficiency was considered in the larger area, for example, entire

OptiCell™ chamber, long-time ultrasound exposure may be required, as with increased exposure time, larger area will be affected. Nevertheless, the key principle we proposed here is applicable for all setups, which is the bubble dynamics play the key role in sonoporation study, as a bridge, connecting all ultrasound parameters and sonoporation outcomes.

3.5 Conclusion

In this study, microbubble dynamics in a large population exposed to 1s pulsed ultrasound have been thoroughly explored. After observing various bubble dynamics, three basic bubble dynamics categories have been identified. Bubble dynamics and corresponding delivery outcomes in three basic categories have been quantified and characterized. Category 3 “rapid collapse” can result in the optimal delivery outcomes. Finally we intended to build up the connection between ultrasound parameters and delivery outcomes bridging with bubble dynamics. These results provide insight in interpreting sonoporation outcomes in different experimental environments and ultrasound conditions. And more importantly, it built a knowledge base to guide optimization of bubble-cell interaction so that enhanced delivery outcomes can be achieved.

Chapter 4

Controlled and Enhanced Delivery Facilitated by Targeted Microbubbles

Interaction of ultrasound-driven microbubble with cells is the direct cause for intracellular delivery by sonoporation. In previous chapter we identified that the rapid collapse of microbubble, provides the highest uptake while maintaining good cell viability.

In this chapter, we describe our studies which utilized targeted microbubbles to further increase the controllability of microbubbles and their interaction with cells. By manipulating targeted microbubbles activities with optimized ultrasound exposure conditions, we achieved improved gene transfection outcomes.

4.1 Introduction

Targeting ligands attached to the lipid, protein or polymer shell coating of gas-filled microbubbles, can guide microbubbles specifically land on the cell surface where the targeted receptors are expressed [52, 72]. The rapid progress of targeted microbubble engineering in recent years is promoted by the general aims of spatial visualization of molecular markers of diseases, such as thrombosis, inflammation, ischemia/reperfusion injury, angiogenesis and related conditions [72, 190]. It can also function as specific and local drug and gene delivery carrier and booster both for *in vivo* and *in vitro* applications [12, 191, 192].

4.2 Materials and methods

4.2.1 Cell culture

Human Embryonic Kidney (HEK-293) cells were provided by Dr. Y. Eugene Chen (University of Michigan). Before experiments, the cells were grown in flasks in a humidified incubator at 37°C containing 5% CO₂ in DMEM supplemented with 10% fetal bovine serum and 1% penicillin-streptomycin. Human umbilical vein endothelial cells (HUVEC) were maintained in flasks in complete human endothelial growth medium (Lonza CC-3124, Walkersville, MD) in a humidified incubator at 37°C and 5% CO₂. For all experiments, cells were seeded in fibronectin coated 20 mm-diameter-glass-bottom 35 mm petri dish (MatTek, Ashland, MA, USA) one day before experiments. At the time of experiment, cells had reached approximately 90%-100% confluency.

Rat aortic smooth muscle cells (RASMC) were used for gene transfection. RASMC were maintained in flasks in complete growth medium consisting of DMEM/F12 (Gibco, Grand Island, NY) supplemented with 10% fetal bovine serum and 1% penicillin-streptomycin in a humidified incubator at 37°C and 5% CO₂. Before experiment, cells were plated in fibronectin coated 20 mm-diameter-glass-bottom 35 mm petri dish. Cells were cultured in the same medium for 18~24 hours. Cells were approximately 80% confluent by the time of gene transfection experiment.

4.2.2 Preparation of microbubbles

Targestar™-SA (Targeson, La Jolla, CA) are microbubbles composed of a perfluorocarbon gas core encapsulated by a lipid shell. The outer shell is derivatized with streptavidin, which can bind biotinylated ligands. The suspension in glass vial is at a concentration of approximately 1×10^9 microbubble/ml with a median diameter of 2.5 μm . Biotinylated anti-human CD51 antibody (Biolegend, City, State, USA) for targeting HEK cells; biotinylated anti-human CD31 antibody (eBioscience, San Diego, CA) for targeting

HUVEC cells; and biotinylated anti-mouse CD51 antibody (BioLegend, San Diego, CA) antibody for targeting RASMC were used respectively .

8 μl of targeted microbubbles stock solution (1×10^9 bubble/ml) was mixed with 2 μl of antibody (stock solution with concentration 0.5 mg/ml) and incubated for 20 min at room temperature then diluted into 490 μl DPBS (Invitrogen, Carlsbad, CA). The diluted solution has microbubble concentration of 1.6×10^7 microbubbles/ml, and antibody concentration of 2 $\mu\text{g/ml}$. Before binding antibody conjugated microbubbles to cell surface, culture medium in glass-bottom dish was completely removed first. 20 μl of diluted solution, which contained 3.2×10^5 microbubbles, and 0.04 μg of antibody, was added onto cells attached to the glass bottom of a petri dish. And then the petri dish was flipped over and incubated at room temperature for 10 minutes. Finally the dish was flipped back and gently washed with DPBS to remove unbound microbubbles.

4.2.3 Plasmid labeling and transfection

For ultrasound mediated gene transfection, pmaxFP™-Green-C plasmid (Lonza, Walkersville, MD), encoding green fluorescent protein (GFP), was added to extracellular medium (DPBS) at the final concentration of 10 $\mu\text{g/ml}$ before ultrasound exposure. 10 minutes after ultrasound exposure, the medium was discarded and replaced with fresh complete culture medium. The GFP expression was analyzed after 24 hours incubation.

To visualize the plasmid, plasmid was fluorescently labeled by nucleic acid stain fluorophore BOBO™-3 iodide (Invitrogen, Carlsbad, CA). BOBO™-3 iodide is non-fluorescent itself, after binding with double strands nucleic acid, it shows strong orange fluorescence, with the maximum excitation wavelength of 570 nm and maximum emission of 602 nm. To label plasmid, BOBO™-3 iodide was mixed with plasmid at the

molecule ratio of 1 dye molecule per 30 base pairs for 30 minutes in room temperature in dark.

Ultrasound mediated gene transfection was compared with lipofection, using lipofectamine 2000 (Invitrogen, Carlsbad, CA). Lipofectamine 2000 and plasmid were added to extracellular medium at the ratio of 1/1 (w/v). Cells were incubated in this medium for four hours and then the medium was discarded and replaced with fresh complete culture medium. The GFP expression was analyzed after 20 hours later.

4.2.4 Experimental setup and ultrasound application

The 35 mm petri dish was placed on the stage an inverted microscope (Nikon Eclipse Ti-U, Melville, NY). A 1.25 Mhz single element planar transducer (Advanced Devices, Wakefield, MA) was used for all experiments. The experiment setup was the same as described in Chapter 2, shown in Fig.2-1A, except that the OptiCell™ cell culture chamber was replaced by a 35mm petri dish. During the experiments, the transducer was mounted above the petri dish, angled at approximately 45° and its active surface submerged in extracellular medium in a petri dish 7.5 mm away from the cell surface. The transducer was driven by a function/waveform generator (Agilent Technologies 33250A, Palo Alto, CA) and a 75 W power amplifier (Amplifier Research 75A250, Souderton, PA). The transducer was characterized in free field using computer-controlled system with a 40 μm calibrated needle hydrophone (Precision Acoustics HPM04/1, UK). Different ultrasound conditions were employed, with peak negative pressure from 0.06 MPa to 2 MPa, PRF 10 or 20hz, DC from 0.008% to 20%, total exposure time from 8 μs to 1 s. For gene transfection, multiple pulse mode was used,

which consisting of 1-3 ultrasound pulses with increased pressure (1.6 MPa, 1.8 MPa and 2 MPa) with time interval 0.05 s.

4.2.5 Optical imaging

Microbubble activity in bright field driven by ultrasound was captured by a high-speed camera (Photron FASTCAM SA1, San Diego, CA) with frame rate 20,000 frames per second. Propidium iodide (PI) was used as an intracellular delivery marker, and fura2-AM was used to monitor intracellular free calcium ($[Ca^{2+}]_i$), which are the same as described in Chapter 2 and 3. After 2 excitation channels recording of fura2 fluorescent signals (at 340 nm and 380 nm), pseudo-colored ratio image of $[Ca^{2+}]_i$ were generated using MetaFluor Analyst (Molecular Devices, Downingtown, PA) and MATLAB (Mathworks, Natick, MA) following the same protocol described in Chapter 2. For fluorescent images, a monochromator (DeltaRAMX™ PTI, Birmingham, NJ) was employed to excite the samples at various wavelengths according to fluorophores. The fluorescent images were collected using a cooled CCD camera (Photometrics QuantEM, Tuscon, AZ) and then artificially-colored using Matlab or a color camera (QIMAGING Micropublisher 5.0, Surrey, BC, Canada).

4.2.6 Data analysis

Sonoporation delivery outcomes were assessed by viability (calcein AM assay), intracellular PI delivery efficiency and delivery amount (PI intensity). For each ultrasound application, the fluorescent images of PI were acquired before and after ultrasound exposure, and calcein image was acquired post ultrasound. The total number of cells with bubble attached in the FOV was considered as total cell number. The percentage of calcein positive cell in the total cell number was defined as viability.

Within total cells, the percentage of both PI and calcein positive cells (PI uptake and surviving cells) post ultrasound relative to all calcein positive cells (surviving cells) was defined as delivery efficiency. PI intensity was quantified in PI uptake and surviving cells using ImageJ software. The cell's contour was manually defined based on calcein image and applied to background corrected PI image. Spatially averaged red intensity was defined as PI intensity in this cell in arbitrary unit.

The ultrasound mediated gene transfection efficiency was examined 24 hours after ultrasound. The 6 dB band width of the 1.25 Mhz transducer with 10 cycles is 4 mm. Therefore, a 4 mm × 4 mm area was marked on the bottom of petri dish centered at the transducer aimed spot right after ultrasound exposure. After 24 hours, the percentage of GFP positive cells relative to the estimated total number of cells, which had bubbles attached before ultrasound, within this area was defined as transfection efficiency. The percentage of cells with bubble attached before ultrasound was calculated using the bright field image taken before ultrasound. This percentage was multiplied with the total cell number counted in this 4 mm×4 mm area 24 hours later. The result was used as the total number of cell, which had bubbles attached before ultrasound. In each 35 mm petri dish, 2 to 3 ultrasound exposures were applied. The lipofection efficiency was examined 24 hours since experiments started, including 4 hours incubation with lipofectamine2000 and plasmid, and 20 hours incubation with fresh growth medium. In each dish, 3 areas with 4mmx4mm were arbitrarily chosen to calculate the percentage of GFP positive cells relative to the total cell number in this area.

At each experimental condition, multiple experiments were conducted. The number of experiments are indicated where the results are reported.

4.3 Results

4.3.1 Controlled delivery by targeted microbubbles

Multiple entry areas were generated when multiple bubbles attached on one cells, and multiple excitations were created when multiple ultrasound pulses were applied. As shown in Fig.4-1A, two bubbles were positioned on the two ends of a cell, which resulted into two entry spots of PI (Fig.4-1B) and $[Ca^{2+}]_i$ (Fig.4-1C) transients simultaneously. The PI intensity at two spots was at the same level, which may be due to the similar size of the bubbles and similar intracellular RNA distribution at two spots. As long as the microbubble was not completely destroyed, it could respond to the following ultrasound excitation. The example shown in Fig.4-2 illustrates that PI uptake and $[Ca^{2+}]_i$ transient was created at time 0, when first ultrasound (0.17 MPa and 2.4 μ s) was applied; while PI uptake and $[Ca^{2+}]_i$ transient was created again at time 470 s, when a second ultrasound (0.23 MPa and 2.4 μ s) was applied. The insert of Fig.4-2A shows a bright field image before ultrasound and superimposed with PI image at time 11 s, indicating there was a microbubble attached on the left side of the cells, and PI entranced from the bubble attached area. The selective PI images and pseudocolor $[Ca^{2+}]_i$ images shown in Fig.4-2B presenting multiple PI uptake and multiple $[Ca^{2+}]_i$ changes.

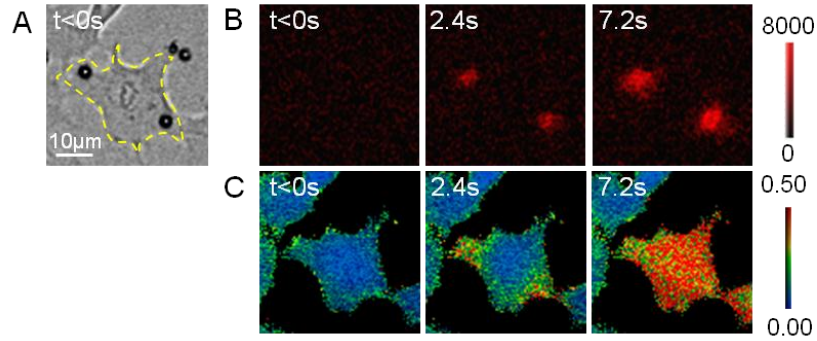


Figure 4-1 Multiple targeted microbubbles attached on cell membrane (A) resulted multiple entry area of PI (B) and Ca²⁺ (C). Ultrasound applied was of 0.17 MPa and 2.4 μs duration.

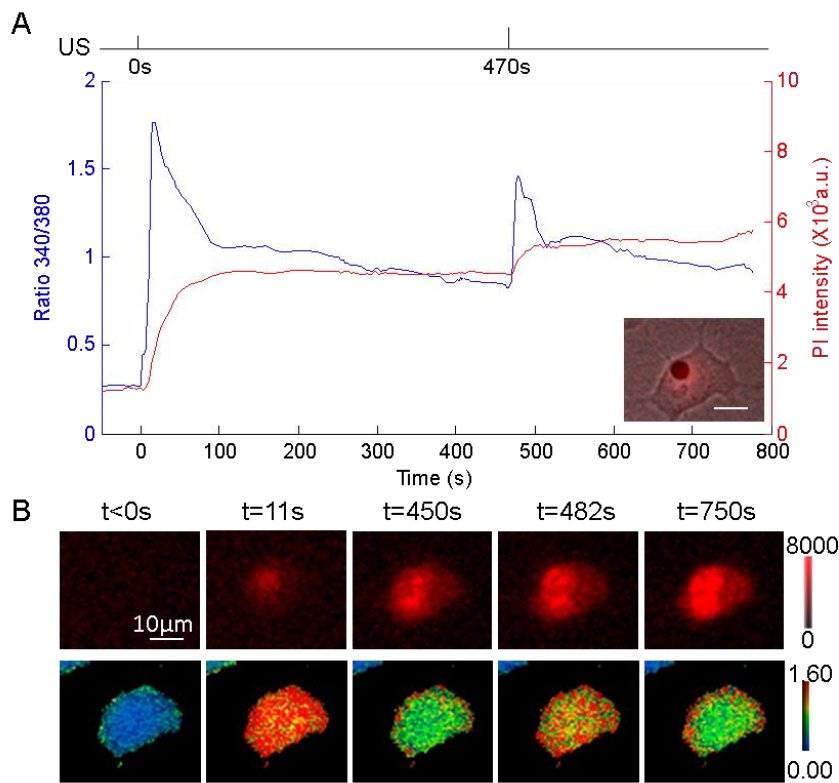


Figure 4-2 Multiple excitations of ultrasound pulses induced multiple entry of PI and Ca²⁺ at different time. (A) [Ca²⁺]_i change, indicated by ratio of 340 nm excitation and 380 nm excitation, and PI intensity change as a function of time. Insert is a bright field image before ultrasound superimposed with PI fluorescent image at time 11s. Scale bar is 10 μm. (B) Selective fluorescent images of PI (first row) and pseudocolor [Ca²⁺]_i images. The first ultrasound pulse was of 0.17 MPa and 2.4 μs duration, and second pulse was of 0.23 MPa and 2.4 μs duration.

Microbubbles with different initial size respond to the same ultrasound exposure differently. Because of the close distance between bubbles and cell membrane, the

difference of microbubbles response are very likely translated into the difference of cell membrane deformation and thereby delivery outcomes. On the other hand, selective excitation of microbubbles depending on their initial size can be used as a strategy to achieve staged delivery outcomes. Under the same ultrasound excitation (0.29 MPa and 5 μ s in Fig.4-3), typical images illustrates that bubbles with larger initial radius exhibited larger maximum radius during expansion (Fig.4-3A). From the measurement of 24 bubbles under this ultrasound condition, it shows that the maximum radius during expansion is linearly related with the initial radius ($R^2=0.87$) (Fig.4-3B). The results from Fig.4-3 imply that excited by the same ultrasound, bigger bubbles may results larger cell membrane deformation and therefore more uptakes compared with smaller bubbles. To more effectively stimulate small bubbles, stronger acoustic pulse may be needed. This principle was demonstrated in Fig.4-4. Upon the first ultrasound pulse (0.26 MPa and 8 μ s) at time 0, the bigger bubble (bubble 1, 2 μ m radius) was successfully excited and lead PI uptake into cell1 while the smaller bubble (bubble 2, 1.5 μ m radius) did not change much and resulted no PI uptake. A second pulse with higher pressure (0.6 MPa and 8 μ s) was applied at time 250 s and effectively excited bubble 2 and resulted in PI uptake into the cell. Staged delivery was achieved by selective excitation of microbubbles with different initial size.

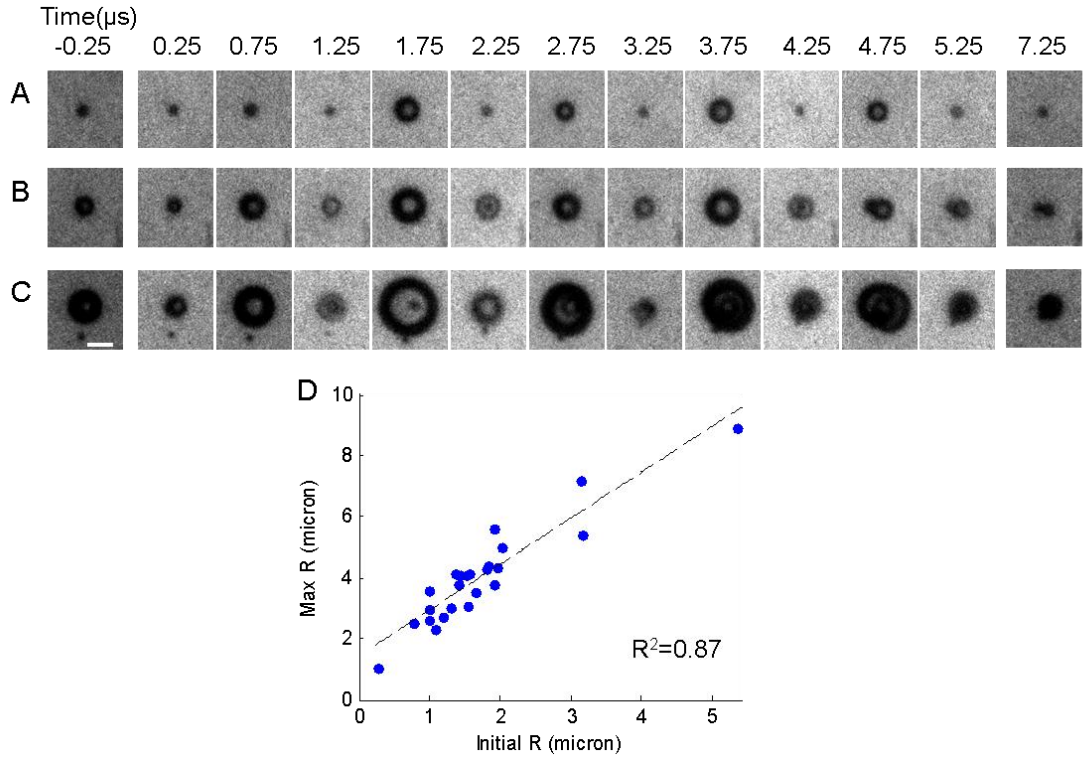


Figure 4-3 Maximum bubble radius during expansion is correlated with bubble initial size, under a certain ultrasound condition. (A-C) Ultra-fast images of Definity® microbubbles with different initial radius (1.9 μm, 3.1 μm and 5.3 μm) were excited by 0.29 MPa and 5 μs ultrasound. (D) Scatter plot of maximum bubble radius during expansion as a function of initial radius (n=24) excited by 0.29 MPa and 5 μs ultrasound. A linear fitting was applied, with the goodness of fitting $R^2=0.87$.

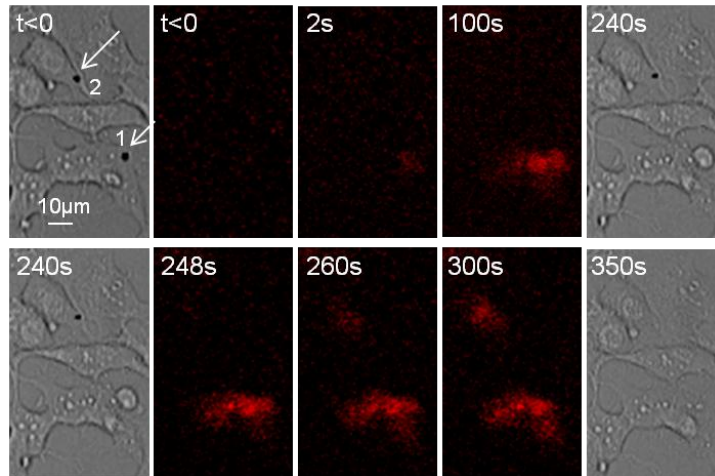


Figure 4-4 Excitation of microbubbles with different radius by different ultrasound pressure to achieve staged delivery. Before ultrasound, bubble 1 was of 2 μm radius and bubble 2 was of 1.5 μm radius. The first ultrasound (0.26 MPa and 8 μs) was applied at time 0 s, another ultrasound pulse (0.6 MPa and 8 μs) was applied at time 250 s.

4.3.2 Comparison of bubble dynamics between targeted and non-targeted microbubbles

The three basic categories of Definity® microbubble as non-targeted microbubbles were investigated in-depth in Chapter 3. Inheriting this concept from previous chapter, we applied the same ultrasound conditions corresponding to the three basic categories of non-targeted microbubble to targeted microbubbles to see the similarity and differences between non-targeted microbubbles and targeted microbubbles.

Figure 4-5 shows the targeted microbubbles response of ultrasound condition 0.06 MPa, 20 hz PRF, 20% DC and 1 s exposure. When a strong binding existed between targeted microbubble surface and cell membrane, although the attraction was still built up between adjacent bubbles during ultrasound-on period, once ultrasound was off, bubbles moved back by the binding force on cell membrane (Fig.4-5B). This movement took place repeatedly driven by pulsed ultrasound (Fig.4-5B). In the case there was no bubble nearby, the binding force held targeted microbubble firmly during ultrasound exposure. No movement or very mild movement was observed (Fig.4-5C). When the binding with cell surface was weak, it can be broken during ultrasound, releasing targeted microbubble from the cell membrane. In this case, unbound targeted microbubbles performed just as non-targeted microbubble (Fig.4-5D and E).The bubbles shown in Fig.4-5C and D led PI uptake (Fig.4-5A). Linking on cell surface localized activated-bubble impact on cells.

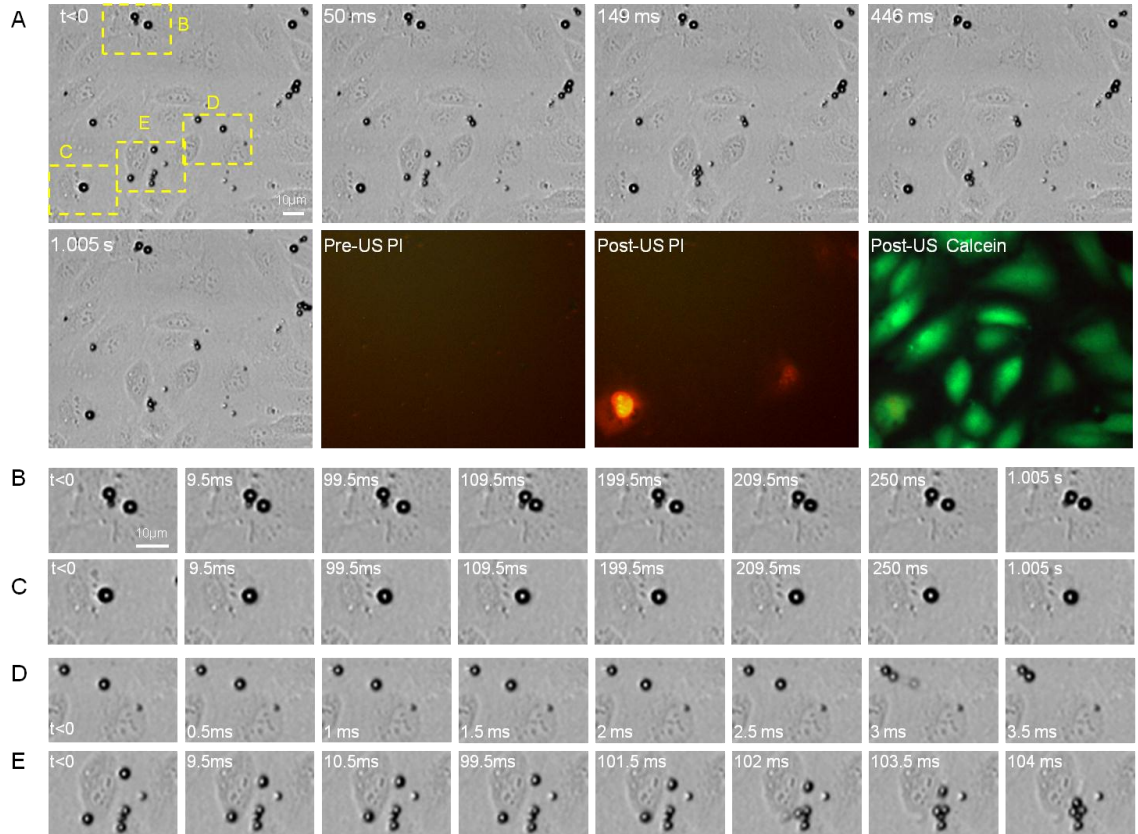


Figure 4-5 A typical example of Targestar™-SA microbubbles behavior category 1: aggregation and microstreaming. In this example, Targestar™-SA microbubbles were conjugated with anti-human CD31 antibody bound on HUVEC cells, excited by a 1.25 Mhz transducer, with 0.06 MPa, 20 hz PRF, 20% DC (10ms in each pulse), 1 s exposure totally. Panel (A) shows selective bright field images of a 216 μm \times 180 μm area before, during and immediately post ultrasound application, followed by fluorescence images excited at 538 nm before and post ultrasound for PI signals, and fluorescence images excited at 488 nm for calcein signal post ultrasound. Four sub-areas are selected in Panel (A), labeled as (B-D). (B) and (C) are microbubbles, which were bound the cell surface though entire ultrasound exposure; while (D) and (E) are microbubbles, whose link to cell surface were broken during ultrasound exposure. More temporal information was shown in panel (B-D) accordingly.

Driven by high acoustic pressure and long time (for the data shown in Fig.4-6, 0.43 MPa, 10 ms ultrasound was applied), the link of targeted microbubble was disassembled quickly; therefore there is no significant difference between non-targeted and targeted microbubbles. Similarly to non-targeted microbubbles (Fig.3-3), detached small microbubbles first coalesced into big bubbles, and further fused into bigger bubbles. Fast translational movement associated with violent oscillation occurred with

the coalesced big bubbles. The bright field images (Fig.4-6) clearly shows that the cells, which encountered the fast moving bubbles, were either torn apart, squashed, deformed or detached from the bottom (Fig.4-6).

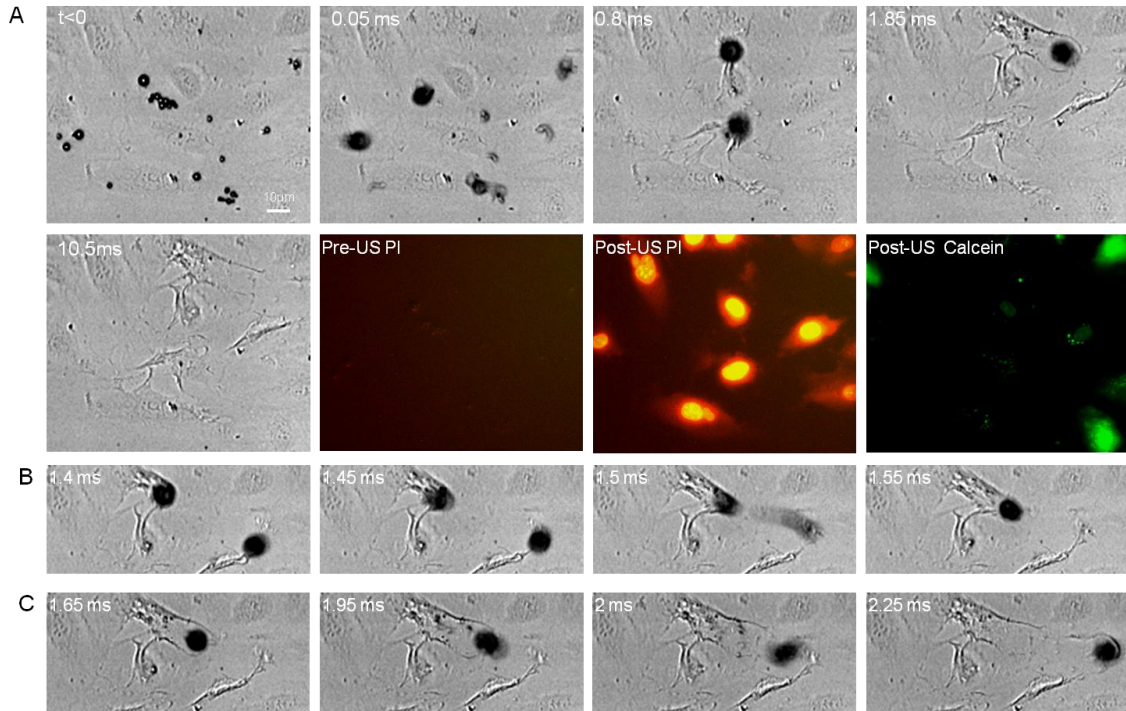


Figure 4-6 A typical example of Targestar™-SA microbubbles behavior category 2: coalescence and translation. In this example, Targestar™-SA microbubbles were conjugated with anti-human CD31 antibody bound on HUVEC cells, excited by a 1.25 Mhz transducer, with 0.43 MPa, 10 ms. (All bubble disappeared immediately after ultrasound.) Panel (A) shows selective bright field images of a 216 μm×180 μm area before, during and immediately post ultrasound application, followed by fluorescence images excited at 538 nm before and post ultrasound for PI signals, and fluorescence images excited at 488 nm for calcein signal post ultrasound. Panel (B) and (C) are sub-areas shown in the image of panel (A), with more temporal information, illustrating coalescence in (B) and newly fused big bubble fast translating while violently oscillating in (C).

For the third category, high pressure, short pulse was applied (0.43 MPa, 10hz PRF, 0.008% DC (8 μs), 1s for the data shown in Fig.4-7) to the targeted microbubbles. Immediate disappear and shrink was observed post each ultrasound pulse. The targeted microbubble may experience the similar dynamics during ultrasound-on time, as shown

in Fig.3-5 B-D. However, as these bubbles were positioned right on the cell surface, their collapse had more localized and maybe stronger impact on the cell membrane.

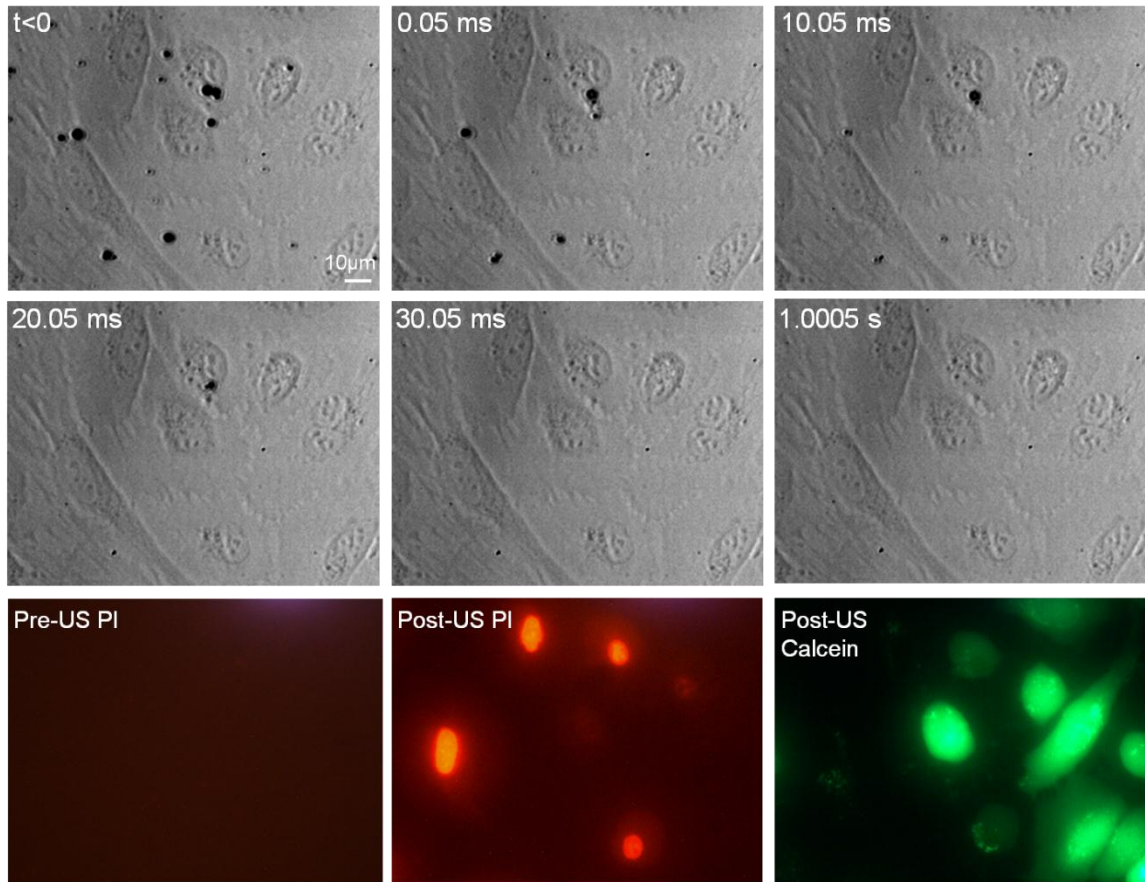


Figure 4-7 A typical example of Targestar™-SA microbubbles behavior category 3: collapse. In this example, Targestar™-SA microbubbles were conjugated with anti-human CD31 antibody bound on HUVEC cells, excited by a 1.25 Mhz transducer, with 0.43 MPa PNP, 10hz PRF, 0.008% duty cycle, 1s. Selective bright field images of a 293 µm×233 µm areas before, during and post 1s ultrasound are shown followed by fluorescence images excited at 538 nm before and post ultrasound for PI signals, and fluorescence images excited at 488 nm for calcein signal post ultrasound.

4.3.3 Delivery outcomes by sonoporation using targeted and non targeted microbubbles

Under the same ultrasound parameters, quantified PI delivery outcomes were presented together in Fig.4-8 of non-targeted microbubbles in Opticell setting as

presented in Chapter 3 and targeted microbubbles in petri dish setting. For all three categories, PI delivery outcomes shared the same trends with non-targeted microbubbles in Opticell and targeted microbubbles in petri dish: “rapid collapse” provided the highest delivery efficiency among three categories; although targeted microbubbles in petri dish always had stronger effects than non-targeted microbubble in Opticell, killing more cells. Therefore “collapse” bubble dynamics mode was chosen for the following study.

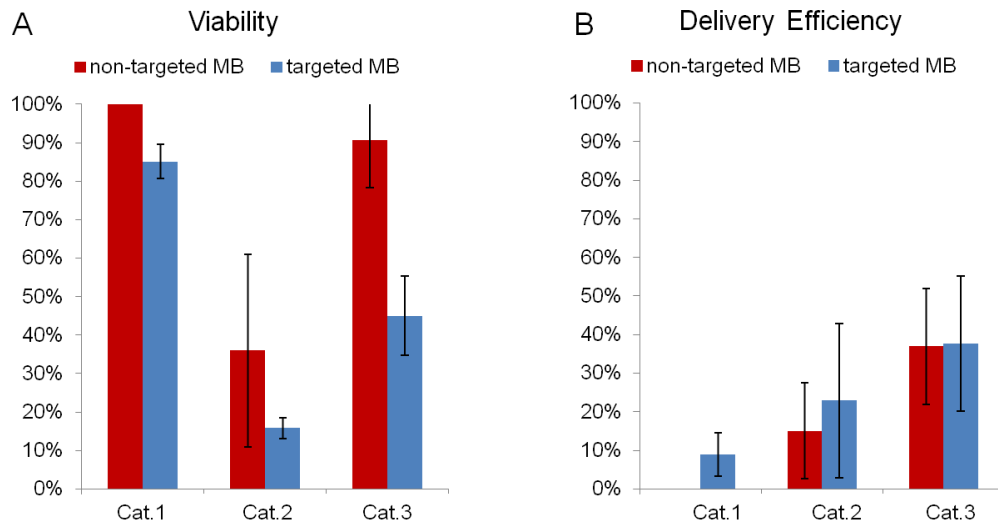


Figure 4-8 PI delivery outcomes of Definity® microbubbles (non-targeted microbubbles) in Opticell setting and Targestar™-SA microbubbles (targeted microbubbles) in petri dish setting in three typical categories: Cat.1: aggregation and microstreaming; Cat.2: coalescence and translation; and Cat.3: collapse. Ultrasound conditions used for data shown here for Definity® microbubbles are: Cat.1: 0.06 MPa, 20 hz PRF, 20% DC (10ms in each pulse), 1 s (N=9); Cat.2: 0.43 MPa, 20 hz PRF, 20% DC, 1 s (N=10); and Cat.3: 0.43 MPa, 10 hz PRF, 0.008% duty cycle, 1 s (N=13). Ultrasound conditions used for data shown here for Targestar™-SA microbubbles were the same as Definity® microbubbles: Cat 1 (N=6); Cat 2 (N=6); and Cat 3 (N=4).

4.3.4 Optimization of PI delivery

The ultrasound parameters creating the third category were 0.43MPa, 10hz PRF, 0.008% DC (8μs), 1s, which was chosen arbitrarily. Starting from this ultrasound condition, we conducted systematic study to optimize delivery outcome using PI as the delivery indicator. This ultrasound condition led to 55%±10.3% cell death. If reduced the

pulse number applied, we may be able to increase the cell viability as well as delivery efficiency. As shown in Fig.4-9, as the pulsed number decreased from 10 pulses to 2 pulses and further 1 pulse, the viability significantly increased as well as the delivery efficiency.

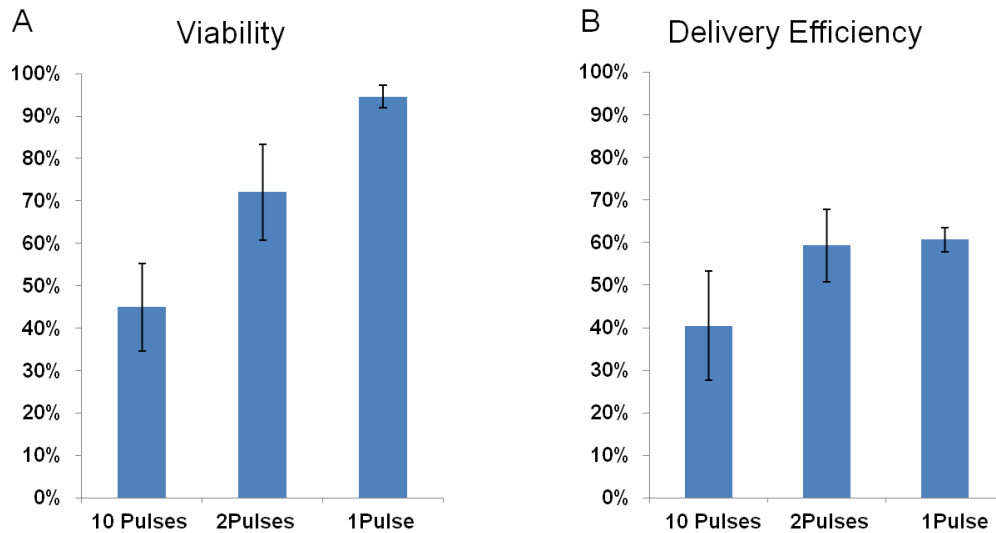


Figure 4-9 Viability (A) and delivery efficiency (B) using PI as the delivery indicator with different ultrasound pulses. For all data, the acoustic pressure was 0.43MPa, 10hz PRF (for multiple pulses) and 8 μ s for each pulse. N \geq 5 for each condition.

With 0.43MPa, one pulse generated better results than 2 pulses and 10 pulses; therefore one pulse ultrasound was applied for the following optimization. We applied different acoustic pressure with single ultrasound pulse to test whether with higher acoustic pressure, higher delivery efficiency and larger amount of PI can be resulted. PI intensity inside the cells were quantified and used as an indicator of PI amount delivered into the cells. The impacts of acoustic pressure on delivery outcome were shown in Fig.4-10.

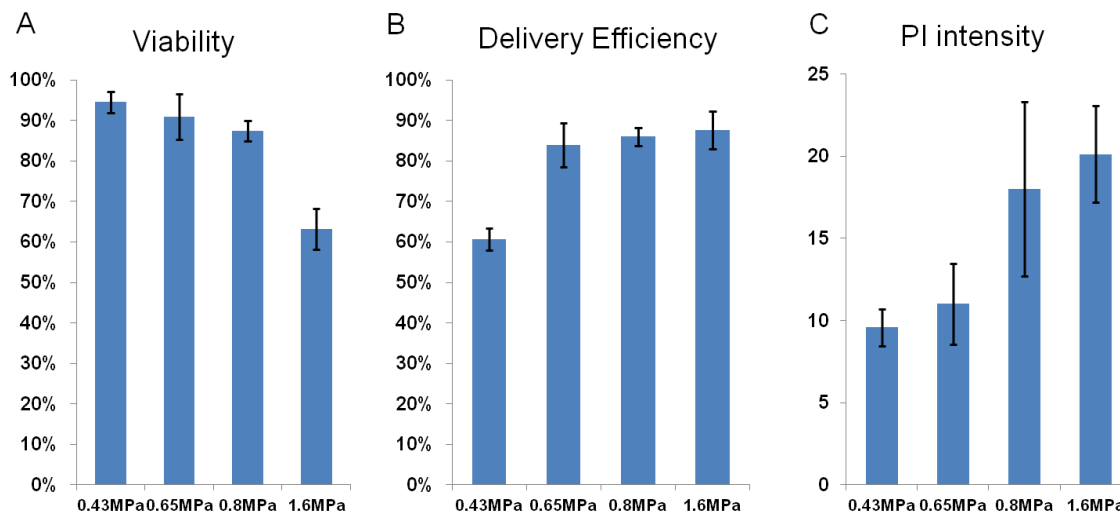


Figure 4-10 Viability (A), delivery efficiency (B) and PI intensity (C) with different acoustic pressure. For all data, single ultrasound pulse with $8\mu\text{s}$ duration was applied. $N \geq 5$ for each condition.

Considering the plasmid used for gene transfection was much larger than small molecule PI, larger pore may be required. The acoustic pressure 1.6MPa, which led the highest PI intensity in these experiments: 20.1 ± 2.9 ($N=7$) in arbitrary units at the cost of $37\% \pm 5\%$ cell death, was chosen for gene transfection experiments.

When the situation that microbubbles attached on cell surface was created, another parameter that could take effect on delivery outcomes is the number of bubbles attached in each cell. It is found that when 2 or 3 bubbles attached per cell can induce higher delivery efficiency compared with 1 bubble attached case (Fig.4-11). As demonstrated in Fig.4-1, 2 bubble attachments can create 2 entry spots of PI, increasing the chance of extracellular agent uptake, which may explain why 2 or 3 bubble attachment had higher delivery efficiency than 1 bubble attachment. Although it's hard to create a uniform bubble distribution on cells in entire FOV, by increasing targeted

microbubble density, a 2 or 3 bubbles per cell dominated situation can be generated. Therefore, for the following study, this bubble-cell ratio was adopted.

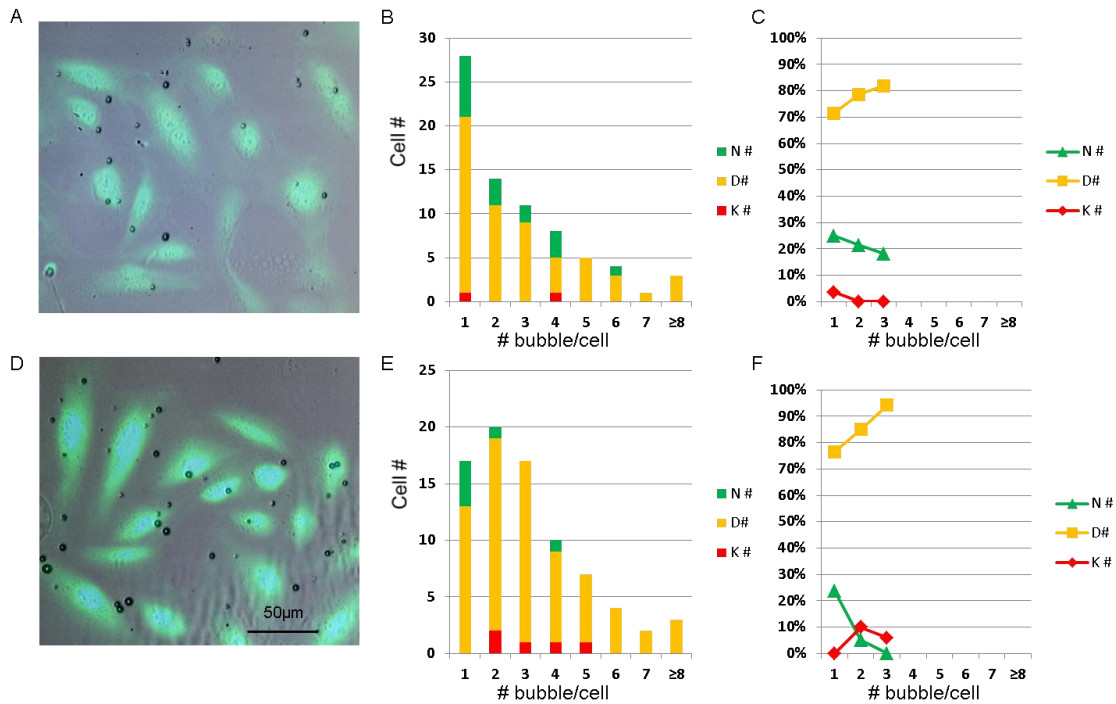


Figure 4-11 Impact of the number of bubbles attached per cells (# bubble/cell) on delivery outcomes. (A-C) are typical example of # bubble/cell distribution 1 and (D-E) are typical example of distribution 2. (A) and (D) are calcein image superimposed bright field image before ultrasound. (B) and (E) are cell number grouped by # bubble/cell corresponding to the example shown in (A) and (D) in the entire FOV. Green, yellow and red represent surviving and no PI uptake cells, surviving and PI delivered cells and killed cells respectively. (C) and (F) convert the information shown in (B) and (E) into percentage within three groups (1bubble/cell, 2bubble/cell and 3bubble/cell).

4.3.5 Enhanced gene transfection achieved by targeted microbubble and optimized ultrasound exposure condition

For gene transfection, rat aortic smooth muscle cells (RASMC) were chosen, as it serves as an *in vitro* model to study sonoporation potential to treat cardiovascular disease. The presence of GFP 24 hours later is an indicator of successful gene transfection. To visualize plasmid, plasmid was fluorescently labeled using BOBO™-3 iodide. The

fluorescent image, which was taken right after ultrasound, shows that the plasmid was already homogeneously distributed in cytoplasm and nucleus (Fig.4-12A). Plasmid positive cells all had bubble attached before ultrasound (Fig.4-12C and D), indicating the rapid and direct transfer of plasmid by sonoporation probably via the physical pore in cell membrane.

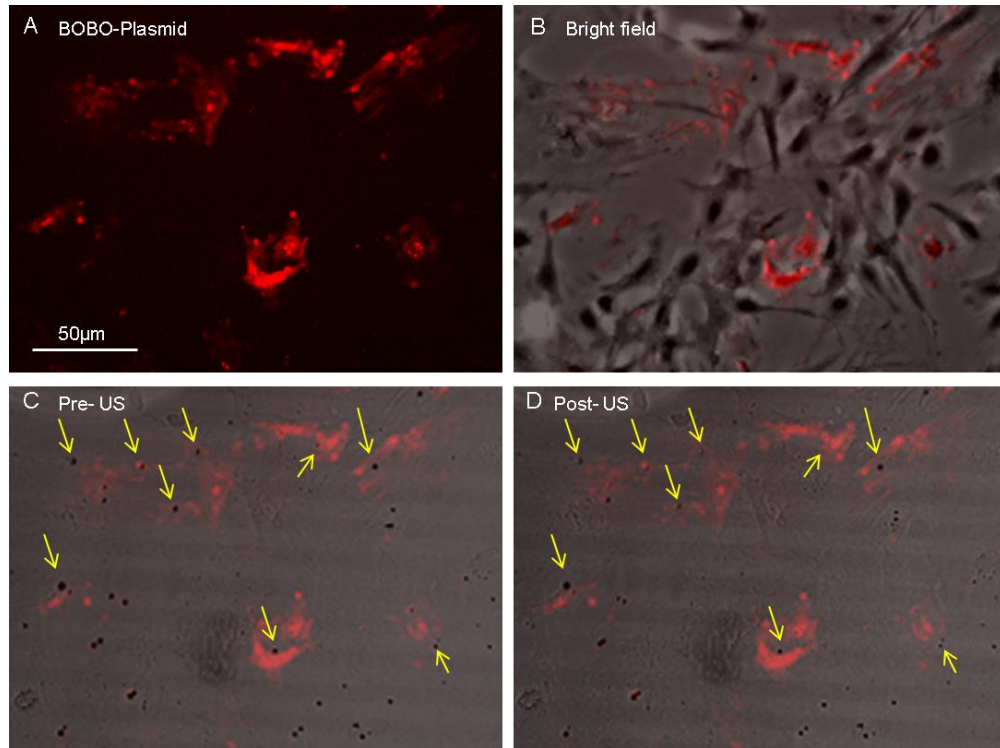


Figure 4-12 BOBO™-iodide labeled plasmid delivery was spatially correlated with bubble attached cells. (A) Fluorescent image excited at 570 nm post ultrasound. (B) Phase contrast bright field image post ultrasound. (C-D) are (A) superimposed with bright field image before and post ultrasound. Arrows point the bubbles, which resulted plasmid uptake.

Based on the PI delivery study presented above, single ultrasound pulse consisting of 10 cycles (8µs duration) with 1.6 MPa was used to mediate gene transfection first. However, this parameter only resulted into $1.8 \pm 0.5\%$ (N=9) transfection efficiency (Fig.4-15 G), which may be due to limited amount of plasmid delivered and some inherent obstacles on the gene expression pathway in RASMC. Fast speed bubble

dynamics recording revealed that after the 1st ultrasound pulse, remaining bubbles did not disappeared right away (Fig.4-15D), which makes it possible to active bubble multiple times to generate multiple entry of plasmid. Therefore, 2 and 3 pulses with time interval 0.05 s were employed. The lipid shell cracked or broke during the 1st pulse; when the 2nd ultrasound pulse was arrived; residual bubbles were of smaller size, as shown in Fig.4-13D and F. To more effectively activate smaller residual bubbles, a scheme with ramped up acoustic pressure were employed, as illustrated in Fig.4-13G. The 2nd pulse was with acoustic pressure 1.8 MPa, and the 3rd pulse with 2.0 MPa. Two pulses ultrasound significantly increased the transfection efficiency compared with single pulse, leading a transfection efficiency $6.6 \pm 2.2\%$ (N=9). While as three pulses may be too strong to cells, resulting severe cell death and unhealthy condition for the surviving cells, which may explain why the transfection efficiency dropped to $2.5 \pm 0.8\%$ (N=4) with three pulses. Figure 4-14 presents a typical image of GFP expression using two pulses with ramped up pressure ultrasound scheme.

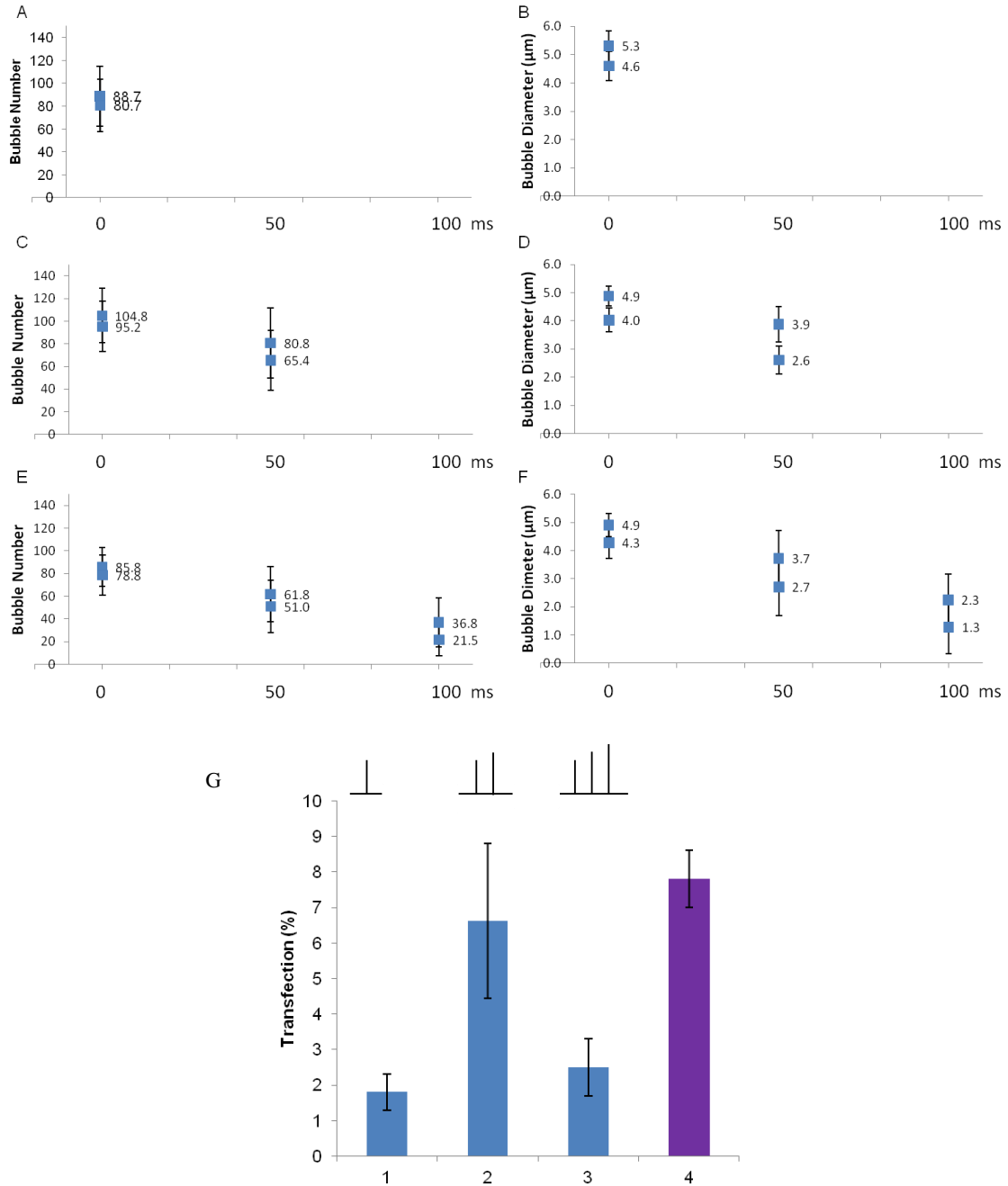


Figure 4-13 Characterization of bubble number and bubble size change in three ultrasound conditions: 1.6 MPa, 8 μ s (A and B); 1.6 MPa, 8 μ s followed by 1.8 MPa, 8 μ s with 50 ms time interval (C and D); and 1.6 MPa, 8 μ s, followed by 1.8 MPa, 8 μ s, and 2.0 MPa, 8 μ s with 50 ms time interval (E and F). (G) Gene transfection efficiency corresponding to the three conditions, and from lipofection (purple filled bar).

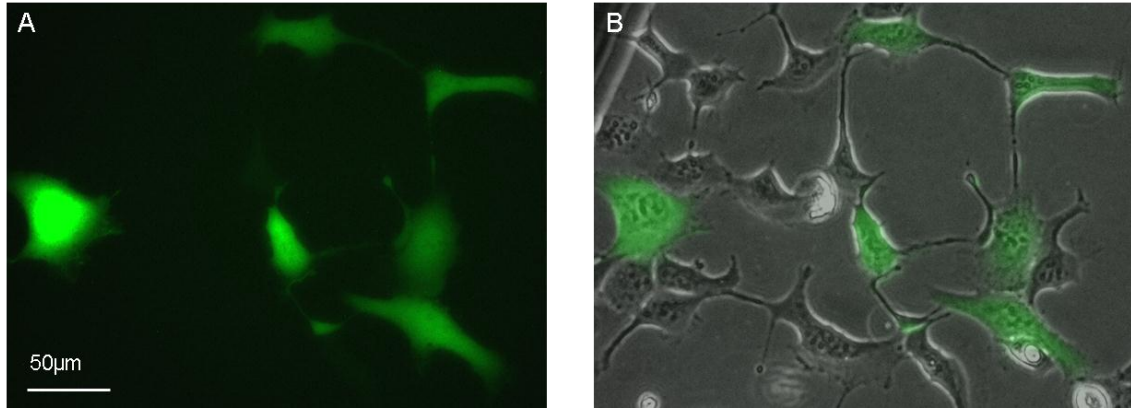


Figure 4-14 Example images show GFP expressed cells (A) and superimposed with bright field phase contrast image (B) using ultrasound condition: 1.6 MPa, 8 μ s followed by 1.8 MPa, 8 μ s with 50 ms time interval.

4.4 Discussion

4.4.1 Controlled ultrasound excitation of targeted microbubbles

By incorporating ligands in the microbubble coating materials, microbubbles can achieve localized adhesion at the site where a specific molecular marker is expressed, which is the underlying mechanism for ultrasound molecular imaging and therapy. The close distance between microbubble and cell surface significantly increase the vulnerability of cell membrane to microbubble action upon ultrasound excitation. Thanks to the superior controllability provided by targeted microbubbles, we demonstrated that multiple entry areas and multiple excitations, as well as selectively excitation of targeted microbubbles. The response of a microbubble to ultrasound excitation (cavitation), such as expansion, contraction and collapse, depends on the size of the bubble and the acoustic parameters including the acoustic pressure, center frequency, and pulse duration [12, 100]. For preformed microbubbles with a thin encapsulating shell, the ultrasound driven expansion and contraction of the bubble often destroy the protecting shell [193], resulting in more robust volume oscillation and/or collapse of the free gas bubble. The oscillation

and collapse of the bubble are in the time scale below sub- μ s for ultrasound excitation in the MHz frequency. Ultra-fast video-microscopy [12, 13] (millions frames/s) has illustrated some details of cavitation including the formation of membrane-directing fluid jet during violent bubble collapse near a cell membrane. In this study, we presented ultra-fast images of Definity® microbubble oscillation in OptiCell™ with different initial bubbles size to demonstrate the concept that at the same acoustic pressure, larger microbubbles exhibits larger expansion during ultrasound rarefaction. All the microbubbles were linked on the cell surface, and the distances were reported much less than 100 nm [182], which is almost negligible compared with micron scale microbubbles and its even bigger expansion size, thereby larger expansion will result larger deformation of the cell membrane, leading more agent uptake. As the fundamental causes for any sonoporation outcomes, microbubble interaction with cells under ultrasound exposure is the key to gauge the effect of ultrasound application.

4.4.2 Binding force between targeted microbubbles and cell membrane

Both for the application of molecular imaging and targeted drug delivery, it is essential of targeted microbubbles to form stable and firm bonds with cell surface. In this study, we observed that under ultrasound condition of 0.06 MPa, 20 hz PRF, 20% DC, 1 s, some microbubbles exhibited very firm bonds on cell surface, that they moved a couple of micron away from their initial position during ultrasound-on time, and restored back during ultrasound-off time, and it occurred repeatedly (Fig.4-5B); while some microbubbles were released from broken bonds (Fig.4-5D and E), which indicates the strength of the binding varies from bubble to bubble.

The AFM result suggested that the single bond formed between CD31 antibody, which was decorated in microbubble via biotin-avidin link, and CD31 expressed on Sk-Hep1 hepatic endothelial cells had a median of 93 pN adhesion force [194]. The total binding force between a single microbubble and cell membrane also depends on ligand density of microbubble surface, receptor availability of cell membrane and the contact area, which may vary dramatically from case to case. That's why we see different situations of disassociation between microbubbles and cell membrane under the same ultrasound influence. Our observation also demonstrated that both the first and secondary radiation force (Fig.4-5D) can be used as an energy modality to detach microbubbles from cell surface. Secondary radiation force has been employed to estimate the force between single bond to be hundreds of pN [182].

4.4.3 Restoring and detachment mechanisms

In this study, we observed both restoring after microns displacement and detachment of targeted microbubbles when driven by mild ultrasound (Fig.4-5B-E). The mechanisms for the restoring force is suggested to be deformation of microbubbles or lipid bilayers of cell membrane [182, 194], or excess interfacial materials to form tethers and folds extending outward [72, 195] , and it is less likely to the springs behavior of ligand and receptor [196], as this distance was at sub-nanometer scale and therefore cannot account for the micron scale displacement observed in this study. When the pulling force exceeds the strength of the total binding force between microbubbles and cell surface, detachment will happen. Most likely the break occurred first between ligand and receptor [194] and less likely occurred first between avidin and biotin, as it's reported to have a larger binding force around 257 pN [197].

4.4.4 Loading capability of antibody on microbubbles

Currently, the relative low antibody density carried in microbubble is one limiting factor in forming strong bonds. It is reported that CD31 molecules expressed in endothelial cell was at the level of 10^6 molecule/cell [198]. Based on the images show in this study, the cell surface area is around $2 \times 100 \mu\text{m}^2$; therefore, the receptor density is 5×10^3 molecule/ μm^2 . The contact area was estimated to be $1 \mu\text{m}^2$ [88]. With current technique, antibody linked on microbubbles was approximately 100-200 molecule/ μm^2 [88, 182]. As a result, in the contact area, receptors are in one order more than antibody and exceed even more in the case where receptors are over expressed under pathological condition. Therefore, great efforts have been made to enhance the load capability of antibody on microbubbles. With more sophisticated strategies, therapeutic reagents can also be coupled on microbubbles, which will further enhance the targeted delivery efficiency [3, 12, 67, 72, 190, 199]

4.4.5 The impact of primary radiation force and ratio of bubble/cell on delivery

outcomes

Figure 4-11 presents the PI delivery outcomes using the same ultrasound parameters with non-targeted microbubble (Definity® in Opticell setting) and targeted microbubbles (Target-start SA in petri dish setting). The data shows that with targeted microbubbles, it always generated stronger impacts on cell, meaning killing more cells than with non-targeted microbubbles. The close distance between targeted bubble and cell surface may contribute to the stronger impact. However, given the configuration of cells and bubbles were different in two settings, other factors, such as primary radiation

force and ratio of bubble/cell may also be responsible for the delivery outcomes difference and should be taken into consideration.

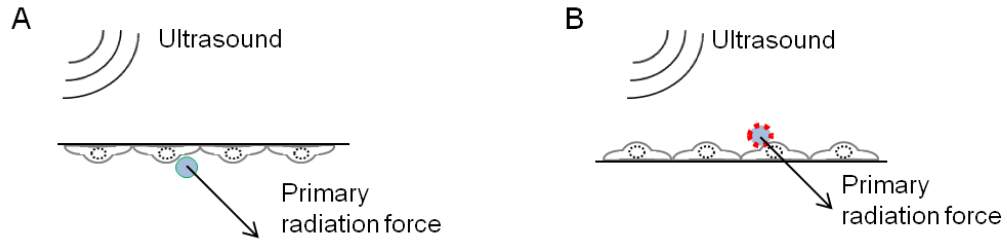


Figure 4-15 Schematic illustration of the direction of primary radiation force in Opticell setting with Definity® microbubbl (A) and in petri dish setting with Targestar™-SA targeted microbubble (B).

As shown in Fig.4-15, in Opticell, when ultrasound was applied, the primary radiation force was pushing microbubble away from cell surface, while in petri dish setting, when ultrasound was applied; the primary radiation force was towards cells. This may be partially responsible for the stronger impact resulted in petri dish setting. We estimated primary radiation force under ultrasound condition creating basic category one and compared it with buoyancy. Once the Definity microbubble was pushed away from cell monolayer during ultrasound on, it was subject to buoyancy and primary radiation force only (Fig.4-16).

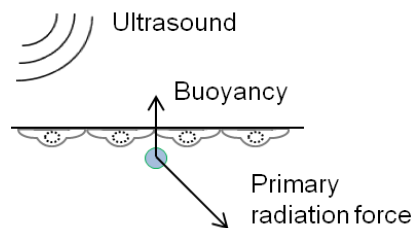


Figure 4-16 Force diagram of Definity® microbubble once it was pushed away from cell monolayer.

Under the assumption of small-amplitude linear oscillation, and the time averaged primary radiation force exerted on microbubbles were estimated using the following equation [112]

$$F_{rad} = \frac{2\pi P_A^2 DR}{\rho_0 c \omega T} \frac{2\beta_{tot}/\omega}{\{[(\omega_0/\omega)^2 - 1]^2 + (2\beta_{tot}/\omega)^2\}} \quad \text{Equ. 4-1}$$

where P_A is incident acoustic pressure amplitude, D is duration of each transmitted pulse, T is pulse repetition period, R is bubble radius at equilibrium, ρ_0 is density of surrounding medium, ω is frequency (radians/second), ω_0 is resonant frequency of the bubble, β_{tot} is dimensionless damping coefficient related to δ_{tot} by $\delta_{tot} = 2\beta_{tot}/\omega_0$, δ_{tot} is total damping constant, includes dissipation due to radiation, viscoelastic and thermal losses.

To calculate the resonant frequency of Definity® microbubble with equilibrium radius R , Equation 4-2 was used, cited from Goertz etc [200]

$$f_0 = \frac{1}{2\pi} \sqrt{\frac{3\gamma p_0}{\rho_0 R^2} + \frac{2S_p}{\rho_0 R^3}} \quad \text{Equ. 4-2}$$

Where γ is the polytropic exponent, R is the bubble radius at equilibrium, ρ_0 is density of surrounding medium, p_0 is the ambient pressure (100 kPa), and S_p is the stiffness of shell.

The total damping constant (δ_{tot}) is the sum of the radiation (δ_{rad}), viscous (δ_{vis}), and shell friction (δ_{sh}) terms. To calculate the δ_{tot} , the following four equations were used [200]:

$$\delta_{tot} = \delta_{rad} + \delta_{vis} + \delta_{sh} \quad \text{Equ. 4-3}$$

$$\delta_{rad} = \frac{\omega R}{c} \quad \text{Equ. 4-4}$$

$$\delta_{vis} = \frac{4\mu_l}{\omega \rho_0 R^2} \quad \text{Equ. 4-5}$$

$$\delta_s = \frac{S_f}{4\pi \rho_0 R^3 \omega} \quad \text{Equ. 4-6}$$

Where μ_l is the liquid viscosity and S_f is the viscosity of the shell.

In this study, we used Definity® microbubbles and the surrounding medium can be considered as water. The ultrasound condition for category 1 (0.06MPa, 20hz PRF, 20% duty cycle, 1s) satisfied the assumption of small-amplitude linear oscillation. Therefore Equ.4-1 to 6 was used to estimate the force exerted on a Definity® microbubble (Fig.4-17). The primary radiation force has a peak with 4.25µm radius Definity® microbubble (Fig.4-17B), as the incident ultrasound has the center frequency of 1.25Mhz, which is the resonance frequency of a 4.25µm radius Definity microbubble (Fig.4-17A). The primary radiation force is significantly larger than Buoyancy (Fig.4-17B-C). For example, a Definity® microbubble with radius 2.5µm, primary radiation force exerted on it is 1.85×10^{-11} N while buoyancy on it is 6.41×10^{-13} N, 2 orders higher. Therefore, primary radiation force is an important factor that contributes to stronger impact of the same ultrasound conditions in petri dish setting compared with Opticell setting.

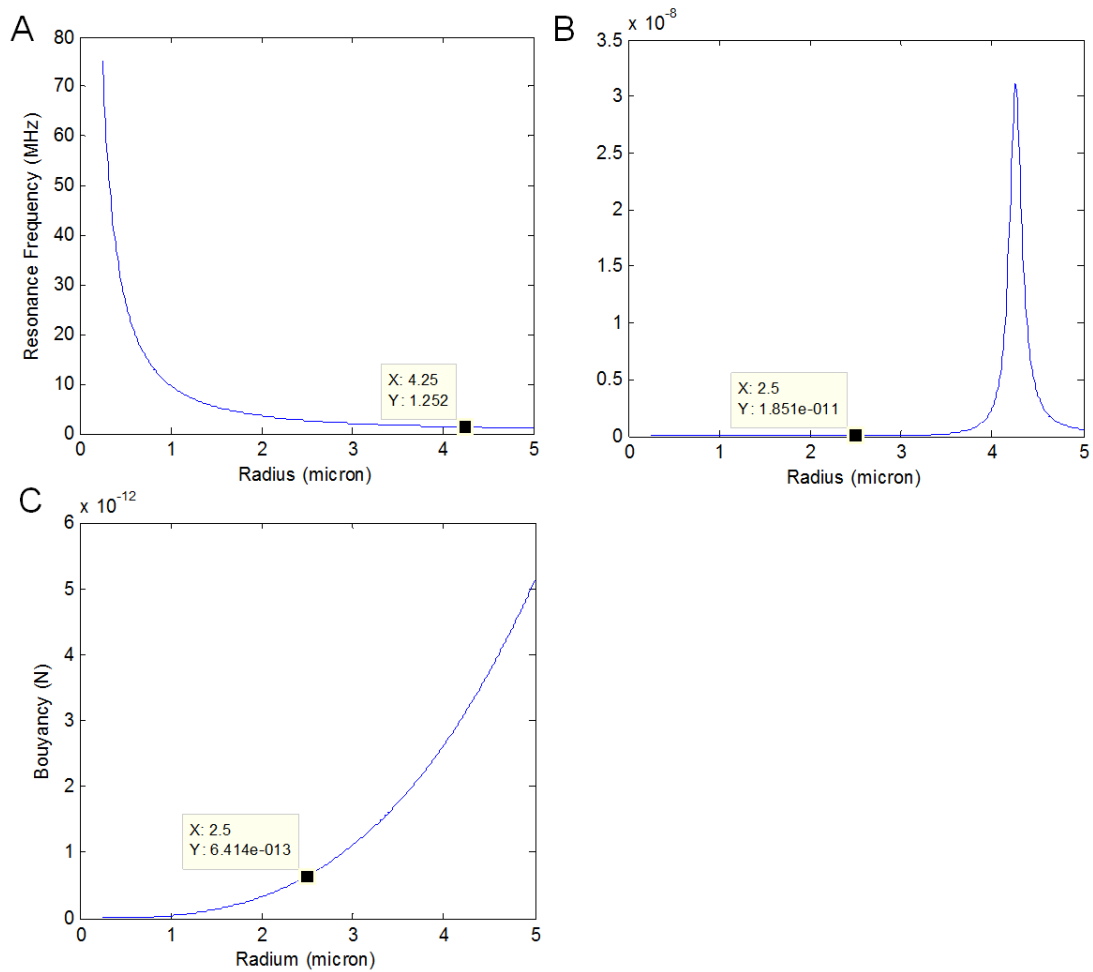


Figure 4-17 Simulation of resonance frequency of Definity® microbubbles (A), time-averaged primary radiation force on a Definity® microbubble with 0.06MPa peak negative pressure and 20% DC (B) and buoyancy of Definity® microbubbles in water.

Another factor that may affect the delivery outcomes due the configuration difference in Opticell and petri dish is the ratio of bubble per cell. Under the ultrasound condition: 0.43MPa, 10hz PRF, 0.008%DC (8 μ s), 1s, which generated the third basic bubble dynamics category, the ratio of bubble per cell in Opticell with Definity® was 6.2 \pm 0.9 bubbles/cell (N=9); and in petri dish with targeted microbubble, it was 2.2 \pm 0.4 bubble/cell (N=4). In Opticell, the ratio was calculated by dividing the total bubbles number in FOV by the total cells number in FOV. In petri dish with targeted

microbubbles, a histogram of bubble/cell was generated first, as it was clear how many bubbles attached to individual cells. Then an average was calculated to present the mean ratio of bubble/cell in this data.

Cells subjected to more bubbles in Opticell did not lead to a stronger delivery outcomes than in petri dish with targeted microbubbles. This may be explained as bubbles were under stronger influence of secondary radiation force with higher density; or in Opticell bubbles preferably located in the cell edge area, as edge is vertically higher than the nucleus area. In addition, the difference in the construction and chemical composition of Definity® microbubbles and Targestar™-SA microbubbles may also contribute to their different responses to ultrasound and therefore the difference in delivery outcomes.

In short, based on the study with Definity® microbubble in Opticell and Targestar™-SA microbubble in petri dish, no conclusions can be made about whether non-targeted microbubbles or targeted microbubble have stronger impact on cells under the same ultrasound conditions, as many differences involved in these two sets of experiences, such as the direction of primary radiation force, the ratio of bubble/cells, the difference between two bubble types, etc.

4.5 Conclusion

Ligand-conjugated microbubbles showed favorable for controlled intracellular delivery. Based on in-depth understanding of ultrasound-driven microbubbles dynamics in sonoporation process, we achieved enhanced gene transfection efficiency, 6.6% to RASMC compared to the 1% efficiency to RASMC reported in literature using

sonoporation[67]. This well controlled platform has a promising perspective to extend its applications into boarder biological and biophysical research context.

Chapter 5

Future Work

In this thesis work, we studied the transmembrane delivery and calcium transients generated by sonoporation (Chapter 2), investigated the critical role that ultrasound-driven microbubbles play in sonoporation and the resulting intracellular delivery, and achieved improved gene transfection using targeted microbubbles and optimized ultrasound exposure conditions (Chapter 3 and 4). The results obtained from this study provide new insights into the cellular and biophysical aspects of sonoporation, which can be helpful in the effort to develop sonoporation as a reliable and robust technique for intracellular delivery applications.

Introducing ion exchange while delivering extracellular agent is a special feature in sonoporation compared with other delivery methods, such as lipofection, as demonstrated in Chapter 2. Intracellular ion concentration change is very important, especially to excitable cells, such as cardiomyocyte and neurons. For the future, we propose to create controlled ion influx by sonoporation to manipulate the transmembrane potential in excitable cells. We achieved 92% delivery efficiency of PI and 6.6% gene transfection to RASMC using targeted microbubbles under optimized ultrasound conditions based on comprehensive understanding of bubble dynamics in Chapter 3 and 4. However, the gene transfection efficiency is still far from being ideal. Successful delivery of plasmid into cell is the first step leading to gene transfection. The limiting factors may exist in the following intracellular migration and expression pathways of

delivered plasmid. Therefore, to further understand and improve gene transfection efficiency, for the future work, we propose to study the internalization and expression pathways of exogenous plasmid after sonoporation.

5.1 Specific topics for future investigations

5.1.1 Manipulation of the contraction rhythm of cardiomyocyte via controlled Ca^{2+} influx by sonoporation

In this study, we demonstrated the Ca^{2+} influx was generated after cell membrane sonoporated. Ca^{2+} plays an important role not only in cell communication, but also in regulating cell membrane voltage [201-203]. Therefore, another potential consequence of Ca^{2+} influx along with other ion influx through the pore can be membrane voltage change, which can be used to manipulate excitable cells, such as cardiomyocyte and neuron. Automatic rhythmic contraction is the unique property of cardiomyocytes, and Ca^{2+} play an important role in contraction regulating [204-206]. By attaching targeted microbubble on cardiomyocyte surface, and stimulating it periodically, potentially we could induce Ca^{2+} ion into cardiomyocyte periodically, therefore manipulate the membrane voltage and change its contraction rhythm. Premature cardiac contraction (arrhythmias) has been reported in laboratory animals and human during contract agent enhanced echocardiography [137, 174, 175]. The study proposed here could uncover the mechanisms for observed premature contraction and also potentially lead the development of a sonoporation based arrhythmias treatment strategy. Figure 5-1 presents the preliminary results demonstrating the feasibility of changing the contraction rhythm of cardiomyocyte.

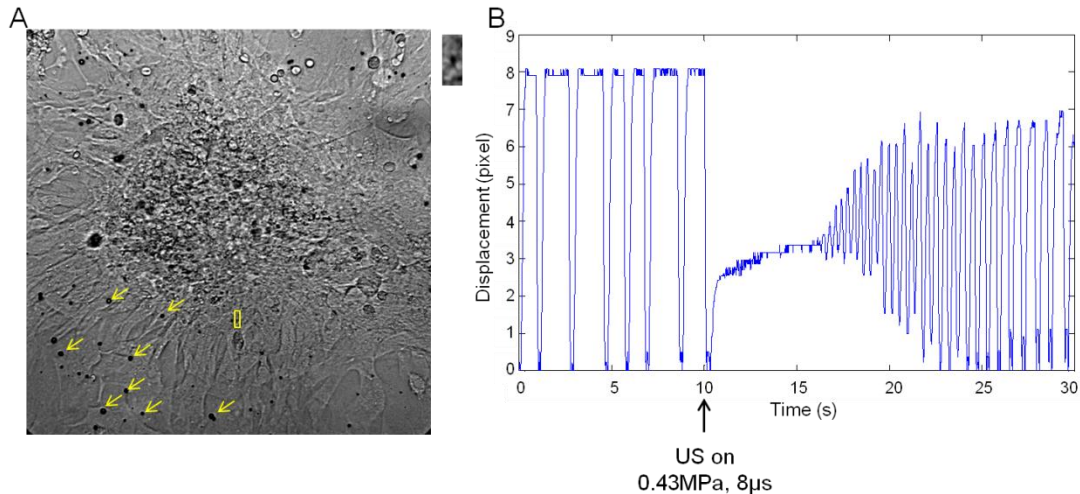


Figure 5-1 A example demonstrates that contraction rhythm of cardiomyocyte was changed by ultrasound application in the presence of microbubbles. (A) Bright field image before ultrasound of a group of cardiomyocytes clustered together attached on the upper inner membrane of Opticell. Some of the black circles were Definity® microbubbles, such as the ones pointed by arrows. The area within the frame was selected to monitor the contraction. The zoomed area is shown on the right side of the image. The black small area in the center of this frame was traced and analyzed using Matlab. Its displacement relative to its original position at time 0 as a function of time was plotted in (B). A single ultrasound pulse with 0.43MPa peak negative pressure and 8μs duration was applied at time 10s.

5.1.2 Study of gene internalization and expression pathways in sonoporation

The $6.6 \pm 2.2\%$ (N=9) transfection efficiency of RASMC is encouraging, and comparable with lipofection result, $7.5 \pm 0.8\%$ (N=9). However, the gene transfection efficiency is still considered low compared with the virus mediated transfection. Ultrasound application facilitates plasmid transporting across cell membrane. After entering cytoplasm, there were many intermediate steps before the protein, which the plasmid encodes, eventually expressed, such as the migration of plasmid from cytoplasm towards nucleus, transportation across nucleic envelope, and expression of plasmid, etc. Obstacles may exist in these pathways. Therefore, to further understand and improve gene transfection efficiency, it's of great importance to reveal the internalization and expression pathways of exogenous plasmid after sonoporation. Figure 5-2 shows the

preliminary work we have done, showing that gene uptake manner and fate of exogenous plasmid inside the cells are different in sonoporation and lipofection. It is well known that in lipofection endocytosis is the plasmid uptake mechanisms. In this preliminary study, we labeled the plasmid with BOBOTM-3 iodide as described in Chapter 4.

Although the BOBO-plasmid signal was strong and evenly distributed throughout the cell right after ultrasound (Fig.5-2 A) indicating a rapid and efficient physical route was created by ultrasound application to transport plasmid across cell membrane. However, 24 hours later, BOBO-plasmid fluorescent signal disappeared completely (Fig.5-2 B). In contrast, in lipofection BOBO-labeled plasmid still can be seen clearly 24 hours later (Fig.5-3 C). Moreover, in lipofection BOBO-labeled plasmid fluorescent signals were clustered in many small spots, which perfectly matched with vesicle structure shown in phase contrast bright field, suggesting that the plasmid was transferred via endocytosis and were still confined in endocytic vesicles 24 hours later. After sonoporation, however, vesicle structure was not observed at all in phase contrast bright field images, indicating endocytosis was not involved in sonoporation. This preliminary result is consistent with other studies visualizing plasmid kinetics in sonoporation [3, 40]. For the future work, live cell imaging can be applied to continuously monitor the plasmid change in cytoplasm as well as the GFP expression dynamics.

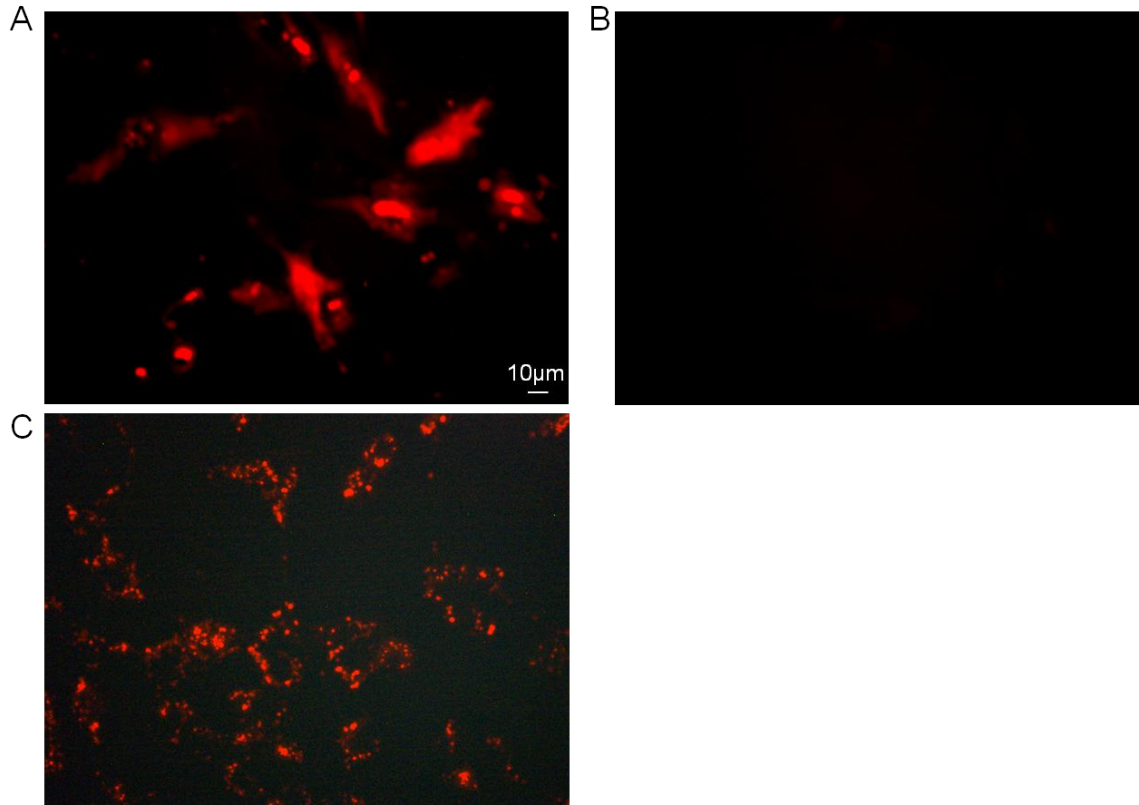


Figure 5-2 BOBO-labeled plasmid distribution 30minutes after sonoporation (A), and 24 hours after sonoporation (B) of the same area; and 24 hours after lipofection (C).

5.1.3 Microbubbles patterning and spatially defined delivery by incorporating aqueous two phase system (ATPS) with sonoporation

To precisely control microbubbles location in this thesis work, we took advantage of the ligand-receptor binding used in targeted microbubbles. However, to reach 10 µg/ml plasmid concentration, a large amount of plasmid was needed to dissolve in the extracellular medium, which is not a reagent efficient manner, wasting a lot of expensive material, such as plasmid; and to bind targeted microbubbles onto cell membrane, a protocol including flipping the dish was applied, which is inconvenient and could introduce uneven binding outcomes if the dish is slight tilt during facing down period. We can solve all these problems if we can confine the microbubbles as well as

plasmid in a small volume right on top of cell membrane. Aqueous two-phases systems (ATPS) have been demonstrated as a successful method to deliver genetic materials to mammalian cells using liquid patterning of droplets containing only hundreds of nanoliter liquid [207]. With modified formula, it's possible to generate picoliter droplet confining microbubbles covering a surface with attached cells. Because of the picoliter volume, the interface of two phases will be very close to cell surface, so that microbubbles can contact cell membrane without flipping over dishes. In the meantime, the reagents for delivery, such as plasmids, can be mixed and confined in the picoliter droplet as well, providing cell-reagent efficient condition and resulting 0.01 mm^2 level spatially defined delivery outcomes by sonoporation. The concept is illustrated as illustrated in Fig.5-3.

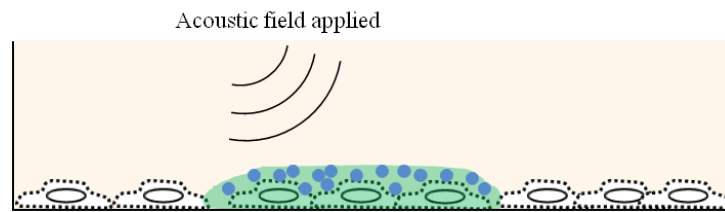


Figure 5-3 Illustration of picoliter microbubble patterning and spatially defined delivery

References

- [1] R. Langer, Drug delivery. *Drugs on target. Science* 293(5527) (2001) 58-59.
- [2] L. Rajendran, H.J. Knolker, K. Simons, Subcellular targeting strategies for drug design and delivery. *Nat Rev Drug Discov* 9(1) (2010) 29-42.
- [3] J.L. Tlaxca, C.R. Anderson, A.L. Klibanov, B. Lowrey, J.A. Hossack, J.S. Alexander, M.B. Lawrence, J.J. Rychak, Analysis of in vitro transfection by sonoporation using cationic and neutral microbubbles. *Ultrasound Med Biol* 36(11) (2010) 1907-1918.
- [4] C.M. Newman, T. Bettinger, Gene therapy progress and prospects: ultrasound for gene transfer. *Gene Ther* 14(6) (2007) 465-475.
- [5] H. Fujii, S.H. Li, J. Wu, Y. Miyagi, T.M. Yau, H. Rakowski, K. Egashira, J. Guo, R.D. Weisel, R.K. Li, Repeated and targeted transfer of angiogenic plasmids into the infarcted rat heart via ultrasound targeted microbubble destruction enhances cardiac repair. *Eur Heart J* 32(16) (2011) 2075-2084.
- [6] R. Suzuki, T. Takizawa, Y. Negishi, N. Utoguchi, K. Sawamura, K. Tanaka, E. Namai, Y. Oda, Y. Matsumura, K. Maruyama, Tumor specific ultrasound enhanced gene transfer in vivo with novel liposomal bubbles. *J Control Release* 125(2) (2008) 137-144.
- [7] C.X. Deng, Targeted drug delivery across the blood-brain barrier using ultrasound technique. *Ther Deliv* 1(6) (2010) 819-848.
- [8] M. Kinoshita, K. Hynynen, A novel method for the intracellular delivery of siRNA using microbubble-enhanced focused ultrasound. *Biochem Biophys Res Commun* 335(2) (2005) 393-399.
- [9] K. Otani, K. Yamahara, S. Ohnishi, H. Obata, S. Kitamura, N. Nagaya, Nonviral delivery of siRNA into mesenchymal stem cells by a combination of ultrasound and microbubbles. *J Control Release* 133(2) (2009) 146-153.
- [10] R.E. Vandenbroucke, I. Lentacker, J. Demeester, S.C. De Smedt, N.N. Sanders, Ultrasound assisted siRNA delivery using PEG-siPlex loaded microbubbles. *J Control Release* 126(3) (2008) 265-273.
- [11] C.R. Mayer, N.A. Geis, H.A. Katus, R. Bekeredjian, Ultrasound targeted microbubble destruction for drug and gene delivery. *Expert Opin Drug Deliv* 5(10) (2008) 1121-1138.
- [12] K. Ferrara, R. Pollard, M. Borden, Ultrasound microbubble contrast agents: fundamentals and application to gene and drug delivery. *Annu Rev Biomed Eng* 9 (2007) 415-447.
- [13] P. Prentice, A. Cuschieri, K. Dholakia, M. Prausnitz, P. Campbell, Membrane disruption by optically controlled microbubble cavitation. *Nature Physics* 1(2) (2005) 107.
- [14] N. Kudo, K. Okada, K. Yamamoto, Sonoporation by single-shot pulsed ultrasound with microbubbles adjacent to cells. *Biophys J* 96(12) (2009) 4866-4876.
- [15] R.K. Schlicher, H. Radhakrishna, T.P. Tolentino, R.P. Apkarian, V. Zarnitsyn, M.R. Prausnitz, Mechanism of intracellular delivery by acoustic cavitation. *Ultrasound Med Biol* 32(6) (2006) 915-924.
- [16] Z. Fan, R.E. Kumon, J. Park, C.X. Deng, Intracellular delivery and calcium transients generated in sonoporation facilitated by microbubbles. *J Control Release* 142(1) (2010) 31-39.

- [17] Y. Qiu, Y. Luo, Y. Zhang, W. Cui, D. Zhang, J. Wu, J. Zhang, J. Tu, The correlation between acoustic cavitation and sonoporation involved in ultrasound-mediated DNA transfection with polyethylenimine (PEI) in vitro. *J Control Release* 145(1) (2010) 40-48.
- [18] M.S. Al-Dosari, X. Gao, Nonviral gene delivery: principle, limitations, and recent progress. *AAPS J* 11(4) (2009) 671-681.
- [19] J.M. Escoffre, T. Portet, L. Wasungu, J. Teissie, D. Dean, M.P. Rols, What is (still not) known of the mechanism by which electroporation mediates gene transfer and expression in cells and tissues. *Mol Biotechnol* 41(3) (2009) 286-295.
- [20] S. Ganta, H. Devalapally, A. Shahiwala, M. Amiji, A review of stimuli-responsive nanocarriers for drug and gene delivery. *J Control Release* 126(3) (2008) 187-204.
- [21] R. Waehler, S.J. Russell, D.T. Curiel, Engineering targeted viral vectors for gene therapy. *Nat Rev Genet* 8(8) (2007) 573-587.
- [22] R. Suzuki, Y. Oda, N. Utoguchi, K. Maruyama, Progress in the development of ultrasound-mediated gene delivery systems utilizing nano- and microbubbles. *J Control Release* 149(1) (2011) 36-41.
- [23] C.X. Deng, F. Sieling, H. Pan, J. Cui, Ultrasound-induced cell membrane porosity. *Ultrasound Med Biol* 30(4) (2004) 519-526.
- [24] M.E. Davis, The first targeted delivery of siRNA in humans via a self-assembling, cyclodextrin polymer-based nanoparticle: from concept to clinic. *Mol Pharm* 6(3) (2009) 659-668.
- [25] J.M. Escoffre, J. Teissie, M.P. Rols, Gene transfer: how can the biological barriers be overcome? *J Membr Biol* 236(1) (2010) 61-74.
- [26] S. Hernot, A.L. Klibanov, Microbubbles in ultrasound-triggered drug and gene delivery. *Adv Drug Deliv Rev* 60(10) (2008) 1153-1166.
- [27] I.A. Khalil, K. Kogure, H. Akita, H. Harashima, Uptake pathways and subsequent intracellular trafficking in nonviral gene delivery. *Pharmacol Rev* 58(1) (2006) 32-45.
- [28] S.D. Li, L. Huang, Gene therapy progress and prospects: non-viral gene therapy by systemic delivery. *Gene Ther* 13(18) (2006) 1313-1319.
- [29] W. Walther, U. Stein, Viral vectors for gene transfer: a review of their use in the treatment of human diseases. *Drugs* 60(2) (2000) 249-271.
- [30] Z.C. Hartman, D.M. Appledorn, A. Amalfitano, Adenovirus vector induced innate immune responses: impact upon efficacy and toxicity in gene therapy and vaccine applications. *Virus Res* 132(1-2) (2008) 1-14.
- [31] S. Nayak, R.W. Herzog, Progress and prospects: immune responses to viral vectors. *Gene Ther* 17(3) (2010) 295-304.
- [32] D. Schaffert, E. Wagner, Gene therapy progress and prospects: synthetic polymer-based systems. *Gene Ther* 15(16) (2008) 1131-1138.
- [33] H.C. Birnboim, J. Doly, A rapid alkaline extraction procedure for screening recombinant plasmid DNA. *Nucleic Acids Res* 7(6) (1979) 1513-1523.
- [34] M.E. Davis, Non-viral gene delivery systems. *Curr Opin Biotechnol* 13(2) (2002) 128-131.
- [35] P.L. Felgner, T.R. Gadek, M. Holm, R. Roman, H.W. Chan, M. Wenz, J.P. Northrop, G.M. Ringold, M. Danielsen, Lipofection: a highly efficient, lipid-mediated DNA-transfection procedure. *Proc Natl Acad Sci U S A* 84(21) (1987) 7413-7417.

- [36] M.J. Hope, B. Mui, S. Ansell, Q.F. Ahkong, Cationic lipids, phosphatidylethanolamine and the intracellular delivery of polymeric, nucleic acid-based drugs (review). *Mol Membr Biol* 15(1) (1998) 1-14.
- [37] P.P. Karmali, A. Chaudhuri, Cationic liposomes as non-viral carriers of gene medicines: resolved issues, open questions, and future promises. *Med Res Rev* 27(5) (2007) 696-722.
- [38] D. Lechardeur, A.S. Verkman, G.L. Lukacs, Intracellular routing of plasmid DNA during non-viral gene transfer. *Adv Drug Deliv Rev* 57(5) (2005) 755-767.
- [39] A.P. Lam, D.A. Dean, Progress and prospects: nuclear import of nonviral vectors. *Gene Ther* 17(4) (2010) 439-447.
- [40] S. Mehier-Humbert, T. Bettinger, F. Yan, R.H. Guy, Ultrasound-mediated gene delivery: kinetics of plasmid internalization and gene expression. *J Control Release* 104(1) (2005) 203-211.
- [41] M. Nishikawa, L. Huang, Nonviral vectors in the new millennium: delivery barriers in gene transfer. *Hum Gene Ther* 12(8) (2001) 861-870.
- [42] D.J. Wells, Electroporation and ultrasound enhanced non-viral gene delivery in vitro and in vivo. *Cell Biol Toxicol* 26(1) (2010) 21-28.
- [43] S. Mehier-Humbert, R.H. Guy, Physical methods for gene transfer: improving the kinetics of gene delivery into cells. *Adv Drug Deliv Rev* 57(5) (2005) 733-753.
- [44] J. Villemejeane, L.M. Mir, Physical methods of nucleic acid transfer: general concepts and applications. *Br J Pharmacol* 157(2) (2009) 207-219.
- [45] C. Chen, S.W. Smye, M.P. Robinson, J.A. Evans, Membrane electroporation theories: a review. *Med Biol Eng Comput* 44(1-2) (2006) 5-14.
- [46] F. Andre, L.M. Mir, DNA electrotransfer: its principles and an updated review of its therapeutic applications. *Gene Ther* 11 Suppl 1 (2004) S33-42.
- [47] T. Muramatsu, A. Nakamura, H.M. Park, In vivo electroporation: a powerful and convenient means of nonviral gene transfer to tissues of living animals (Review). *Int J Mol Med* 1(1) (1998) 55-62.
- [48] J.C. Weaver, Electroporation theory. Concepts and mechanisms. *Methods Mol Biol* 47 (1995) 1-26.
- [49] D.C. Chang, T.S. Reese, Changes in membrane structure induced by electroporation as revealed by rapid-freezing electron microscopy. *Biophys J* 58(1) (1990) 1-12.
- [50] G.A. Hofmann, S.B. Dev, G.S. Nanda, D. Rabussay, Electroporation therapy of solid tumors. *Crit Rev Ther Drug Carrier Syst* 16(6) (1999) 523-569.
- [51] L.C. Smith, J.L. Nordstrom, Advances in plasmid gene delivery and expression in skeletal muscle. *Curr Opin Mol Ther* 2(2) (2000) 150-154.
- [52] K.W. Ferrara, M.A. Borden, H. Zhang, Lipid-shelled vehicles: engineering for ultrasound molecular imaging and drug delivery. *Acc Chem Res* 42(7) (2009) 881-892.
- [53] A.L. Klibanov, Microbubble contrast agents: targeted ultrasound imaging and ultrasound-assisted drug-delivery applications. *Invest Radiol* 41(3) (2006) 354-362.
- [54] S. Bao, B.D. Thrall, D.L. Miller, Transfection of a reporter plasmid into cultured cells by sonoporation in vitro. *Ultrasound Med Biol* 23(6) (1997) 953-959.
- [55] D.L. Miller, S.V. Pislaru, J.E. Greenleaf, Sonoporation: mechanical DNA delivery by ultrasonic cavitation. *Somat Cell Mol Genet* 27(1-6) (2002) 115-134.

- [56] C.D. Ohl, M. Arora, R. Ikink, N. de Jong, M. Versluis, M. Delius, D. Lohse, Sonoporation from jetting cavitation bubbles. *Biophys J* 91(11) (2006) 4285-4295.
- [57] S. Sonoda, K. Tachibana, E. Uchino, T. Yamashita, K. Sakoda, K.H. Sonoda, T. Hisatomi, Y. Izumi, T. Sakamoto, Inhibition of melanoma by ultrasound-microbubble-aided drug delivery suggests membrane permeabilization. *Cancer Biol Ther* 6(8) (2007) 1276-1283.
- [58] B.E. Polat, D. Hart, R. Langer, D. Blankschtein, Ultrasound-mediated transdermal drug delivery: mechanisms, scope, and emerging trends. *J Control Release* 152(3) (2011) 330-348.
- [59] P. Haag, F. Frauscher, J. Gradl, A. Seitz, G. Schafer, J.R. Lindner, A.L. Klibanov, G. Bartsch, H. Klocker, I.E. Eder, Microbubble-enhanced ultrasound to deliver an antisense oligodeoxynucleotide targeting the human androgen receptor into prostate tumours. *J Steroid Biochem Mol Biol* 102(1-5) (2006) 103-113.
- [60] L.H. Treat, N. McDannold, N. Vykhodtseva, Y. Zhang, K. Tam, K. Hynynen, Targeted delivery of doxorubicin to the rat brain at therapeutic levels using MRI-guided focused ultrasound. *Int J Cancer* 121(4) (2007) 901-907.
- [61] M. Kinoshita, N. McDannold, F.A. Jolesz, K. Hynynen, Targeted delivery of antibodies through the blood-brain barrier by MRI-guided focused ultrasound. *Biochem Biophys Res Commun* 340(4) (2006) 1085-1090.
- [62] M. Kinoshita, K. Hynynen, Intracellular delivery of Bak BH3 peptide by microbubble-enhanced ultrasound. *Pharm Res* 22(5) (2005) 716-720.
- [63] R. Suzuki, Y. Oda, N. Utoguchi, E. Namai, Y. Taira, N. Okada, N. Kadowaki, T. Kodama, K. Tachibana, K. Maruyama, A novel strategy utilizing ultrasound for antigen delivery in dendritic cell-based cancer immunotherapy. *J Control Release* 133(3) (2009) 198-205.
- [64] Y.S. Li, E. Davidson, C.N. Reid, A.P. McHale, Optimising ultrasound-mediated gene transfer (sonoporation) in vitro and prolonged expression of a transgene in vivo: potential applications for gene therapy of cancer. *Cancer Lett* 273(1) (2009) 62-69.
- [65] S. Tsunoda, O. Mazda, Y. Oda, Y. Iida, S. Akabame, T. Kishida, M. Shin-Ya, H. Asada, S. Gojo, J. Imanishi, H. Matsubara, T. Yoshikawa, Sonoporation using microbubble BR14 promotes pDNA/siRNA transduction to murine heart. *Biochem Biophys Res Commun* 336(1) (2005) 118-127.
- [66] S. Chen, J.H. Ding, R. Bekeredjian, B.Z. Yang, R.V. Shohet, S.A. Johnston, H.E. Hohmeier, C.B. Newgard, P.A. Grayburn, Efficient gene delivery to pancreatic islets with ultrasonic microbubble destruction technology. *Proc Natl Acad Sci U S A* 103(22) (2006) 8469-8474.
- [67] L.C. Phillips, A.L. Klibanov, B.R. Wamhoff, J.A. Hossack, Targeted gene transfection from microbubbles into vascular smooth muscle cells using focused, ultrasound-mediated delivery. *Ultrasound Med Biol* 36(9) (2010) 1470-1480.
- [68] A. Delalande, M.F. Bureau, P. Midoux, A. Bouakaz, C. Pichon, Ultrasound-assisted microbubbles gene transfer in tendons for gene therapy. *Ultrasonics* 50(2) (2010) 269-272.
- [69] R. Gramiak, P.M. Shah, D.H. Kramer, Ultrasound Cardiography: Contrast Studies in Anatomy and Function. *Radiology* 92(5) (1969) 939-948.

- [70] B.B. Goldberg, J.B. Liu, P.N. Burns, D.A. Merton, F. Forsberg, Galactose-based intravenous sonographic contrast agent: experimental studies. *Journal of Ultrasound in Medicine* 12(8) (1993) 463-470.
- [71] B.B. Goldberg, J.-B. Liu, F. Forsberg, Ultrasound contrast agents: A review. *Ultrasound in Medicine & Biology* 20(4) (1994) 319-333.
- [72] A.L. Klibanov, Preparation of targeted microbubbles: ultrasound contrast agents for molecular imaging. *Med Biol Eng Comput* 47(8) (2009) 875-882.
- [73] S. Qin, C.F. Caskey, K.W. Ferrara, Ultrasound contrast microbubbles in imaging and therapy: physical principles and engineering. *Phys Med Biol* 54(6) (2009) R27-57.
- [74] M.A. Borden, G.V. Martinez, J. Ricker, N. Tsvetkova, M. Longo, R.J. Gillies, P.A. Dayton, K.W. Ferrara, Lateral phase separation in lipid-coated microbubbles. *Langmuir* 22(9) (2006) 4291-4297.
- [75] G. Pu, M.A. Borden, M.L. Longo, Collapse and shedding transitions in binary lipid monolayers coating microbubbles. *Langmuir* 22(7) (2006) 2993-2999.
- [76] M.A. Borden, M. Longo, Dissolution Behavior of Lipid Monolayer-Coated, Air-Filled Microbubbles: Effect of Lipid Hydrophobic Chain Length. *Langmuir* 18 (2002) 9225-9233.
- [77] S.H. Bloch, R.E. Short, K.W. Ferrara, E.R. Wisner, The effect of size on the acoustic response of polymer-shelled contrast agents. *Ultrasound Med Biol* 31(3) (2005) 439-444.
- [78] D.N. Patel, S.H. Bloch, P.A. Dayton, K.W. Ferrara, Acoustic signatures of submicron contrast agents. *IEEE Trans Ultrason Ferroelectr Freq Control* 51(3) (2004) 293-301.
- [79] P. Marmottant, S. van der Meer, M. Emmer, M. Versluis, N. de Jong, S. Hilgenfeldt, D. Lohse, A model for large amplitude oscillations of coated bubbles accounting for buckling and rupture. *J Acoust Soc Am* 118(6) (2005) 3499-3505.
- [80] N. de Jong, M. Emmer, C.T. Chin, A. Bouakaz, F. Mastik, D. Lohse, M. Versluis, "Compression-only" behavior of phospholipid-coated contrast bubbles. *Ultrasound Med Biol* 33(4) (2007) 653-656.
- [81] M.A. Borden, D.E. Kruse, C.F. Caskey, S. Zhao, P.A. Dayton, K.W. Ferrara, Influence of lipid shell physicochemical properties on ultrasound-induced microbubble destruction. *IEEE Trans Ultrason Ferroelectr Freq Control* 52(11) (2005) 1992-2002.
- [82] S. Qin, K.W. Ferrara, A model for the dynamics of ultrasound contrast agents in vivo. *J Acoust Soc Am* 128(3) (2010) 1511-1521.
- [83] P.A. Dayton, K.E. Morgan, A.L. Klibanov, G.H. Brandenburger, K.W. Ferrara, Optical and acoustical observations of the effects of ultrasound on contrast agents. *IEEE Trans Ultrason Ferroelectr Freq Control* 46(1) (1999) 220-232.
- [84] K.E. Morgan, J.S. Allen, P.A. Dayton, J.E. Chomas, A.L. Klibanov, K.W. Ferrara, Experimental and theoretical evaluation of microbubble behavior: effect of transmitted phase and bubble size. *IEEE Trans Ultrason Ferroelectr Freq Control* 47(6) (2000) 1494-1509.
- [85] M. Overvelde, V. Garbin, J. Sijl, B. Dollet, N. de Jong, D. Lohse, M. Versluis, Nonlinear shell behavior of phospholipid-coated microbubbles. *Ultrasound Med Biol* 36(12) (2010) 2080-2092.

- [86] S.P. Wrenn, M. Mleczko, G. Schmitz, Phospholipid-stabilized microbubbles: Influence of shell chemistry on cavitation threshold and binding to giant uni-lamellar vesicles. *Applied Acoustics* 70(10) (2009) 1313-1322.
- [87] D.B. Ellegala, H. Leong-Poi, J.E. Carpenter, A.L. Klibanov, S. Kaul, M.E. Shaffrey, J. Sklenar, J.R. Lindner, Imaging tumor angiogenesis with contrast ultrasound and microbubbles targeted to alpha(v)beta3. *Circulation* 108(3) (2003) 336-341.
- [88] A.M. Takalkar, A.L. Klibanov, J.J. Rychak, J.R. Lindner, K. Ley, Binding and detachment dynamics of microbubbles targeted to P-selectin under controlled shear flow. *J Control Release* 96(3) (2004) 473-482.
- [89] H. Leong-Poi, J. Christiansen, A.L. Klibanov, S. Kaul, J.R. Lindner, Noninvasive assessment of angiogenesis by ultrasound and microbubbles targeted to alpha(v)-integrins. *Circulation* 107(3) (2003) 455-460.
- [90] I. Lentacker, S.C. De Smedt, J. Demeester, N.N. Sanders, Microbubbles which bind and protect DNA against nucleases. *J Control Release* 116(2) (2006) e73-75.
- [91] M.J. Shortencarier, P.A. Dayton, S.H. Bloch, P.A. Schumann, T.O. Matsunaga, K.W. Ferrara, A method for radiation-force localized drug delivery using gas-filled lipospheres. *IEEE Trans Ultrason Ferroelectr Freq Control* 51(7) (2004) 822-831.
- [92] A.F. Lum, M.A. Borden, P.A. Dayton, D.E. Kruse, S.I. Simon, K.W. Ferrara, Ultrasound radiation force enables targeted deposition of model drug carriers loaded on microbubbles. *J Control Release* 111(1-2) (2006) 128-134.
- [93] M. Postema, A. van Wamel, C.T. Lancee, N. de Jong, Ultrasound-induced encapsulated microbubble phenomena. *Ultrasound Med Biol* 30(6) (2004) 827-840.
- [94] W. Lauterborn, C.D. Ohl, Cavitation bubble dynamics. *Ultrason Sonochem* 4(2) (1997) 65-75.
- [95] J.E. Chomas, P. Dayton, D. May, K. Ferrara, Threshold of fragmentation for ultrasonic contrast agents. *J Biomed Opt* 6(2) (2001) 141-150.
- [96] N. de Jong, P.J. Frinking, A. Bouakaz, M. Goorden, T. Schourmans, X. Jingping, F. Mastik, Optical imaging of contrast agent microbubbles in an ultrasound field with a 100-MHz camera. *Ultrasound Med Biol* 26(3) (2000) 487-492.
- [97] A. van Wamel, K. Kooiman, M. Hartevelde, M. Emmer, F.J. ten Cate, M. Versluis, N. de Jong, Vibrating microbubbles poking individual cells: drug transfer into cells via sonoporation. *J Control Release* 112(2) (2006) 149-155.
- [98] A. van Wamel, A. Bouakaz, M. Versluis, N. de Jong, Micromanipulation of endothelial cells: Ultrasound-microbubble-cell interaction. *Ultrasound in Medicine & Biology* 30(9) (2004) 1255-1258.
- [99] T.G. Leighton, *The acoustic bubble*, Academic Press, London ; San Diego, Calif., 1994.
- [100] J. Wu, W.L. Nyborg, Ultrasound, cavitation bubbles and their interaction with cells. *Adv Drug Deliv Rev* 60(10) (2008) 1103-1116.
- [101] L.A. Crum, R.A. Roy, Sonoluminescence. *Science* 266(5183) (1994) 233-234.
- [102] D.L. Miller, R.M. Thomas, Ultrasound contrast agents nucleate inertial cavitation in vitro. *Ultrasound Med Biol* 21(8) (1995) 1059-1065.
- [103] T.J. Matula, R.A. Roy, Comparisons of sonoluminescence from single-bubbles and cavitation fields: bridging the gap. *Ultrason Sonochem* 4(2) (1997) 61-64.

- [104] J. Collis, R. Manasseh, P. Liovic, P. Tho, A. Ooi, K. Petkovic-Duran, Y. Zhu, Cavitation microstreaming and stress fields created by microbubbles. *Ultrasonics* 50(2) (2010) 273-279.
- [105] P. Tho, Cavitation microstreaming patterns in single and multiple bubble systems. *Journal of fluid mechanics* 576 (2007) 191.
- [106] S.A. Elder, Cavitation Microstreaming. *The Journal of the Acoustical Society of America* 31(1) (1959) 54.
- [107] I.C. Macedo, W.J. Yang, Acoustic effects on gas bubbles in the flows of viscous fluids and whole blood. *J Acoust Soc Am* 53(5) (1973) 1327-1335.
- [108] P.A. Dayton, J.S. Allen, K.W. Ferrara, The magnitude of radiation force on ultrasound contrast agents. *J Acoust Soc Am* 112(5 Pt 1) (2002) 2183-2192.
- [109] V. Bjerknes, Fields of force; supplementary lectures, applications to meteorology; a course of lectures in mathematical physics delivered December 1 to 23, 1905, The Columbia university press; [etc., New York, 1906.
- [110] C. Feuillade, Acoustically coupled gas bubbles in fluids: time-domain phenomena. *J Acoust Soc Am* 109(6) (2001) 2606-2615.
- [111] P. Dayton, A. Klibanov, G. Brandenburger, K. Ferrara, Acoustic radiation force in vivo: a mechanism to assist targeting of microbubbles. *Ultrasound Med Biol* 25(8) (1999) 1195-1201.
- [112] P.A. Dayton, K.E. Morgan, A.L. Klibanov, G. Brandenburger, K.R. Nightingale, K.W. Ferrara, A preliminary evaluation of the effects of primary and secondary radiation forces on acoustic contrast agents. *Ultrasonics, Ferroelectrics and Frequency Control, IEEE Transactions on* 44(6) (1997) 1264-1277.
- [113] M. Postema, P. Marmottant, C.T. Lancee, S. Hilgenfeldt, N. de Jong, Ultrasound-induced microbubble coalescence. *Ultrasound Med Biol* 30(10) (2004) 1337-1344.
- [114] P. Marmottant, S. Hilgenfeldt, Controlled vesicle deformation and lysis by single oscillating bubbles. *Nature* 423(6936) (2003) 153.
- [115] S. Mehier-Humbert, T. Bettinger, F. Yan, R.H. Guy, Plasma membrane poration induced by ultrasound exposure: implication for drug delivery. *J Control Release* 104(1) (2005) 213-222.
- [116] K. Tachibana, T. Uchida, K. Ogawa, N. Yamashita, K. Tamura, Induction of cell-membrane porosity by ultrasound. *Lancet* 353(9162) (1999) 1409.
- [117] Y. Liu, H. Yang, A. Sakanishi, Ultrasound: mechanical gene transfer into plant cells by sonoporation. *Biotechnol Adv* 24(1) (2006) 1-16.
- [118] K. Ogawa, K. Tachibana, T. Uchida, T. Tai, N. Yamashita, N. Tsujita, R. Miyauchi, High-resolution scanning electron microscopic evaluation of cell-membrane porosity by ultrasound. *Med Electron Microsc* 34(4) (2001) 249-253.
- [119] Y.Z. Zhao, Y.K. Luo, C.T. Lu, J.F. Xu, J. Tang, M. Zhang, Y. Zhang, H.D. Liang, Phospholipids-based microbubbles sonoporation pore size and reseal of cell membrane cultured in vitro. *J Drug Target* 16(1) (2008) 18-25.
- [120] Y. Zhou, R.E. Kumon, J. Cui, C.X. Deng, The size of sonoporation pores on the cell membrane. *Ultrasound Med Biol* 35(10) (2009) 1756-1760.
- [121] B.D. Meijering, L.J. Juffermans, A. van Wamel, R.H. Henning, I.S. Zuhorn, M. Emmer, A.M. Versteilen, W.J. Paulus, W.H. van Gilst, K. Kooiman, N. de Jong, R.J. Musters, L.E. Deelman, O. Kamp, Ultrasound and microbubble-targeted delivery of

- macromolecules is regulated by induction of endocytosis and pore formation. *Circ Res* 104(5) (2009) 679-687.
- [122] V. Zarnitsyn, C.A. Rostad, M.R. Prausnitz, Modeling Transmembrane Transport through Cell Membrane Wounds Created by Acoustic Cavitation. *Biophysical Journal* 95(9) (2008) 4124-4138.
- [123] V. Lionetti, A. Fittipaldi, S. Agostini, M. Giacca, F.A. Recchia, E. Picano, Enhanced caveolae-mediated endocytosis by diagnostic ultrasound in vitro. *Ultrasound Med Biol* 35(1) (2009) 136-143.
- [124] L.J. Juffermans, P.A. Dijkmans, R.J. Musters, C.A. Visser, O. Kamp, Transient permeabilization of cell membranes by ultrasound-exposed microbubbles is related to formation of hydrogen peroxide. *Am J Physiol Heart Circ Physiol* 291(4) (2006) H1595-1601.
- [125] L.J. Juffermans, D.B. Meijering, A. van Wamel, R.H. Henning, K. Kooiman, M. Emmer, N. de Jong, W.H. van Gilst, R. Musters, W.J. Paulus, A.C. van Rossum, L.E. Deelman, O. Kamp, Ultrasound and microbubble-targeted delivery of therapeutic compounds: ICIN Report Project 49: Drug and gene delivery through ultrasound and microbubbles. *Neth Heart J* 17(2) (2009) 82-86.
- [126] L.J. Juffermans, A. van Dijk, C.A. Jongenelen, B. Drukarch, A. Reijerkerk, H.E. de Vries, O. Kamp, R.J. Musters, Ultrasound and microbubble-induced intra- and intercellular bioeffects in primary endothelial cells. *Ultrasound Med Biol* 35(11) (2009) 1917-1927.
- [127] A. Tsukamoto, S. Higashiyama, K. Yoshida, Y. Watanabe, K.S. Furukawa, T. Ushida, Stable cavitation induces increased cytoplasmic calcium in L929 fibroblasts exposed to 1-MHz pulsed ultrasound. *Ultrasonics* 51(8) (2011) 982-990.
- [128] R.E. Kumon, M. Aehle, D. Sabens, P. Parikh, Y.W. Han, D. Kourennyi, C.X. Deng, Spatiotemporal effects of sonoporation measured by real-time calcium imaging. *Ultrasound Med Biol* 35(3) (2009) 494-506.
- [129] R.E. Kumon, M. Aehle, D. Sabens, P. Parikh, D. Kourennyi, C.X. Deng, Ultrasound-induced calcium oscillations and waves in Chinese hamster ovary cells in the presence of microbubbles. *Biophys J* 93(6) (2007) L29-31.
- [130] D.L. Miller, C. Dou, Induction of apoptosis in sonoporation and ultrasonic gene transfer. *Ultrasound Med Biol* 35(1) (2009) 144-154.
- [131] L.B. Feril, Jr., T. Kondo, Q.L. Zhao, R. Ogawa, K. Tachibana, N. Kudo, S. Fujimoto, S. Nakamura, Enhancement of ultrasound-induced apoptosis and cell lysis by echo-contrast agents. *Ultrasound Med Biol* 29(2) (2003) 331-337.
- [132] H. Honda, Q.L. Zhao, T. Kondo, Effects of dissolved gases and an echo contrast agent on apoptosis induced by ultrasound and its mechanism via the mitochondria-caspase pathway. *Ultrasound Med Biol* 28(5) (2002) 673-682.
- [133] H. Honda, T. Kondo, Q.L. Zhao, L.B. Feril, Jr., H. Kitagawa, Role of intracellular calcium ions and reactive oxygen species in apoptosis induced by ultrasound. *Ultrasound Med Biol* 30(5) (2004) 683-692.
- [134] L.B. Feril, Jr., T. Kondo, Z.G. Cui, Y. Tabuchi, Q.L. Zhao, H. Ando, T. Misaki, H. Yoshikawa, S. Umemura, Apoptosis induced by the sonomechanical effects of low intensity pulsed ultrasound in a human leukemia cell line. *Cancer Lett* 221(2) (2005) 145-152.

- [135] L.J. Juffermans, O. Kamp, P.A. Dijkmans, C.A. Visser, R.J. Musters, Low-intensity ultrasound-exposed microbubbles provoke local hyperpolarization of the cell membrane via activation of BK(Ca) channels. *Ultrasound Med Biol* 34(3) (2008) 502-508.
- [136] T.A. Tran, J.Y. Le Guennec, P. Bougnoux, F. Tranquart, A. Bouakaz, Characterization of cell membrane response to ultrasound activated microbubbles. *IEEE Trans Ultrason Ferroelectr Freq Control* 55(1) (2008) 43-49.
- [137] T.A. Tran, J.Y. Le Guennec, D. Babuty, P. Bougnoux, F. Tranquart, A. Bouakaz, On the mechanisms of ultrasound contrast agents-induced arrhythmias. *Ultrasound Med Biol* 35(6) (2009) 1050-1056.
- [138] T.A. Tran, S. Roger, J.Y. Le Guennec, F. Tranquart, A. Bouakaz, Effect of ultrasound-activated microbubbles on the cell electrophysiological properties. *Ultrasound Med Biol* 33(1) (2007) 158-163.
- [139] P.A. Frenkel, S. Chen, T. Thai, R.V. Shohet, P.A. Grayburn, DNA-loaded albumin microbubbles enhance ultrasound-mediated transfection in vitro. *Ultrasound Med Biol* 28(6) (2002) 817-822.
- [140] M. Kinoshita, K. Hynynen, Key factors that affect sonoporation efficiency in in vitro settings: the importance of standing wave in sonoporation. *Biochem Biophys Res Commun* 359(4) (2007) 860-865.
- [141] C.H. Su, C.Y. Chang, H.H. Wang, Y.J. Wu, T. Bettinger, C.H. Tsai, H.I. Yeh, Ultrasonic microbubble-mediated gene delivery causes phenotypic changes of human aortic endothelial cells. *Ultrasound Med Biol* 36(3) (2010) 449-458.
- [142] R. Karshafian, P.D. Bevan, R. Williams, S. Samac, P.N. Burns, Sonoporation by ultrasound-activated microbubble contrast agents: effect of acoustic exposure parameters on cell membrane permeability and cell viability. *Ultrasound Med Biol* 35(5) (2009) 847-860.
- [143] B.D. Meijering, R.H. Henning, W.H. Van Gilst, I. Gavrilovic, A. Van Wamel, L.E. Deelman, Optimization of ultrasound and microbubbles targeted gene delivery to cultured primary endothelial cells. *J Drug Target* 15(10) (2007) 664-671.
- [144] A. Rahim, S.L. Taylor, N.L. Bush, G.R. ter Haar, J.C. Bamber, C.D. Porter, Physical parameters affecting ultrasound/microbubble-mediated gene delivery efficiency in vitro. *Ultrasound Med Biol* 32(8) (2006) 1269-1279.
- [145] M. Ward, J. Wu, J.F. Chiu, Experimental study of the effects of Optison concentration on sonoporation in vitro. *Ultrasound Med Biol* 26(7) (2000) 1169-1175.
- [146] K.Y. Ng, Y. Liu, Therapeutic ultrasound: its application in drug delivery. *Med Res Rev* 22(2) (2002) 204-223.
- [147] S. Mitragotri, Healing sound: the use of ultrasound in drug delivery and other therapeutic applications. *Nat Rev Drug Discov* 4(3) (2005) 255-260.
- [148] J. Wu, W.L. Nyborg, Emerging therapeutic ultrasound, World Scientific, Hackensack, NJ, 2007.
- [149] V. Frenkel, Ultrasound mediated delivery of drugs and genes to solid tumors. *Adv Drug Deliv Rev* 60(10) (2008) 1193-1208.
- [150] K. Hynynen, Ultrasound for drug and gene delivery to the brain. *Adv Drug Deliv Rev* 60(10) (2008) 1209-1217.

- [151] C. Pichon, K. Kaddur, P. Midoux, F. Tranquart, A. Bouakaz, Recent advances in gene delivery with ultrasound and microbubbles. *Journal of Experimental Nanoscience* 3(1) (2008) 17-40.
- [152] C.X. Deng, in: V. Frenkel (Ed.), *Therapeutic Ultrasound: Mechanisms to Applications*, Nova Science Publishers, 2009 [in press].
- [153] P. Campbell, M.R. Prausnitz, Future directions for therapeutic ultrasound. *Ultrasound Med Biol* 33(4) (2007) 657.
- [154] R.E. Kumon, M. Aehle, D. Sabens, P. Parikh, D. Kourennyi, C.X. Deng, Ultrasound-induced calcium oscillations and waves in Chinese hamster ovary cells in the presence of microbubbles. *Biophys J* 93 (2007) L29-L31.
- [155] A. Tsukamoto, N. Yasui, Y. Watanabe, K. Furukawa, T. Ushida, in: A. Hierlemann (Ed.), *Sixth IASTED International Conference*, Vol. 601, Acta Press, Innsbruck, Austria, 2008, pp. 334-337.
- [156] R.E. Kumon, M. Aehle, D. Sabens, P. Parikh, Y.W. Han, D. Kourennyi, C.X. Deng, Spatiotemporal effects of sonoporation measured by real-time calcium imaging. *Ultrasound Med Biol* 35 (2009) 494-506.
- [157] G. Grynkiewicz, M. Poenie, R.Y. Tsien, A new generation of Ca^{2+} indicators with greatly improved fluorescence properties. *J Biol Chem* 260(6) (1985) 3440-3450.
- [158] S.J. Hong, Mechanism of endothelin-1-induced cytosolic Ca^{2+} mobility in cultured H9c2 myocardial ventricular cells. *Cell Signal* 14(10) (2002) 811-817.
- [159] R.Y. Tsien, A.T. Harootunian, Practical design criteria for a dynamic ratio imaging system. *Cell Calcium* 11(2-3) (1990) 93-109.
- [160] R.A. Steinhardt, G. Bi, J.M. Alderton, Cell membrane resealing by a vesicular mechanism similar to neurotransmitter release. *Science* 263(5145) (1994) 390-393.
- [161] T. Togo, J.M. Alderton, G.Q. Bi, R.A. Steinhardt, The mechanism of facilitated cell membrane resealing. *J Cell Sci* 112 (Pt 5) (1999) 719-731.
- [162] T. Togo, T.B. Krasieva, R.A. Steinhardt, A decrease in membrane tension precedes successful cell-membrane repair. *Mol Biol Cell* 11(12) (2000) 4339-4346.
- [163] V.L. Sukhorukov, C.S. Djuzenova, H. Frank, W.M. Arnold, U. Zimmermann, Electroporation and fluorescent tracer exchange: the role of whole-cell capacitance. *Cytometry* 21(3) (1995) 230-240.
- [164] C.S. Djuzenova, U. Zimmermann, H. Frank, V.L. Sukhorukov, E. Richter, G. Fuhr, Effect of medium conductivity and composition on the uptake of propidium iodide into electroporated myeloma cells. *Biochim Biophys Acta* 1284(2) (1996) 143-152.
- [165] M.J. Berridge, Elementary and global aspects of calcium signalling. *J Physiol* 499 (Pt 2) (1997) 291-306.
- [166] M.J. Berridge, P. Lipp, M.D. Bootman, The versatility and universality of calcium signalling. *Nat Rev Mol Cell Biol* 1(1) (2000) 11-21.
- [167] S. Boitano, E.R. Dirksen, M.J. Sanderson, Intercellular propagation of calcium waves mediated by inositol trisphosphate. *Science* 258(5080) (1992) 292-295.
- [168] H. Sauer, J. Hescheler, M. Wartenberg, Mechanical strain-induced Ca^{2+} waves are propagated via ATP release and purinergic receptor activation. *Am J Physiol Cell Physiol* 279(2) (2000) C295-307.
- [169] J.P. Ross, X. Cai, J.F. Chiu, J. Yang, J. Wu, Optical and atomic force microscopic studies on sonoporation. *J Acoust Soc Am* 111(3) (2002) 1161-1164.

- [170] M. Duvshani-Eshet, L. Baruch, E. Kesselman, E. Shimoni, M. Machluf, Therapeutic ultrasound-mediated DNA to cell and nucleus: bioeffects revealed by confocal and atomic force microscopy. *Gene Ther* 13(2) (2006) 163-172.
- [171] M. Duvshani-Eshet, D. Adam, M. Machluf, The effects of albumin-coated microbubbles in DNA delivery mediated by therapeutic ultrasound. *J Control Release* 112(2) (2006) 156-166.
- [172] F. Yang, N. Gu, D. Chen, X. Xi, D. Zhang, Y. Li, J. Wu, Experimental study on cell self-sealing during sonoporation. *J Control Release* 131(3) (2008) 205-210.
- [173] T.A. Tran, J.Y. Le Guennec, D. Babuty, P. Bougnoux, F. Tranquart, A. Bouakaz, On the Mechanisms of Ultrasound Contrast Agents-Induced Arrhythmias. *Ultrasound Med Biol* (2009) (in press).
- [174] S. Chapman, J. Windle, F. Xie, A. McGrain, T.R. Porter, Incidence of cardiac arrhythmias with therapeutic versus diagnostic ultrasound and intravenous microbubbles. *J Ultrasound Med* 24(8) (2005) 1099-1107.
- [175] P.A. van Der Wouw, A.C. Brauns, S.E. Bailey, J.E. Powers, A.A. Wilde, Premature ventricular contractions during triggered imaging with ultrasound contrast. *J Am Soc Echocardiogr* 13(4) (2000) 288-294.
- [176] P.S. Chen, A.Y. Tan, Autonomic nerve activity and atrial fibrillation. *Heart Rhythm* 4(3 Suppl) (2007) S61-64.
- [177] K.M. Dibb, H.K. Graham, L.A. Venetucci, D.A. Eisner, A.W. Trafford, Analysis of cellular calcium fluxes in cardiac muscle to understand calcium homeostasis in the heart. *Cell Calcium* 42(4-5) (2007) 503-512.
- [178] H.E. ter Keurs, Y. Wakayama, Y. Sugai, G. Price, Y. Kagaya, P.A. Boyden, M. Miura, B.D. Stuyvers, Role of sarcomere mechanics and Ca²⁺ overload in Ca²⁺ waves and arrhythmias in rat cardiac muscle. *Ann N Y Acad Sci* 1080 (2006) 248-267.
- [179] C.C. Chou, M. Nihei, S. Zhou, A. Tan, A. Kawase, E.S. Macias, M.C. Fishbein, S.F. Lin, P.S. Chen, Intracellular calcium dynamics and anisotropic reentry in isolated canine pulmonary veins and left atrium. *Circulation* 111(22) (2005) 2889-2897.
- [180] H. Honjo, M.R. Boyett, R. Niwa, S. Inada, M. Yamamoto, K. Mitsui, T. Horiuchi, N. Shibata, K. Kamiya, I. Kodama, Pacing-induced spontaneous activity in myocardial sleeves of pulmonary veins after treatment with ryanodine. *Circulation* 107(14) (2003) 1937-1943.
- [181] B.D. Stuyvers, P.A. Boyden, H.E. ter Keurs, Calcium waves: physiological relevance in cardiac function. *Circ Res* 86(10) (2000) 1016-1018.
- [182] V. Garbin, M. Overvelde, B. Dollet, N. de Jong, D. Lohse, M. Versluis, Unbinding of targeted ultrasound contrast agent microbubbles by secondary acoustic forces. *Phys Med Biol* 56(19) (2011) 6161-6177.
- [183] P. Marmottant, A. Bouakaz, N. de Jong, C. Quilliet, Buckling resistance of solid shell bubbles under ultrasound. *J Acoust Soc Am* 129(3) (2011) 1231-1239.
- [184] B.D.M. Meijering, R.H. Henning, W.H. Van Gilst, I. Gavrilovi, A. Van Wamel, L.E. Deelman, Optimization of ultrasound and microbubbles targeted gene delivery to cultured primary endothelial cells. *Journal of drug targeting* 15(10) (2007) 664.
- [185] P.A. Dayton, J.E. Chomas, A.F. Lum, J.S. Allen, J.R. Lindner, S.I. Simon, K.W. Ferrara, Optical and acoustical dynamics of microbubble contrast agents inside neutrophils. *Biophys J* 80(3) (2001) 1547-1556.

- [186] P.A. Dayton, K.E. Morgan, A.L. Klibanov, G. Brandenburger, K.R. Nightingale, K.W. Ferrara, A preliminary evaluation of the effects of primary and secondary radiation forces on acoustic contrast agents. *IEEE transactions on ultrasonics, ferroelectrics, and frequency control* 44(6) (1997) 1264.
- [187] S. Kotopoulos, M. Postema, Microfoam formation in a capillary. *Ultrasonics* 50(2) (2010) 260-268.
- [188] S. Zhao, M. Borden, S.H. Bloch, D. Kruse, K.W. Ferrara, P.A. Dayton, Radiation-force assisted targeting facilitates ultrasonic molecular imaging. *Mol Imaging* 3(3) (2004) 135-148.
- [189] R. Karshafian, S. Samac, P.D. Bevan, P.N. Burns, Microbubble mediated sonoporation of cells in suspension: Clonogenic viability and influence of molecular size on uptake. *Ultrasonics* (2010).
- [190] A.L. Klibanov, Ultrasound molecular imaging with targeted microbubble contrast agents. *J Nucl Cardiol* 14(6) (2007) 876-884.
- [191] R. Bekeredjian, S. Chen, P.A. Frenkel, P.A. Grayburn, R.V. Shohet, Ultrasound-targeted microbubble destruction can repeatedly direct highly specific plasmid expression to the heart. *Circulation* 108(8) (2003) 1022-1026.
- [192] G. Korpany, S. Chen, R.V. Shohet, J. Ding, B. Yang, P.A. Frenkel, P.A. Grayburn, Targeting of VEGF-mediated angiogenesis to rat myocardium using ultrasonic destruction of microbubbles. *Gene Ther* 12(17) (2005) 1305-1312.
- [193] J.E. Chomas, P. Dayton, J. Allen, K. Morgan, K.W. Ferrara, Mechanisms of contrast agent destruction. *IEEE Trans Ultrason Ferroelectr Freq Control* 48(1) (2001) 232-248.
- [194] V. Sboros, E. Glynos, J.A. Ross, C.M. Moran, S.D. Pye, M. Butler, W.N. McDicken, S.B. Brown, V. Koutsos, Probing microbubble targeting with atomic force microscopy. *Colloids Surf B Biointerfaces* 80(1) (2010) 12-17.
- [195] J.J. Rychak, A.L. Klibanov, K.F. Ley, J.A. Hossack, Enhanced targeting of ultrasound contrast agents using acoustic radiation force. *Ultrasound Med Biol* 33(7) (2007) 1132-1139.
- [196] M. Dembo, D.C. Torney, K. Saxman, D. Hammer, The reaction-limited kinetics of membrane-to-surface adhesion and detachment. *Proc R Soc Lond B Biol Sci* 234(1274) (1988) 55-83.
- [197] E.L. Florin, V.T. Moy, H.E. Gaub, Adhesion forces between individual ligand-receptor pairs. *Science* 264(5157) (1994) 415-417.
- [198] S.M. Watt, S.E. Gschmeissner, P.A. Bates, PECAM-1: its expression and function as a cell adhesion molecule on hemopoietic and endothelial cells. *Leuk Lymphoma* 17(3-4) (1995) 229-244.
- [199] J.M. Warram, A.G. Sorace, R. Saini, H.R. Umphrey, K.R. Zinn, K. Hoyt, A triple-targeted ultrasound contrast agent provides improved localization to tumor vasculature. *J Ultrasound Med* 30(7) (2011) 921-931.
- [200] D.E. Goertz, N. de Jong, A.F. van der Steen, Attenuation and size distribution measurements of Definity and manipulated Definity populations. *Ultrasound Med Biol* 33(9) (2007) 1376-1388.
- [201] M.B. Cannell, J.R. Berlin, W.J. Lederer, Effect of membrane potential changes on the calcium transient in single rat cardiac muscle cells. *Science* 238(4832) (1987) 1419-1423.

- [202] M.T. Nelson, J.B. Patlak, J.F. Worley, N.B. Standen, Calcium channels, potassium channels, and voltage dependence of arterial smooth muscle tone. *Am J Physiol* 259(1 Pt 1) (1990) C3-18.
- [203] K.S. Lee, E. Marban, R.W. Tsien, Inactivation of calcium channels in mammalian heart cells: joint dependence on membrane potential and intracellular calcium. *J Physiol* 364 (1985) 395-411.
- [204] D.M. Bers, Calcium fluxes involved in control of cardiac myocyte contraction. *Circ Res* 87(4) (2000) 275-281.
- [205] A. Fabiato, F. Fabiato, Contractions induced by a calcium-triggered release of calcium from the sarcoplasmic reticulum of single skinned cardiac cells. *J Physiol* 249(3) (1975) 469-495.
- [206] D.M. Bers, Cardiac excitation-contraction coupling. *Nature* 415(6868) (2002) 198-205.
- [207] H. Tavana, A. Jovic, B. Mosadegh, Q.Y. Lee, X. Liu, K.E. Luker, G.D. Luker, S.J. Weiss, S. Takayama, Nanolitre liquid patterning in aqueous environments for spatially defined reagent delivery to mammalian cells. *Nat Mater* 8(9) (2009) 736-741.